Universidad de Concepción
Dirección de postgrado
Facultad de Ingeniería
Programa de Doctorado en Ciencia e Ingeniería de Materiales

Development of ZnO-CeO_2/CeO_2-ZnO core-shell nanostructures by solvothermal and hydrothermal methods and their UV characteristics

Tesis para optar al grado de

Doctor en Ciencia e Ingeniería de Materiales

Saeed Farhang Sahlevani
Concepción-Chile
2019

Profesor Guía: Dr. Mangalaraja Ramalinga Viswanathan
Departamento de Ingeniería de Materiales
Facultad de Ingeniería
Universidad de Concepción

Acknowledgments

At the moment when I just finished typing the last words in this thesis, a kind of release suddenly came out from the bottom of my heart and ran through my entire body. All the scenes happened within last few years in University of Concepcion were suddenly flashing back. Many people who ever contributed to the work and helped me in life were slowly came into mind one by one. I truly appreciate and cherish what all of you have done for me, even though my gratitude is beyond words.

First of all, I would like to express my sincere gratitude to my supervisor Professor R.V. Mangalaraja who provided this huge opportunity for me and bring me into this warm relation. Therefore, I have a chance to have a brilliant new life in Chile which I will never forget for my entire life.

I express my gratitude to The Director of the Department Professor Camurri and all the Faculty members**,** of Department of the Materials Engineering, UdeC for their support during my research tenure. I am also grateful to all the doctorate committee members who gave this opportunely to achieve my gold.

This thesis would not be possible without the help of some individuals. I couldn't pass without acknowledging Dr. T. Pandiyarajan, Dr. R. Udayabhaskar, Mr. Felipe and my friends who has contributed a lot to my success.

I greatly acknowledge CONICYT and DIMAT for providing me with scholarship to carry out my doctorate program at University of Concepcion.

I thank all the **Non-teaching staff** for their kind support throughout my research period.

Last but not least, to my dear Maryam, I deeply thanks for the love, support and everything you have done for me. Thanks to you so much my first and last love.

To my family and teachers, who helped me to become what I am today.

Abstract

The nanomaterials have already taken a remarkable part in our everyday life due to their unique properties not seen in the respective bulk materials. The developments and innovation in nanomaterials have been considered as the new emerging nanotechnology of this century which has opened numerous opportunities in various fields, such as catalysis, optics, medicine, energy, information, etc. Today the ongoing quest of nanotechnology is to improve existing products by creating better performance at lower cost.

Among all multicomponent nanomaterials, core shell nanostructures are an important class of nanostructures which are attractive for their application in catalysis, drug delivery and bio-applications [1] due to their outstanding properties. The core shell nanostructures consist of an inner core and outer shell made of different material; therefore, the combination of different properties of different materials leads to novel properties. On the other hand, the core shell nanoparticles can be easily tuned by changing the size, shape, and components of core as well as thickness and components of shell materials. From the view of bio-applications, the bio-compatibility is the most important perspective of these materials. In other words, the biocompatibility of core shell structures can be improved by coating with biomaterials like silica, zinc oxide, polymer, and etc. The toxicity can be decreased, and shell layer can modified with biomolecules [1,2]. With these unique properties, the core shell nanostructures have attracted researchers for large variety of applications in chemistry, biotechnology, material science, energy, such as photocatalysis and optical spectroscopy, sensor, drug delivery, cancer treatment and bio-imaging.

This dissertation was structured as follows: The chapter 1 compromises the introduction. In the chapter 2 literature review of ZnO, CeO_2 and their core shell nanostructures were addressed.

The chapter 3 presents the experimental and characterization methods of ZnO, CeO_2 and their core shell nanostructures. The chapter 4 discusses about the results of ZnO and CeO_2 nanoparticles and ZnO@CeO_2/ CeO_2@ZnO core shell nanostructures obtained *via* hydrothermal and coprecipitation (solvothermal) methods. Also, the chapter 4 is provided with the details of the usage of the prepared nanostructures in the photocatalysis and UV screening applications. The dissertation concludes with summary and suggestion for future work as presented in the chapter 5.

Table of contents

List of tables

Table 4-17 The lattice parameters, crystallite size of ZnO, CeO_2 and their spherical core shell.

List of figures

Chapter 1

INTRODUCTION

1.1 Introduction

One of the most intense application of ZnO@CeO_2 core shell nanostructures is their usage in sunscreens due to their ability for strong absorption in UV region. Sunscreens are used to protect the skin against the harmful effect of ultraviolet (UV) and visible radiation. The UV region consists of three parts: (i) UVC (100-290 *nm*) with short wavelength and high energy (ii) UVB (290-320 *nm*) and (iii) UVA (320-400 *nm*. All of UVC and part of UVB were filtered off by atmosphere mainly because of smaller wavelengths. Remaining UVB along with UVA rays reaches our skin which effects our biological and metabolic reactions [3]. Sunscreens should provide protection against the adverse effects of both UVB and UVA as well visible radiation. Inorganic particulate ingredient particles, like zinc oxide(ZnO), cerium oxide [4] (CeO_2 also known as ceria) and titanium dioxide (TiO_2) which efficiently reflect or scatter UV radiation depending on the particles size or shape of structures. According to previous reports nanoparticles of TiO_2 has been reported to induce cytotoxicity and the formation of reactive oxygen species (ROS) in animal and human cell lines [5]. Also they kill the microorganisms related to photoactivation and led to free radical activity [6,7]. Furthermore coupled with its multiple potential exposure routes, indicated that nano TiO_2 could pose a risk to biological targets that are sensitive to oxidative stress damage, and which in turn can cause DNA damage [7], therefore mediates toxic effects on cells. There has been a growing public hysteria about the possible risks nano TiO_2 particles in sunscreen lotions. Among the various inorganic materials, ZnO and CeO_2 are the promising materials with multifunctional properties for addressing technological applications ranging from optoelectronics to environmental [8] and cosmetic applications [5].

ZnO is a representative II-VI compound semiconductor with direct band gap (3.37eV) and possess high exciton binding energy [9] (60meV) at room temperature. On the other hand, CeO_2 has diverse band gap from 2.7 to 3.4eV, depending on the size [10] with a cubic fluorite type crystal structure, can absorb a large fraction of the solar spectrum [11]. Both materials are most important n-type semiconductors, which have received much attention by scientists because of their wide band gap, chemical inertness and non-toxicity. ZnO with its good chemical stability proven as a suitable active material for ultraviolet light emitters, sensors (chemical and gas), solar cells and catalysis [12] applications. Among the rare earth oxides, CeO_2 is the most abundant in crust of earth [13] and considered as active material for various applications such as catalysis [14], fuel cells [15], ultraviolet absorbent [16] [17] applications. The previous reports noted that the protective effect of CeO_2 nanoparticles on UV-irradiated epithelial cell lines, showing that a pre-treatment with CeO_2 nanoparticles significantly increased viability in UV-ray-irradiated cells. In addition to their shielding properties, CeO_2 nanoparticles act as strong antioxidant due to the redox switch of Ce^{3+} and Ce^{4+} valence states in the oxide. In other words, CeO_2 nanoparticles abate the most noxious ROS in a catalytic, energy-free and auto-regenerative fashion [18].

Accordingly, CeO_2 nanoparticles protect cells and animals from many different harsh encounters, exert strong anti-apoptotic effects and ameliorating many serious oxidant-related pathologies promoting wound healing. Moreover [18,19], CeO_2 nanoparticles have exerted effective and intriguing anticancer effects [20]. Above all these properties, CeO_2 used as shell material due to its stability against photoirradiation and ability to respond for large fraction of absorption of the solar spectrum. In order to achieve novel applications, thin surface layer on particles were found to substantially change origin particles functionalities and properties, such as chemical reactivity [21], thermal stability [22,23], magnetic, optical and electronic properties [9],

makes it way as an active material for several disciplines including drug delivery, catalysis, cosmetics, optics and electrical industries [24–26].

The concept of core shell structure has received enormous attention of the researchers from different fields in order to define variety of solutions with advanced properties. Naturally, the core shell structures are constructed with core as inner material, and covered with one or more outer layer materials as a shell. According to the previous evidences, the core shell structures were classified based on material [27], arrangement of components, specific form and geometry [24]. Thus, aforementioned parameters would combine two properties of core and shell within one structure or offer a new property. However, advanced core shell structures possess unique and applicable properties and emerging as novel materials for wide range of applications. Generally, different thickness of shell has used to tune the property of particles, e.g. tuning shell thickness of gold on silica particles, moved the absorption band to infrared region [28], besides similar idea was utilized for the preparation of core shell which exhibited the quantum confinement, magnetic and optical properties. Among various inorganic core shell structures, ZnO and CeO_2 are the promising materials with cosmetic application [5].

Interestingly, ZnO@CeO_2 core shell structure has emerged as an ideal host material for UV applications. In order to allow better refractory properties, for increasing the sun protection factor (SPF) in most of the commercial lotions adopted the ZnO nanoparticles formulations. Coating with CeO_2 has expected to improve the properties of core (ZnO) material. The aim of present research was to fabricate the core shell ZnO@CeO_2 microstructures as well as to control the shell thickness and to investigate their structural and optical properties.

The main safety concern over the use of nanoparticles in cosmetics is their potential for penetration through the skin and subsequent entry into the body's systems. As per 'food and drug

administration (FDA)' and 'scientific committee on consumer safety (SCCS)' reports, it has been indicated that various attributes of a particular nanoscale material, including increased surface-area-to-volume ratio, morphology, surface features, and charge, can affect the distribution of that material in the body and that material's interaction with biological systems. Therefore, the characterization of nanomaterials can form an integral part of the safety assessment. This would include proper identification of the chemical composition as well as impurities, structure and configuration of the nanomaterial used in the cosmetic product. In addition, the characterization of the nanomaterials as present in the raw material, formulation and in the relevant biological environment for toxicological testing should be considered to determine potential biological interactions and effects [29]. Finally, the improvement of cosmetic sunscreen technology is of strong priority.

1.2 Nanomaterials

Nano is a prefix used to describe one billionth of somethings. A nanometer (*nm*) is an international system (system international, SI) of unit [30]. Here nano applied for the length. In principle, nanomaterials (NMs) are described as materials with length of 1–1000 *nm* in at least one dimension [31]; however, they are commonly defined to be of 1 to 100 *nm*. Nanotechnology has received considerable attention due to their potential applications to bring benefited in diverse areas such as drug delivery, water decontamination, information and communication technologies, energy, and realization of stronger and lighter materials. While the development of nanotechnologies is, a modern multidisciplinary science involving the field of chemistry, physic, materials engineering, and biotechnology. Ordinary materials, when reduced to the nanoscales, exhibit novel and unpredictable properties like chemical reactivity, electrical conductivity, optical properties, superparamagnetic behavior and some other characteristic, that the same materials

doesn't possess at the micro or bulk scale. Roughly, the synthesis of nanoparticles can be divided into solution based [32,33] (chemical) and gas or vapor based [34,35]. Generally, nanoparticles are prepared by different methods such as precipitation, hydrothermal, microwave combustion, ultrasonic cavitation, mechanical milling, thermal composition and etc. among them, hydrothermal and coprecipitation synthesis are attracted, because of their simplicity and easy way to prepare nanoparticles.

1.3 Semiconductors

Semiconductor materials as the name suggest are neither fully conductor nor they are insulator. The bandgap of such materials is more than that of conducting materials and less than that of insulator materials. Semiconductor materials generally have band gap less than the 4eV. Previously group IVA elements like Si and Ge were used as semiconductor but the advancement in materials physics led to the development of new semiconducting materials with the combination of various group like IB-VIIA, IIB-VIA, and IIIA-VA. The band gap of some semiconductors is quite high and that is why they called semi-insulators. GaAs is the most common example of the semi-insulator. Whereas, TiO_2 and ZnO are other examples of semi-insulator.

Since the semiconducting nanostructures represent one of the most important frontiers in advanced material research due to their peculiar optical, electrical, thermoelectric properties and potential applications in nanodevices. Semiconducting oxides are the fundamentals of smart devices as both the structure and morphology of these materials can be controlled precisely and accordingly, are referred as functional oxides. They have two structural characteristics: cations with mixed valence states, and anions with deficiencies. By varying either one or both of these characteristics, the electrical, optical, magnetic, and chemical properties can be tuned, giving the possibility of fabricating smart devices. The structures of functional oxides are very diverse and varied, and there

are endless new phenomena and applications. However, prior to looking for various applications it is worthwhile to consider the general features exhibited by some of these novel functional oxides. II-VI undoped and doped semiconductors have been focused of intense research due to their use in optoelectronic and semiconducting applications. These semiconductors demonstrated some unique properties, making them useful for unique applications [36–38].

In semiconductor core shell nanostructures core shell, either core, shell or both are made of semiconductor materials. Core shell nanostructures find application in many areas such as medical, optics and photovoltaics.

1.4 Hybrid nanomaterial

The surface chemistry and reactivity of materials at the nanoscale becomes important and can govern their optical and electronic properties. It is therefore very critical to develop new techniques to control the surface chemistry of the resulting nanomaterials. The study of the reaction of these nanoparticles with a variety of functionalized alkanes including alcohols, thiols, and silanes along with other metals and metal oxides to produce particles with core/shell structures has been an important area of research. The several studies in the last decade have reported on the synthesis of SiO_2-ZnO, SiO_2-TiO_2, Zn-ZnO core shell nanoparticles [9,39–41].

Core shell nanostructures are composed of two or more materials out of which at least one materials acting as a shell which cover the other core material. The core nanoparticles are encapsulated by the shell particles (Fig. 1-1), the most common shape is spherical core. The core shell nanostructure attracted the researchers with potential to address many problems related to energy, health care, environment and etc.

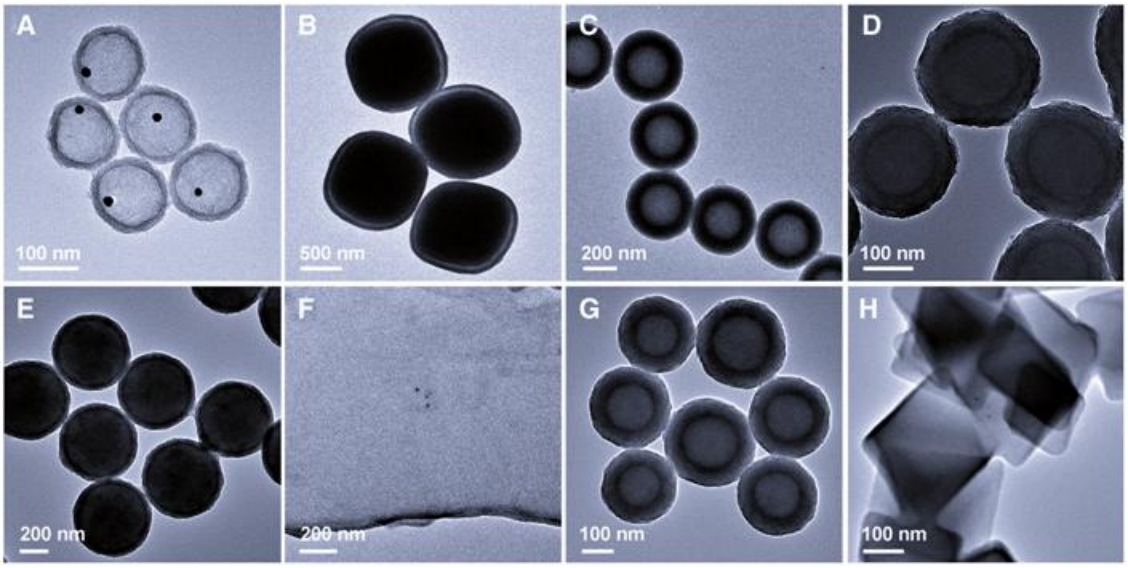

Fig. 1-1 TEM characterizations of (A)Au@TiO_2 core shell nanospheres. (B)Fe_2O_3@TiO_2 core shell. (C)TiO_2-polymer double-shell nanospheres. (D)MSN@TiO_2 core shell nanospheres. (E)PN@TiO_2 core shell nanospheres. (F)GO@TiO_2 composite nanosheets. (G)CN@TiO_2 core shell nanospheres. (H)MOF@TiO_2 core shell particles [42].

Numerous studies were carried out and reported on the synthesis, characterization, and application of core shell nanostructures. Although it's a challenging task to categories the core shell nanostructures as they can be differentiated in terms of synthesis route, edibility, targeted application, and so on. In a broad sense, we can categorize core shell into four types on the basis of core and shell materials. Inorganic or organic materials can be utilized for the synthesis of core shell nanomaterials. The broad classification of the core shell nanostructures can be understood from Fig. 1-2. This classification either base on type of core and shell materials like organic core organic shell, inorganic core-inorganic shell, organic core-inorganic shell and inorganic core organic shell, or based on properties of core and shell, such as core multishell and a movable core hollow shell. Out of all these categories, most important class of core shell nanostructures are inorganic core and inorganic shell. The core and shell are composed of silica, metal, metal oxide, semiconductors or other inorganic compounds. The inorganic core shell materials further were

divided into two parts, that is, silica containing and non-silica containing inorganic compounds. The subclass of inorganic core and inorganic shell materials are semiconducting core shell materials and lanthanides. Among this classification, the semiconductors inorganic core shell nanostructures have been studied and reported to have many applications in field of photocatalysis, energy and cosmetics.

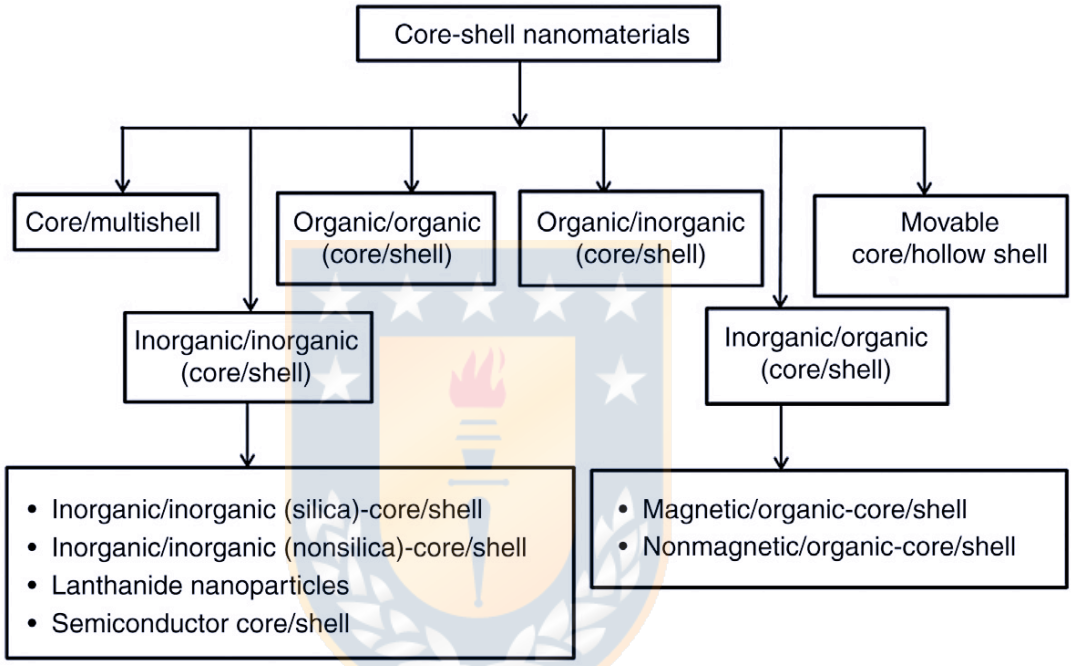

Fig. 1-2 Classification of core shell nanostructures [25].

Chapter 2

LITERATURE REVIEW

2.1. Zinc oxide

Over the decades, the control of optical and electronic properties of II-VI semiconductor nanostructured materials with morphologies (such as sphere, rods, tubes etc.) has been received a great attention due to their promising application in wide range of industrial applications like opto-electronics, sensors, solar cells and transistors [43]. Among the various II-VI semiconductors, Zinc Oxide (ZnO) nanostructures with its wide band gap (3.37 eV) and very high exciton binding energy (60 meV) at room temperature has been emerged as promising candidate for various opto-electronic applications [44]. The physical and chemical properties of ZnO nanostructures could be tuned through selective doping and by controlling their morphologies [45]. In the material science research community hexamethylenetetramine (HMTA), which is a heterocyclic organic compound received a great importance as an additive building block for self-assembled structures with tunability in size and shape by varying the reaction conditions [46]. Nanostructures with rod like shape are one class of nanomaterials which exhibit exceptional optical and electronic properties [47] and proved to be used as an active component material in technological applications such as optical switching [48], gas sensors [49], waveguides [50], solar cells [51], and lithium-ion batteries [52]. Over the years, for the fabrication of 1-D nanostructured materials several methods like wet chemical, chemical bath deposition [53], hydrothermal [54], microwave [55] and sonochemical [56] routes has been adopted by various research groups. Among these methods, wet chemical synthesis is one of the facile and cost effective synthesis technique to tune the aspect ratio the ZnO nanostructures. Recently, Feng et al. [57] reported about the role of hexamethylenetetramine (HMTA) on the formation of ZnO crystals which were prepared by wet chemical method.

Sornalatha et al. [58] reported about the band gap enhancement due to size effect in ZnO nanostructures which were synthesized by wet chemical method using HMTA as capping agent. Similarly, Musa et al. [59] reported the growth of ZnO nanorods from the colloidal nanoparticles and studied their length dependent photoluminescence properties of ZnO nanorods. Avireddy et al. reported that HMTA played a dual role, as a capping agent as well as a pH regulator in the preparation of the ZnO nanostructures for gas sensing application [60]. Likewise, Strano et al. [61] reported the dual role of HMTA on the growth of ZnO nanorods which were prepared by using chemical bath deposition. To the best of our knowledge, mechanism of formation of rod like ZnO nanostructures was reported by Vergas et al. [62] as follows: initial seeds achieve a critical size, then pair of seeds grownup to embryonic prism/needles which later converted into rods with an increase in length but not in width.

2.2. Cerium oxide

Nanostructured materials offered a great opportunity for the global research community to explore these advanced materials for promising energy and environmental applications such as photonics, electronics, catalysis, biosensors and water remediation [63]. Among the various oxide materials, cerium oxide (CeO_2) with its size and shape dependent optical properties [64] attracted the research community as promising material for a wide range of applications such as catalysis [65,66], active component in solid oxide fuel cell [67], sensors [68], irradiation protector [69], water purification by photocatalysis [70], surface coating for high-temperature oxidation protection [71], solar fuel production [72] and biomedical applications [69,73]. Cerium is known to exhibits two valence states Ce^{4+} and Ce^{3+} and is a most naturally abundant material. Thus, the presence of Ce^{3+} on the surface of the ceria nanostructures can influence the optical properties and catalytic activity [74,75]. The very low or no toxicity nature of the ceria nanoparticles made them

as effective radioprotectants for normal tissues [69]. The auto-regenerative antioxidant cycle (Ce^{3+} → Ce^{4+} → Ce^{3+}) on the surface of the ceria nanostructures was considered as a key factor for its radio-protective action. Ceria based nanocomposites found to be suitable for the environmental applications like water treatment [70], CO removal by catalytic oxidation [76] and methanol decomposition for syngas generation [14]. It was reported that the catalytic performance of ceria based nanocomposites was influenced by the morphology and size of ceria nanostructures [14,70]. Several research groups adopted various synthesis routes like reverse micelles [77], deep eutectic-solvothermal [78], nitrate-fuel combustion [79], pulsed laser deposition (PLD) [80], sonochemical [81,82] and hydrothermal techniques [83] for the synthesis of CeO_2 nanostructures. The optoelectronic and catalytic properties of the ceria nanostructures are found to be strongly influenced by the size-related lattice parameter changes, morphology, and defects concentrations [65,66,84,85]. Maria et al. discussed the confinement effects on the lattice parameter, microstrain and the optical bandgap in ceria nanoparticles [86]. Chen et al. reported about the size-related lattice parameter changes and surface defects in ceria nanocrystals [87]. They observed both lattice expansion and a more unusual lattice contraction in ultrafine nanocrystals. Thi et al. showed that the chemical reactivity was influenced by the size, shape, channel curvature, morphology, and microstructure (dislocations, grain-boundaries) of ceria nanomaterials [88]. They reported that the reactivity in ceria nanostructures was tunable with strain and shape of the nanostructures. The relaxation of microstrain in ZnO nanostructures favored the enhancement in visible region luminescence [89]. Pardeshi et al. reported that the photocatalytic degradation efficiency of ZnO nanostructures was found to decrease with the increase of crystallite size [90]. Similarly, Feng et al. observed an enhanced photocatalytic activity in BiOBr nanosheets and the same was attributed to improved charge separation due to low-strain [91]. Therefore, the morphology, crystallinity,

and microstrain are governing factors for better photocatalytic activity in ceria nanostructures. As a consequence, the controllable synthesis of ceria nanostructures with various morphologies and the understanding of their structural (lattice changes, microstrain) and optical properties (band gap and luminescence) are highly important for the usage of these materials in various applications. In this point of view, the synthesis of ceria nanostructures with well-defined morphology at low cost and lower reaction time has been attracted us to achieve the desired material with targeted applications. The application of commercial microwave oven for the synthesis of nanostructures has advantages like the ultrafast formation of the nanostructures, energy and time saving, economic and versatile control over the morphology by the variation of the power and time of irradiation. In this synthesis technique, the power and irradiation cycles are the main important experimental conditions whose variation can result in different morphological nanostructures. To the best of our knowledge, there are very few reports, specifically on ceria nanostructures, about the influence of these parameters on their synthesis, structural and optical properties. The CeO_2 nanostructures known to exhibit an optical direct and indirect band gaps of about ~3.6 and 5.5 eV which corresponds to the transition of valence band (O *2p*) to 4f0 (Ce *4f* state) and 5d (Ce *5d* state), respectively. The band gap of CeO_2 nanostructures known to be greatly influenced by the size, morphology and dopants [81,82,86]. In general, the band gap of CeO_2 nanostructures exhibits blue or redshift based on the size and the concentration of Ce^{3+} over the surface. Apart from the bandgap related emission in ceria, the presence of oxygen related defects (F-centers) was also involved in the observation of the room temperature photoluminescence (PL) in the visible range [92]. As a result, the visible emission in CeO_2 nanostructures is due to the hopping from different defect levels to O *2p* band. The changes in size, shape and defects which are controllable by varying the synthesis conditions are needed to be discussed.

2.3. Core shell nanostructures

Over the past few decades with the development of nanotechnology, the concept of core shell nanostructures (CSNs) have attracted enormous owing to explore advanced materials for novel applications. Moreover, the thin surface layer on nanoparticles were found to change their functionalities and properties substantially, likewise chemical reactivity [21], thermal stability [22,23], magnetic, optical and electronic properties [9,93]. Thus, it opened a gateway for these materials in order to apply in several disciplines including, such as catalysis, biosensors, nanomedicine, cosmetics and water remediation, optics, and electrical industry [13,24–26].

2.3.1. Synthesis of core shell

The similar synthesis and fabrication techniques for nanomaterials are also applicable for core shell nanostructures. The core shell nanostructures possess modified properties which are considered as highly functional materials, where the thermal stability or reactivity can be altered by tuning the cores, as well as the shells of these nanostructures. Due to this marvelous behavior of such materials, these can be employed in extensive variety of applications. The researchers are gaining interest towards the synthesis of these nanostructures because the demand of these core shell nanostructures has been increasing day by day. Various synthetic methods for preparing those core shell nanostructures are being reported by researchers, which includes sol-gel reduction, coprecipitation, cation-exchange, hydrothermal and polyol method. The hydrothermal and coprecipitation synthesis technique are two more effective and facile with high efficiency are adopted for this thesis work. Apart from synthesis methods, coprecipitation and hydrothermal synthesis of core shell nanoparticles with control over the shape and size are very suitable methods.

2.3.2. Synthesis of core shell nanoparticles by coprecipitation

In coprecipitation method, the reaction occurs in liquid phase and product is made in solid (powder) form. The mechanism of this synthesis involves nucleation, growth and agglomeration or aggregation. Nucleation step occurs at a fast rate when there is very low solubility of the material. In the growth step, particle consisting of only few atoms diffuses toward the surface of nuclei. In the final step of agglomeration process, small sized particles get fuzzed into large sized particles due to Oswald ripening and decrease in solid-liquid interface area [27]. Among the different liquid-solid transformation methods coprecipitation technique is much facile method for the synthesis of these core shell.

2.3.3. Synthesis of core shell nanoparticles by hydrothermal

The hydrothermal method involves the synthesis of nanomaterials using a close reaction vessel where physical and chemical processes flowing in aqueous solution at temperature usually above 100°C. The main advantage of this technique comprises the capability to prepare nanostructures of good quality and the capability to synthesize crystals of materials, which are usually unstable near the melting point [94]. For hydrothermal process Teflon container with proper sealing can endure high pressure and temperature for a long duration to provide an exaggerated condition for nanomaterials synthesis. Mukhlis et al. used the combination of hydrothermal and chemical method for the preparation of gold nanosphere on the surface of ZnO [26]. Tok et al. has prepared CeO_2 nanoparticles (NPs) by hydrothermal method [95]. Li et. al. reported the one step synthesis of TiO_2@MoO_3 core shell nanomaterials [96]. Hydrothermal synthesis is also considered as an attractive technique for synthesizing the core shell nanostructures. This technique provides moderate pressure and temperature, which helps in prominent interaction of the raw materials during the synthesis.

2.4. Nucleation and growth

Nucleation and growth are basic phenomena that ply vital roles in processing of various materials such as semiconductor, quantum dots, and some materials crystals. Nucleation is a thermodynamic model whereby seeds act as templates for crystal growth. Primary nucleation is the case of nucleation without the presence of other crystalline material [97]. This phenomenon can be used to describe the nucleation of many chemical syntheses. The nucleation process can be considered thermodynamically by looking at the total free energy of a nanoparticle defined as the sum of the surface free energy and the bulk free energy. For a particle with radius r, the surface energy γ and the free energy of the bulk crystal ΔG_v are related to total free energy ΔG, by the following equation [97];

$$\Delta G = 4\pi r^2\gamma + \frac{4}{3}\pi r^3 \Delta G_v$$

where free energy of the bulk crystal (ΔG_v) determined by $\Delta G_v = \frac{-k_B T \ln(s)}{v}$. Due to the surface free energy as always being positive and the crystal free energy as always being negative, it is possible to find a maximum free energy of which a nucleus can pass through to from a stable nucleus. By differentiating ΔG with respect to radius and setting it to zero $\frac{d\Delta G}{dr} = 0$, gives a critical free energy. The critical radius corresponds to the minimum size at which particles can survive in solution without being re-dissolved ΔG_{crit} can calculated by $\Delta G_{crit} = \frac{4}{3}\pi\gamma r_{crit}^2$, where $r_{crit} = \frac{-2\gamma}{\Delta G_v}$.

The Fig. 2-1 has been provided with the details about the free energy of particles where a critical free energy is required to obtain stable particles with in the solution.

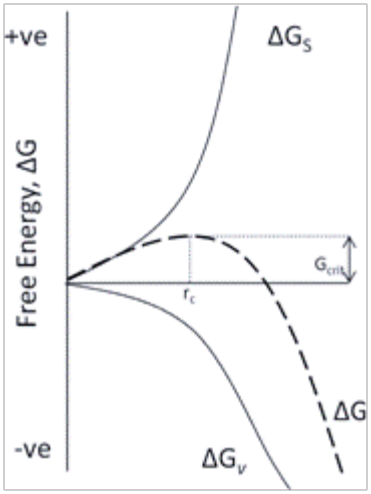

Fig. 2-1 Free energy diagram for nucleation of a critical nucleus [98].

In nucleation and growth, material transport by diffusion and its effect on the size (radius) of the critical nucleus often plays a fundamental role in controlling the size of the products [99]. In particular, growth by diffusion has been studied as it applies to various problems such as precipitation liquid droplet, and colloidal particles formation from solution [100]. The problem of nucleation and growth of the core shell nanostructures consider the two step nucleation in a three phase system. Initially, the pre-critical nucleus of the intermediate metastable phase; next, the stable crystal core in the solution. In such a case, the core shell critical nucleus forms through the diffusion of materials, which must occur in two steps; bulk diffusion in original mother solution and diffusion in the surrounding shell of the intermediated metastable solution. Furthermore, the released OH^- hydroxyl ion in way affects the nucleation and growth behavior of CeO_2 on surface of ZnO. An optimized OH^- concentration ascertains the metal-oxygen-metal bond in an order fashion. On the other hand at low temperature the presence of four symmetrically placed N atoms and the overall cubic symmetry of HMTA molecule allow the formation of up to four hydrogen bonding interactions: N-H...O, O-H...O, C-H...O, and N-H…N the formation of N…H bond involves mainly the unpaired electron of the nitrogen atom.

2.5. Raman spectroscopy

Raman spectroscopy is based on the phenomenon called Raman scattering, named after Indian scientist Raman who first discovered it in 1928. In Raman a sniggle frequency light usually from s single mode laser source, shines on the sample and scattered light is measured off the angle with respect to the incident light to minimize Rayleigh scattering. The energy difference between the scattered and incident light called Raman shift, usually given in wave number $cm^{-1}=1/\lambda$, equals to the vibrational or phonon frequencies of samples. According to group theory, at the center of *Brillouin* zone phonon modes are represented by $\Gamma = 2 \times (A_1 + B_1 + E_1 + E_2)$. The phonon modes can split into acoustic modes $\Gamma_{aco} = A_1 + E_1$ and optical modes $\Gamma_{opt} = A_1 + 2B_1 + E_1 + 2E_2$. The polar modes A_1 and E_1 are active in infrared as well as Raman scattering phenomena. Furthermore, Raman spectra of ZnO exhibits modes related to first order activities such as $E_{2,low}$, $E_{2,high}$, polar optical phonons and second order processes such as $E_{2,High}$-$E_{2,Low}$, $TA+LO$, etc. Usually the polar modes can split into transverse optical (TO) and longitudinal optical (LO) activity related modes. The $E_{2,Low}$ mode is related to the movement of zinc atoms and the $E_{2,High}$ mode is related to the vibration of oxygen atoms in the sub-lattice. The B_1 mode is usually called as silent mode because they neither Raman nor infrared active.

2.6. Optical properties

The core shell nanostructures offer attractive optical properties with the possibility of tuning these properties by varying the shape, size, and the type of material. The optical properties including the absorbance and emission properties gets effected by the nature of materials and thickness of shell materials. The thickness of shell materials effect not only the band position but also the intensity of absorption. Lu et al. [101] reported that the increment in the shell thickness of SiO_2 on the Au nanoparticles resulted in the rise of intensity of absorption of Au-SiO_2. The

photoluminescence (PL) of materials refers to the reemission of photons from nanostructures after absorbing incident photons. Normally, the band gap of a bulk material governs the emission center of the material. Thus, absorption and emission has been considered as the characteristic properties of a material. At nanoscale, these optical has been considered to be the function of the structural properties of the nanomaterial. Thus tunability in the wide range of a spectrum can be achieved in nanomaterials. Particularly in the case of core shell nanostructures by varying the thickness of core or shell materials the band and the PL properties can be tuned to the desired range of the spectrum.

The luminescence quantum yield of the core shell nanostructures has been reported to be better than their counter individual nanoparticles. Reiss et al. reported [102] that by increasing the shell thickness the intensity of emission was increased. The thickness of shell can be varied by simply modifying reaction time and quantity of precursors in the reaction. The alternation in the spectra can be achieved by varying the shape and size of the core and shell as well. Pan et al. reported about the variation in the PL spectra of CdS coated alternatively with CdSe and CdS [103]. The PL intensity was minimum with the CdSe coating, however, it was increased as the layer of CdS and CdSe were increased. The scattering of light in the core shell nanostructures is also influenced by the size of core shell nanostructures [41]. The maximum and minimum of scattering pattern shifts in perpendicular and parallel plane can be effected by radius and refractive index.

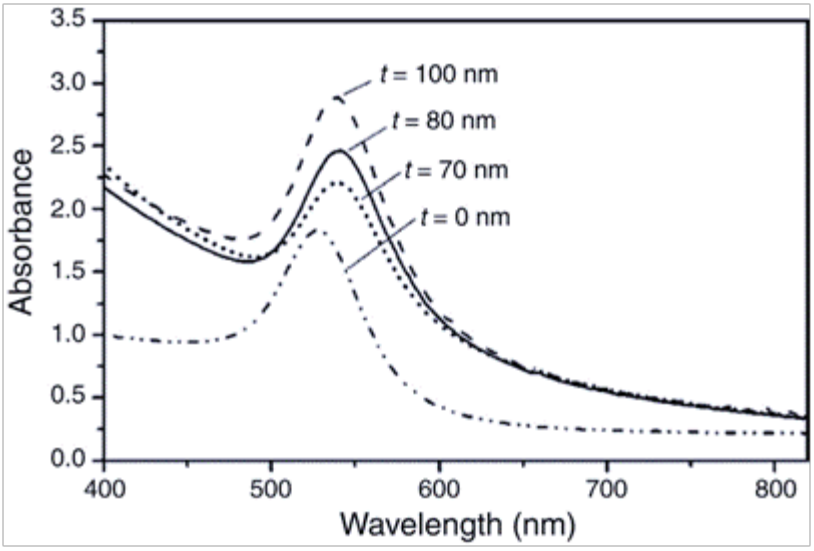

Fig. 2-2 UV-Vis absorption spectra of Au-SiO_2 core shell [101].

As a final point, to further enhance the photocatalytic activity and UV absorption of CeO_2 nanoparticles, large amounts of investigation on CeO_2-base composite were carried out, among them ZnO and CeO_2 composite materials have been studied for the higher efficient photocatalysis and UV filter [104]. Selvi et al. reported ZnO can be used as a shell material in order to tune the surface features of CeO_2 nanoparticles. Coating with ZnO is expected to improves the properties of both core and shell materials [105]. The ZnO@CeO_2 is an ideal host material for UV absorption in cosmetic sunscreen. Coting with CeO_2 is expected to improve the properties of core (ZnO) material. The present research aimed to fabricate the ZnO@CeO_2 core shell nanostructure as well as to control the shell thickness and to investigate their structure and optical properties.

2.7. Hypothesis

The synthesis of nanoparticles of ZnO, CeO_2 and their core-shell nanostructures through solvothermal (co-precipitation), and hydrothermal routes is studied and optimize the core-shell nanostructures to enhance the efficiency of UV observation.

2.8. Objectives

General Objective

To study the development of ZnO-CeO_2 / CeO_2-ZnO core shell nanostructure by solvothermal (co-precipitation) and hydrothermal methods in order to identify their ability to the absorption of UV radiation.

Specific Objectives

Task 1 Synthesis and tuning of CeO_2, ZnO, CeO_2-ZnO and ZnO-CeO_2 core shell nanostructures through solvothermal, and hydrothermal methods. The tuning parameters as it follow;

(i) Time of reaction, and

(ii) Concentration of precursors.

Task 2 XRD, XPS and Raman spectrometry will be used in order to identify characterization of crystal nature.

Task 3 To identify the core-shell and their thickness through TEM, HRTEM.

Task 4 To study functional properties ability attenuation of UV radiation in the UVA and UVB of different nanostructures through absorption and photoluminescence spectroscopies.

Task 5 Evaluation of efficiency of UV observation.

2.9. Methodology

Two different synthesis methods which comprises of solvothermal and hydrothermal have been used to synthesis of nanoparticles and core shell nanostructures. The structural, morphological and functional properties have be studied. In addition to the synthesis route, concentration, time and other variables affected the morphology, size of core and shell thickness which were influenced the optical properties of core-shell nanostructures. The schematic representation of the methodology is shown in Fig. 2-3.

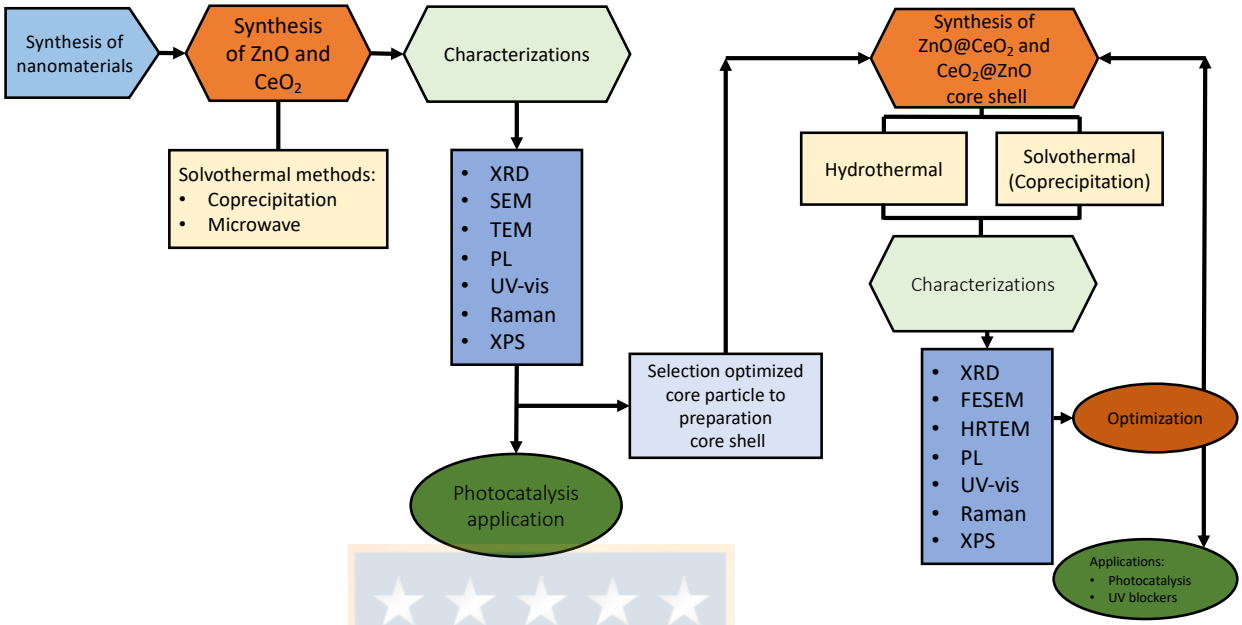

Fig. 2-3 Schematic diagram of various steps for the preparation of ZnO, CeO_2 and their core shell nanostructures.

Chapter 3

EXPERIMENTAL

3.1. Synthesis of zinc oxide nanoparticles

All the chemicals such as zinc nitrate hexahydrate ($Zn(NO_3)_2 \cdot 6H_2O$), Zinc acetate dihydrate ($Zn(CH_3COO)_2.2H_2O$), Sodium hydroxide (NaOH) and Hexamethylenetetramine ($C_6H_{12}N_4$) used in the experiment were of high purity reagents purchased from Sigma-Aldrich and used without any further purification. In a typical reaction, the rod shaped ZnO nanostructures were prepared by mixing aqueous solutions of 0.1 M of $Zn(NO_3)_2 \cdot 6H_2O$ with 0.1 M of HMTA and the resulting mixture was refluxed for ~3 h at ~95^{o}C. The obtained white colored precipitate was washed with ethanol and double distilled water. The precipitate was dried in a hot air oven at ~60^{o}C for ~5 h. The final product was calcinated at 500^{o}C for ~1 h for the improvement in crystallinity. Thus the samples prepared with varying HMTA are referred with code names M1, M2, M3 and M4 which corresponds to 0.01, 0.025, 0.05 and 0.1 M of HMTA, respectively. Similarly, the samples which were prepared with fixed amount of precursors (0.1 M of $Zn(NO_3)_2 \cdot 6H_2O$ and 0.1 M of HMTA) and by varying the time of reaction are code named as T6, T12 and T18 based on the refluxing time of 6, 12 and 18 h, respectively.

The ZnO spherical was prepared through a simple wet chemical precipitation technique and the preparation is as follows; 50mM of zinc acetate dihydrate and 50mM of sodium hydroxide were dissolved in ethanol (500mL), separately. Then the NaOH solution was added dropwise into $Zn(CH_3COO)_2 \cdot 2H_2O$ solution and the mixed reactants were refluxed for 3 hours at 90 °C and then allowed to cool to room temperature. The obtained products were washed with ethanol and water several times to remove the unreacted products, and then dried in a hot air oven at 100 °C for about

6 hours. The obtained asprepared ZnO rods were calcinated at 500°C for 1 hour in an air atmosphere.

3.2. Synthesis of cerium oxide nanoparticles

All the chemical reactants were purchased from Sigma-Aldrich, Merck and used without further purification. The synthesis of pure CeO_2 nanostructures was performed by using commercial microwave oven (2.45 GHz, P=990 W, with an option to preselect the operating power) operating at different powers (10%, 50% and 100% of P) for different time durations. In a typical synthesis, 50 ml (0.05 M) of cerium nitrate solution was mixed with 50 ml (1.5 M) of NaOH solution under magnetic stirrer for 3 min. The resultant reactants mixture was subjected to microwave irradiation by operating at low power (L=10% of P) for 4, 8 and 12 min with an interval of 2 min (1 min of cooling for each interval) to avoid any overheating or damage of the reactants during the irradiation. The resulting precipitates were collected by washing and drying. The samples were codenamed as L4, L8 and L12 based on the power and irradiation time of 4, 8 and 12 min, respectively. In the same custom, the samples prepared with medium power (M=50 % of P) for 4, 8 and 12 min of irradiation time were codenamed as M4, M8 and M12, respectively. Likewise, the samples prepared with high power (H=100 % of P) were codenamed as H4, H8 and H12 based on the irradiation time of 4, 8 and 12 min, respectively.

To prepare cubic CeO_2 nanoparticles, 0.05M of $Ce(NO_3)_3.6H_2O$ and 4M of NaOH by a magnetic stirrer for 30 min at ambient temperature. The resultant reactant was transferred in to a Teflon lined autoclave and kept at 180°C for 12 h washed with ethanol and double distilled water to remove the unreacted reagents and dried in a hot air oven at 80°C for 6 h.

3.3. Synthesis of CeO_2 decorated ZnO nanostructures

500 mg of the prepared CeO_2 nanoparticles with 500 mg of Polyvinylpyrrolidone Mw~10000 (PVP) and 600 mg of $Zn(NO_3)_2.6H_2O$ were mixed in 40 mL double distilled water by a magnetic stirrer. Then 0.1M of NaOH solution was added to the above solution and stirred for 30 minutes. The obtained solution was then transferred to the Teflon lined autoclave and kept at 180°C for 12 h for hydrothermal treatment. The obtained products were filtered out, washed with ethanol and double distilled water to remove the unreacted reagents and dried in a hot air oven at 80°C for 6 h.

3.4. Synthesis of ZnO@CeO_2 core shell (Rod)

The prepared ZnO rod (25 mg) were dispersed ultrasonically in a mixed solution of water (20 mL) and ethanol (20 mL). Then, cerium(III) nitrate hexahydrate ($Ce(NO_3)_3 \cdot 6H_2O$ (8.6 mg) was added into the above solution and sonicated for 15 min. Then the 15, 30 or 50 mL of HMTA solution (0.02 g L^{-1}) were added into the final mixture separately, in order to tuning shell thickness, and the temperature of the mixture was increased to 90 °C and kept under reflux for 2 h before being cooled to room temperature. The products were collected by centrifugation and washed with water and ethanol to remove unreacted products. The obtained products were dried at 100 °C for 6 h and followed by calcination at 350°C for 1 hour.

3.5. Synthesis of ZnO@CeO_2 core shell (Spherical)

To synthesis of ZnO@CeO_2 core shell with spherical morphology used the prepared ZnO spherical (25 mg) were dispersed ultrasonically in a mixed equal solution of water and ethanol. Then, cerium(III) nitrate hexahydrate (8.6 mg) was added into the above solution and sonicated for 15 min. Then the 30 ml of HMTA solution (0.02 g L^{-1}) was added into the final mixture and the temperature of the mixture was increased to 90 °C and kept under reflux for 2 h before being

cooled to room temperature. The products were collected by centrifugation and washed with water and ethanol to remove unreacted products. The obtained products were dried at 100 °C for 6 h and followed by calcination at 350ºC for 1 h.

3.6. Characterization techniques

The characterization of nanomaterials is extremely important for understanding the physical and chemical properties for possible application. From developing a new synthetic technique to testing the quality control of an existing technique, characterization aids in the correct identification of phases, impurities, and formation of core shell. Because of its importance to the advance of quality scientific research, the following sections will review some basic characterizations described in less detail.

In this part, an overview of current technology appraisal for the morphological, microstructural, optical, electrical characterizations of semiconductor and core shell nanostructures are discussed. Understanding the structural properties of core shell structures assist their diverse applications. In the perceptive of core shell nanostructures, the nucleation and growth processes with representative characterization techniques are briefly mentioned with recent examples based on structural properties. Also, the significant development and progress in the field of characterization techniques useful for the investigation of core shell nanostructures is discussed.

3.6.1. X-Ray diffraction (XRD)

During the course of this research work, crystalline nature and phase purity were examined through powder X-ray diffraction (XRD) technique by using Bruker, D4 Endeavor, Cu-Kα radiation, 40 kV and 30 mA, in the range of 20−80° diffraction angle range.

The lattice parameters '*a*', '*c*' and unite cell volume (*v)* of ZnO were calculated through the following relations:

$$a = \frac{\lambda}{\sqrt{3}\sin\theta}\left(h^2 + hk + k^2\right)$$

$$c = \frac{\lambda}{\sin\theta}$$

$$v = \frac{\sqrt{3}a^2 c}{2}$$

The influence of reaction conditions on bond length (*L*) of Zn-O was calculated by using the relation [106,107]:

$$L = \sqrt{\left(\frac{a^2}{3}\right) + \left(\frac{1}{2} - u_p\right)^2 c^2}$$

where, 'u_p' is the positional parameter which is a measure of the amount by which each atom is displaced with respect to the next atom along the *'c'* axis. The 'u_p' parameter can be calculated by the formula [108]:

$$u_p = \left(\frac{a^2}{3c^2}\right) + 0.25$$

Williamson-Hall (W-H) had proposed that the microstrain and crystallite size [109] induced broadening are major factors for the diffraction peak broadening and is expressed by the following mathematical expression:

$$\beta_{hkl} = \beta_D + \beta_\varepsilon$$

where, β_D is the line broadening due to crystallite size, β_ε is line broadening due to strain and β_{hkl} is the observed full width at half maximum (FWHM) of diffracted peak. In addition, instrument also would contribute to the peak broadening and to decompose line broadening effect

from the instrumental contribution, standard silicon (*Si*) sample diffraction pattern was used. The instrumental corrected line broadening of each diffraction peak is obtained from the following relation [110]:

$$\beta_{hkl} = \left[(\beta_{hkl})^2_{measured} - \beta_{instrumental} \right]^{0.5}$$

where, $\beta_{instrumental}$ is the broadening due to the instrumental contribution. The diffraction peaks were fitted using *Lorentzian profile* to calculate full width at half maximum (FWHM) for further analysis. The peak broadening due to crystallite size diameter (*D*) contribution can be calculated by using Scherer formula [111,112]:

$$\beta_D = \frac{k\lambda}{D\cos\theta}$$

where, *k* is the shape factor, λ is the *X-ray* wavelength and θ is the Bragg angle [113]. Similarly, strain induced peak broadening can be obtained through the relation:

$$\beta_\varepsilon = 4\varepsilon \tan\theta$$

where, 'ε' is the microstrain. Thus, the line broadening due to the combination of broadening induced by the crystallite size and microstrain can be represented as:

$$\beta_{hkl} = \left(\frac{K\lambda}{D\cos\theta} \right) + (4\varepsilon \tan\theta)$$

This can be further simplified as follows and is known as Uniform Deformation model (UDM)

$$\beta_{hkl}\cos\theta_{hkl} = \left(\frac{K\lambda}{D} \right) + (4\varepsilon \sin\theta_{hkl})$$

The values of micro strain were obtained from the plot of $\beta_{hkl}\cos\theta_{hkl}$ *vs.* $4\sin\theta_{hkl}$. By using the value of *D*, the dislocation density (δ) can be obtained through the relation $\delta = \frac{1}{D^2}$ [114].

For CeO_2, considering the (111) plane in order to the lattice parameter "*a*" and the unit cell volume "*V*" are calculated by using the relation

$$d = \frac{a}{\sqrt{h^2} + k^2 + l^2}$$

where, d is the inter-planar spacing. For W-H analysis, uniform deformation (UD), UD stresses (UDS), and UD energy density (UDED) models are considered [79,89].

For UDS model the, the isotropic strain is replaced by the deformation stress (σ) using the relation $\varepsilon_{hkl} = \frac{\sigma}{E_{hkl}}$, where E_{hkl} is the Young's modulus in the direction perpendicular to the corresponding diffraction plane [89]. The Young's modulus for the cubic crystals can be obtained by using the relation

$$\frac{1}{E_{hkl}} = S_{11} - (2S_{11} - 2S_{12} - S_{44})\left[\frac{k^2l^2+l^2h^2+h^2k^2}{(h^2+k^2+l^2)}\right],$$

where $S_{11} = 22.9 \times 10^{-12}$, $S_{11} = 22.1 \times 10^{-12}$, $S_{11} = -9.80 \times 10^{-12}$ are elastic compliances (m^2N^{-1}) of cubic crystals [79]. By considering the UDS model, the slope from the plot of $\beta_{hkl}\cos\theta_{hkl}$ *vs* $[4\sin\theta_{hkl}\,(E_{hkl})^{-1}]$ is used for obtaining the stress value for all the samples. For UDED model, the deformation energy density (u) which is related to the lattice strain by Hooke's relation $u = \varepsilon_{hkl}^2 \frac{E_{hkl}}{2}$ is obtained from the plots of $\beta_{hkl}\cos\theta_{hkl}$ vs $\left[\frac{2^{5/2}\sin\theta_{hkl}}{\sqrt{\theta_{hkl}}}\right]$.

3.6.2. Microscopic Characterization

The characterization with high resolution imaging techniques using electromagnetic radiations of shorter wavelength are presently in use for the detailed characterization of nanostructures. Diverse morphological characterization can be easily done with the help of various microscopic techniques. Such as scanning electronic microscopy (SEM), field emission SEM (FESEM), transmission electron microscopy (TEM) and high resolution TEM (HRTEM).

3.6.2.1. SEM / FESEM

Size and shape analysis of nanostructures in broader study area are carried out with SEM and FESEM. Scanning the sample surface with electron beams in a raster scan pattern in SEM provides the information about surface topography and composition of nanostructures, when equipped with energy dispersive X-ray spectroscopy (EDAX) analysis. The basic concept with of SEM involves the analysis of backscattered and secondary electron that are emitted from the samples. Hence nanostructures having complicated topography can also be characterized with SEM *via* a characteristic three-dimensional appearance due to the relative narrower electron beam and greater depth of field analysis. A detailed SEM analysis provides information about the nature of nanostructures, as well as in-depth investigation on their degree of aggregation. FESEM has the advantage of higher magnification on contrast to conventional SEM. FESEM may provide the information about shell surface, whether smooth or rough. FESEM consists of field emission gun as an electron source in contrast to tungsten filament cathode in regular SEM. The morphology and aspect ratio of the prepared nanostructures were characterized by using scanning electron microscope (SEM, JEOL, JSM-6380, operated at 20 kV).

3.6.2.2. TEM / HRTEM

Internal nanostructure characterization, discrimination between core and shell material, core thickness and composition (when equipped with EDAX) of core shell nanostructures are analyzed with TEM. HRTEM is employed for getting the most precise information about the nanostructure, such as lattice fringes, d-spacing and crystallinity of nanostructures. Based on this we can easily differentiate between amorphous and crystalline materials, doped verses undoped and mono/bimetallic nanostructures that cannot be possible via SEM or FESEM techniques.

The morphology of the prepared samples, formation and average shell thickness and core diameter were analyzed by using a transmission electron microscope (TEM, JEM 2000 EX, operated at 200 kV).

3.6.3. Ultraviolet-visible spectroscopy (UV-Vis)

In ultraviolet-visible (UV-Vis) spectroscopy, high energy electromagnetic radiation in the wavelength range of 200-1000 *nm* will be utilized to promote the electrons to higher energy orbitals. Since orbitals have quantized energy, only certain transitions can occur in the UV-Vis region. The difference in the incident and transmitted beam give us information about the frequencies which are absorbed by the samples. Based on the absorbance data, the physiochemical properties of the samples can be analyzed. Among various spectroscopic methods, UV-Vis spectroscopy has been often used to characterize the optical properties of the nanoparticles. For this dissertation, UV-Vis spectroscopy was used to get information about the absorption band of pure and core shell nanostructures, besides the calculation of the band gap energy of the samples.

Optical characterizations were done by using UV-visible-NIR spectroscopic technique at room temperature. For optical characterizations, the solutions prepared by mixing 5 *mg* of prepared sample with 10 *mL* of distilled water through sonication for 15 *min* were used. The diffuse reflectance spectra (UV-visible-NIR spectra) of the nanopowders were recorded by using *Shimadzu UV–Vis 2550* spectrophotometer in the range of 300-800 *nm*.

3.6.4. Photoluminescence spectroscopy

Photoluminescence (PL) spectroscopy is a powerful toll to study the optical process in semiconductor and it is particularly sensitive to defects, since they often induce characteristic radiative transition cannels. A careful study of the large variety of defect related luminescence such as excitons, donor-acceptor pairs and two-electron satellites. In addition, the formation of

deep levels in the band gap that can serve as non-radiative channels for carrier recombination may be identified by their effect on the PL intensity. The PL is a non-destructive technique used for the determination of extrinsic and intrinsic properties of the semiconductors. In this technique, the semiconductor under investigation is exited using laser irradiation and the PL spectrum of the spontaneous emission from radiative recombination in the material band gap was acquired. In the present work, the PL spectroscopy, aqueous dispersions (0.5 mg/ml) of prepared samples were used. The steady state PL measurements were done by using a *Perkin Elmer* fluorometer with an excitation wavelength of 340 *nm*.

3.6.5. Raman spectroscopy

Information about the vibrational and electronic structures of semiconductor nanoparticles and core shell nanostructures can easily be obtained using Raman spectroscopy. Raman spectroscopy is recognized as the most influential methods among the recent characterization techniques and is based on the inelastic scattering of high power visible light by the nanostructure materials. The energy of irradiated and scattered light for both stokes and anti-stokes radiations are closely related with molecular vibration of nanostructures. Molecular level information related to the nature of chemical bond and symmetry of molecules could easily be characterized by analyzing the Raman shift. Crystalline order and in-plane crystallite size of core shell nanostructures can be conveniently measured by using Raman spectroscopy.

The phonon characteristics of the prepared ZnO nanostructures were analyzed by using Raman scattering measurements (*Thermo Scientific DXR Raman microscope*, 532 *nm*, 5 mW power).

3.6.6. X-Ray photoelectron spectroscopy (XPS)

XPS is a significant technique that suitable to explore the exact and precise information regarding the superficial and chemical composition of core shell structures. XPS analysis can be employed for in-depth analysis to get information about atomic composition. Chemical status of the surface element composition of nanoparticles or core shell, electronic state or mode of chemical binding of surface can also be analyzed. In the present work, the chemical state of prepared samples and their core shell was analyzed using a XPS Esclab 250.

3.7. Photocatalytic activity

For the photocatalytic activity studies, 150 *mL* of (5 *mg/L*) of methylene blue (MB) aqueous solution was considered as a model dye effluent. For the activity study, 20 *mg* of the prepared sample as a catalyst was added to the dye solution and the study was carried out in a double walled reaction vessel (250 mL) with provision for water circulation for maintaining the temperature during the light irradiation. To achieve the adsorption-desorption equilibrium between the catalyst surface and dye molecules, the mixture was kept in dark condition under constant stirring for 30 *min*. For irradiation, a visible light source (Halogen lamp, 7748XHP, 250 W, 24 V) was used. The aliquots were collected at frequent intervals and the catalyst was separated by using a polytetrafluoroethylene (PTFE) 0.45 μm filter. The optical absorption spectra of the aliquots were recorded by using a Shimadzu UV-Vis 2550 spectroscopy for monitoring the removal efficiency and degradation kinetics of the dye effluent with different catalysts.

Chapter 4

RESULTS AND DISCUSSION

4.1. ZnO nanostructures

4.1.1. Morphological analysis

For better understanding of the effect of the concentration of HMTA and the refluxing time on the morphology of ZnO, the SEM and TEM techniques were adopted. The microscopic images of the samples obtained from varying the concentration of HMTA are shown in Fig. 4-1 and the size parameters obtained from the TEM images were tabulated on Table 4-1. From Fig. 4-1, we witnessed that the concentration of HMTA played a crucial role on the morphology of ZnO structures. It was evident that the size and morphology drastically modified with increasing the concentration of HMTA. During the high temperature refluxing, the HMTA present in the solution influences the formation of $Zn(OH)_2$ seed nuclei by commencing the rapid hydrolysis of Zn^{2+} ions. The chemistry involved in the refluxing can be considered as:

$$(CH_2)_6N_4 + 6H_2O \rightarrow 6HCHO + 4NH_3$$

$$NH_3 + H_2O \rightarrow NH_4^+ + OH^-$$

$$Zn^{2+} + OH^- \rightarrow Zn(OH)_4^{2-} \rightarrow ZnO + H_2O$$

We observed that the sample prepared with lower HMTA (0.01 M) exhibited hexagonal six-sided prism like morphology with low aspect ratio. Upon increasing the concentration of HMTA in the synthesis, the morphology was gradually changed from prism to rod like formations. The sample prepared with moderate concentration of HMTA (0.05 M) exhibited a monodisperse hexagonal nanostructures with rod like morphology. Further increase in the concentration of HMTA worsen the morphology. Usually HMTA acts as a virtual shell around the ZnO nanostructures leads to the enhanced axial growth rate. As a consequence, in the presence of

HMTA due to rapid hydrolysis, the $Zn(OH)_2$ core nuclei get aggregated and led to the formation of the multipod structures with rod like morphology.

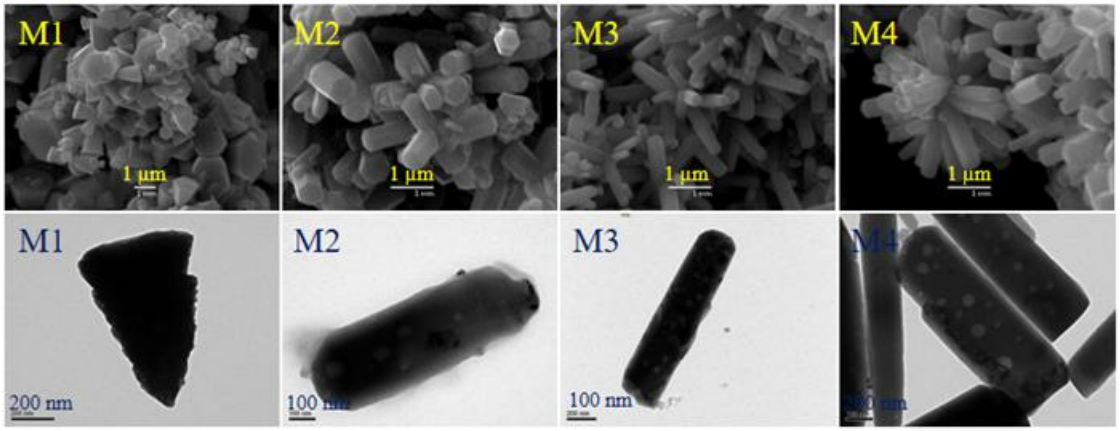

Fig. 4-1 SEM images (top row) and corresponding TEM images (bottom row) of the ZnO nanostructures prepared with different concentration of HMTA such as 0.01, 0.025, 0.05 and 0.1M which are code named as M1, M2, M3 and M4, respectively. The refluxing time is fixed as 3h for this set of samples.

Thus it is very clear that the ratio of the precursors [P=(Conc. Zinc nitrate)/(Conc. HMTA)] strongly influenced the growth rate and morphology of the nanostructures under similar reaction conditions. In the present study, the ratio of the precursors was 10, 4, 2 and 1 corresponds to 0.01, 0.025, 0.05 and 0.1 M of HMTA, respectively. From the size parameters obtained from the TEM images we observed that the aspect ratio of the nanostructures increased with the increasing the concentration of HMTA up to 0.05 M and then shown a decreasing trend with further increase in the concentration of the HMTA. Parize et al. [115] reported about the effect of HMTA on the growth ZnO nanowires by chemical bath deposition (CBD) and concluded that a slight excess of HMTA when compared to Zn precursor was suitable in obtaining a high axial growth rate. Whereas, in our study a merely equal concentration of HMTA led to the deterioration of

monodispersed rod like nanostructures with decreased aspect ratio. The sample (M3) obtained for 3 h of refluxing time (for P=2) exhibited nearly monodisperse hexagonal rods with diameter and length as ~0.286 and 1.263 μm, respectively. Thus, the moderate value of P (=2) corresponds to favourable concentration of HMTA for the formation of hydroxyl ions that led to the rapid nucleation process and influenced the length of the rods.

The sample (M4) obtained for 3 h of refluxing time (for P=1) exhibited nearly hexagonal rods with varying diameter. So, in the next step with an intention to improve the morphology, we fixed the concentration of HMTA (as 0.1 M) and varied the refluxing time for understanding the influence of it on the morphology. The microscopic images of the samples obtained from varying the refluxing time are shown in Fig. 4-2 and the size parameters obtained from the TEM images were tabulated (see Table 4-1). We observed that with the increase of refluxing time the samples possessed merely rod like morphology with a wide size distribution. The samples obtained for 3 h of refluxing time (M4) exhibited hexagonal rods with varying diameter and length ~(0.273 to 0.132) and ~(0.783 to 0.793) μm, respectively. These parameters for the sample obtained from the refluxing time of 6 h were increased, perhaps the morphology was changed to multipod structures with sharp tips. The sample obtained from 12 h of refluxing exhibited an aggregated bipod like nanostructures with polydisperse diameter values. Whereas the sample obtained from the 18 h of refluxing time exhibited bipods and broken rods with a typical diameter and length as ~0.555 and ~1.180 μm, respectively. The aspect ratio was increased for the samples (T6, T12) prepared by 6 and 12 h refluxing time when compared with the sample (M4) prepared by 3 h of refluxing. Further, the aspect ratio was drastically decreased for the sample prepared by 18 h of refluxing time. From the Fig. 4-2 it is evident that the rod like morphology was gradually deteriorated with

increase in the refluxing time. Thus, it indicates that prolonged reaction time led to the aggregated fusion of the nanostructures and deterioration of the morphology.

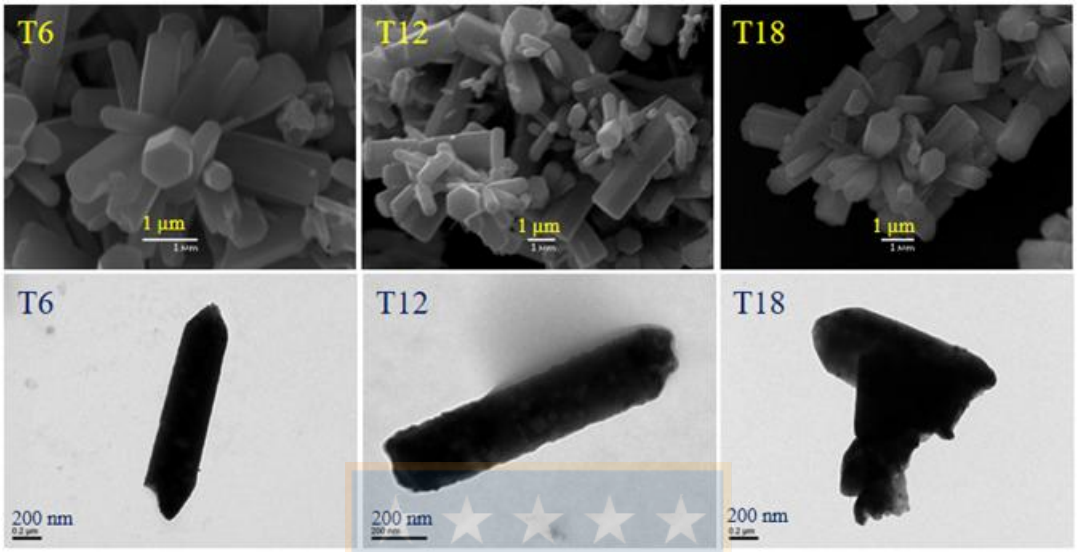

Fig. 4-2 SEM images (top row) and corresponding TEM images (bottom row) of ZnO nanostructures prepared with different refluxing times such as 6, 12 and 18 h. which are code named as T6, T12 and T18, respectively. The concentration of HMTA is fixed as 0.1 M for this set of samples.

Table 4-1 Experimental parameters, size parameters and morphology acquired from TEM are tabulated for comparison. For the sample M1 the diameter of the base of the prism is given in table for comparison.

Sample code	Experimental parameters				From TEM			Morphology
	Zinc nitrate (M)	HMTA (M)	P	Refluxing time (h)	Diameter (*nm*)	Length (*nm*)	Aspect ratio	
M1	0.1	0.01	10	3	470	780	1.66	Hexagonal six-sided Prisms.
M2	0.1	0.025	4	3	296	884	2.99	Hexagonal pellet like multipod structures.
M3	0.1	0.05	2	3	286	1263	4.42	Monodisperse hexagonal rods.
M4	0.1	0.1	1	3	273 132	783 793	2.87 6.01	Hexagonal rods with varying diameter.
T6	0.1	0.1	1	6	318	1442	4.53	Rod like multipod structures with sharp tips.
T12	0.1	0.1	1	12	236	1080	4.58	Polydisperse Hexagonal Bipods.
T18	0.1	0.1	1	18	555	1180	2.13	Bipods and broken rods.

4.1.2. X-ray diffraction

The XRD patterns of the prepared ZnO nanostructures with different reaction conditions are presented in Fig. 4-3. The XRD diffractions of ZnO with hexagonal wurtzite lattice in

agreement with the *JCPDS 36-1451.* The information of crystalline nature and microstructural parameters was obtained from the X-ray diffraction data. The absence of any additional peaks apart from that of ZnO within the XRD detection limits, signified the successful formation of ZnO nanostructures without any additional impurity phases. The lattice parameters of ZnO structures highly depends on various parameters like size, shape of the nanostructures, the concentration of foreign atoms, presence of defects and microstrain [111,116].

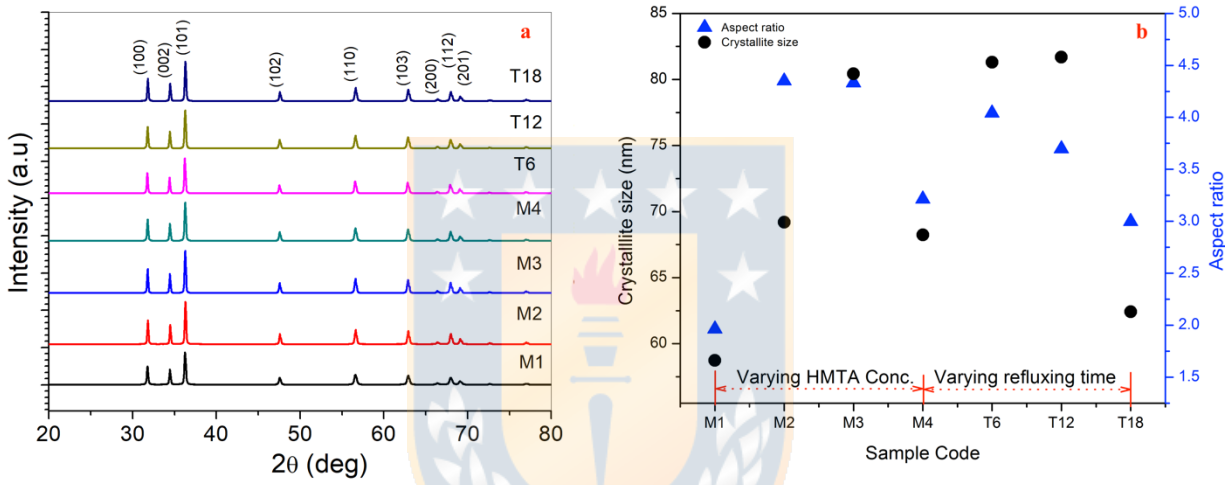

Fig. 4-3 (a) X-ray diffraction patterns of the prepared ZnO nanostructures **(b)** The variation of crystallite size and aspect ratio of the samples.

The diffraction peaks were fitted using *Lorentzian profile* to calculate full width at half maximum (FWHM) for further analysis. The lattice parameters and bond length values of ZnO were listed in tabulated on Table 4-2. In general, the broadening of XRD peak profile of a sample is due to the decrease the crystallite size and strain present in the lattice. The XRD technique is one of the simplest methods to quantify lattice strain [117].

Table 4-2 Various lattice parameters and the crystallite size (D), dislocation density (δ) and micro strain ($\mathcal{E}$) values obtained from the XRD data analysis are tabulated for comparison.

Sample Code	*a* (Å)	*c* (Å)	Unit cell volume *v* (Å^3)	*u*	*L* (Å)	*D* (*nm*)	δ ($\times 10^{11}$ $1/cm^2$)	$\mathcal{E}$ ($\times 10^{-3}$)
M1	3.248	5.200	47.488	0.380	1.976	61.11	2.67	2.20
M2	3.247	5.201	47.534	0.379	1.975	79.89	1.56	1.87
M3	3.244	5.196	47.368	0.379	1.974	79.74	1.57	1.82
M4	3.247	5.200	47.478	0.379	1.975	70.95	1.98	1.86
T6	3.251	5.207	47.659	0.379	1.978	77.46	1.66	1.92
T12	3.244	5.196	47.375	0.379	1.974	74.75	1.78	1.94
T18	3.247	5.201	47.486	0.379	1.975	69.25	2.08	1.97

The parameters obtained from the XRD data analysis are tabulated on Table 4-2. The variation of crystallite size and aspect ratio of the samples prepared with different experimental conditions is shown in Fig. 4-3b. The crystallite size is increased with the increasing concentration of HMTA up to 0.05 M of HMTA and it decreased for the sample with equimolar concentration of the precursors. The increasing refluxing time up to 12 h exhibited an increase in size and further increase in refluxing time led to decrease in the crystallite size. The crystallite size followed the trend of the aspect ratio as observed from the morphological studies. The decrease of microstrain with increase in the concentration HMTA supported the observations of monodisperse nanorods like morphology in sample M3. Similarly, the increased strain with an increase in the refluxing time supported the observation of fused nanostructures due to the merging of grains as a result of prolonged time of refluxion. Thus, from the XRD, SEM and TEM measurements it was evident that the sample (M3) prepared with P=2 and 3 h of refluxing time exhibited mono disperse rods like nanostructures with better crystallinity, lower microstrain and aspect ratio.

4.1.3. Diffuse reflectance spectra (DRS)

The reflectance spectra for all the samples in the range of 300-800 *nm* are shown in Fig. 4-4a. The band gap was obtained from the DRS spectra by using the *Kubelka-Munk* function [118] *(F)* which is defined as: $F = \frac{(1-R)^2}{2R}$

where *R* is the ratio of the reflectance of the sample and the reference. The *Tauc* plots i.e., the plot of $[F(R)\ hv]^2$ *vs* energy (*hv*) of all the samples are shown in Fig. 4-4b. The optical bandgap energies were obtained by extrapolating the linear portion of each plot. The band gap of the prepared nanostructures exhibited a variation from 3.18 to 3.3 eV and the observed values are lower than that of bulk ZnO (3.37 eV) [119]. The observed variation in the band gap values was associated with the variation in the crystallite size and micro strain obtained from XRD studies. It is well known that in metal oxide systems like ZnO the reduction in crystallite size results in a blue shift of bandgap (increase) due to quantum confinement effect [120,121]. For comparison, the variation of the band gap with crystallite size for different synthesis parameters is shown in Fig. 4-4c.

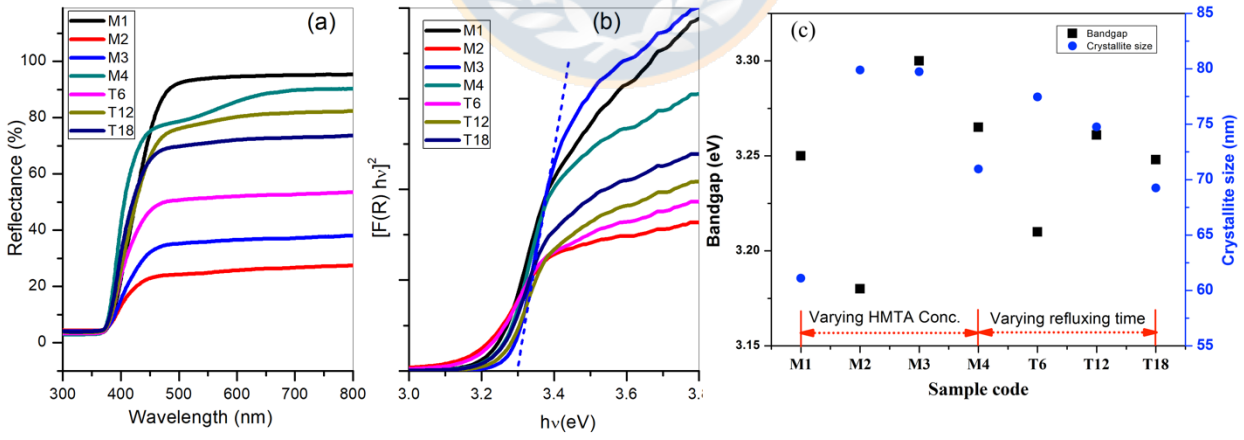

Fig. 4-4 (a) Diffuse reflectance spectra and **(b)** band gap measurements of the prepared ZnO nanostructures **(c)** Variation of crystallite size and band gap with the concentration of HMTA and refluxing time duration.

Table 4-3 Various bandgap and crystallite size (D) with the concentration of HMTA and refluxing time duration of ZnO.

Sample code	Bandgap (eV)	Crystallite size (D)
M1	3.25	61.11
M2	3.18	79.89
M3	3.30	79.74
M4	3.26	70.95
T6	3.20	77.46
T12	3.26	74.75
T18	3.25	69.25

The band gap value of the sample prepared with lower concentration of HMTA, which exhibited six-sided prism like morphology was about ~3.25 eV. Upon increasing the concentration of HMTA, the samples M2 exhibited a decrease in band gap (~3.18 eV). This decrease in the band gap was due to the increase in the crystallite size and change in morphology of the ZnO nanostructures [122]. In contrast, further increase in the concentration of HMTA, the band gap of the ZnO was increased and exhibited a maximum value of ~3.3 eV of all the samples. The observed highest band gap value in the case of sample M3 is attributed to the nature of monodisperse morphology with high crystallinity and lower microstrain when comparing with the other samples. These factors led to the observation higher NBE (near band edge) emission with less intense defects related emission which we discussed in the next section. It was evident that with further increase of HMTA, the band gap value of the sample prepared with equimolar concentration of precursors (M4) was about ~3.26 eV and the observed decrease was due to the polydisperse rod like morphology. The variation in the band gap value of the samples obtained by the increasing the refluxing time T6 (~3.2 eV) and T12 (~3.26) was attributed to the changes in the crystallite size. The band gap value of the sample T18 shown a little variation (~3.25 eV) when compared with the T12 and the observed decrease was due to the deterioration of the morphology [123].

4.1.4. Photoluminescence spectra

The photoluminescence (PL) spectra of the prepared samples are shown in Fig. 4-5. Generally, PL spectrum of ZnO consists of near band edge emission (NBE) related to free excitons and defects related visible emission from trap states with in the band gap of ZnO. The trap states related emission has a tendency to red shift when compared to NBE. All of our samples shown broad emission covering the UV-Vis region and the spectra were decomposed using the *Gaussian* profile and the obtained parameters were used for further analysis (Figs. 4-6 & 4-7). For instance, the emission spectra of all the samples exhibited five different emission bands at ~394, ~420, ~443, ~490 and ~532 *nm*. The emission peak located at ~394 *nm* (~3.14eV) was due to free exciton related NBE emission in ZnO nanorods [124,125]. In general, the emission peaks of ZnO in the visible region are due to various defects such as zinc vacancies (V_{Zn}), interstitial zinc (Zn_i), oxygen vacancies (V_o), interstitial oxygen (O_i) and surface dangling bonds. Theoretically, the Zn_i and V_o^* are located at 0.22 and 0.86eV below the CB, respectively. Also, V_o^{++} and V_{Zn} are located at 1.16 eV and 0.3 eV above the Valance band [126–128]. The native defects appear according to Frenkel and Schottky equation [128]. In the current study: (i) the emission peak centered around ~420 *nm.*

Table 4-4 The emission peak and related peak emission.

sample	Peak Positions		Related peak emission
	nm	eV	
M1, M2, M3, M3, T6, T12, T18	394	3.14	free exciton related near band emission (NBE)
	420	2.95	Electron hole recombination between the Zn interstitial defect (Zn_i) and valence band
	443	2.79	transition of electrons from the Zn vacancy (V_{Zn}^{2-}) to valence band
	490	2.53	recombination of the conduction band electron at defect level produced by the oxygen site (O_{Zn})
	532	2.33	recombination of electrons by oxygen vacancy (V_O)

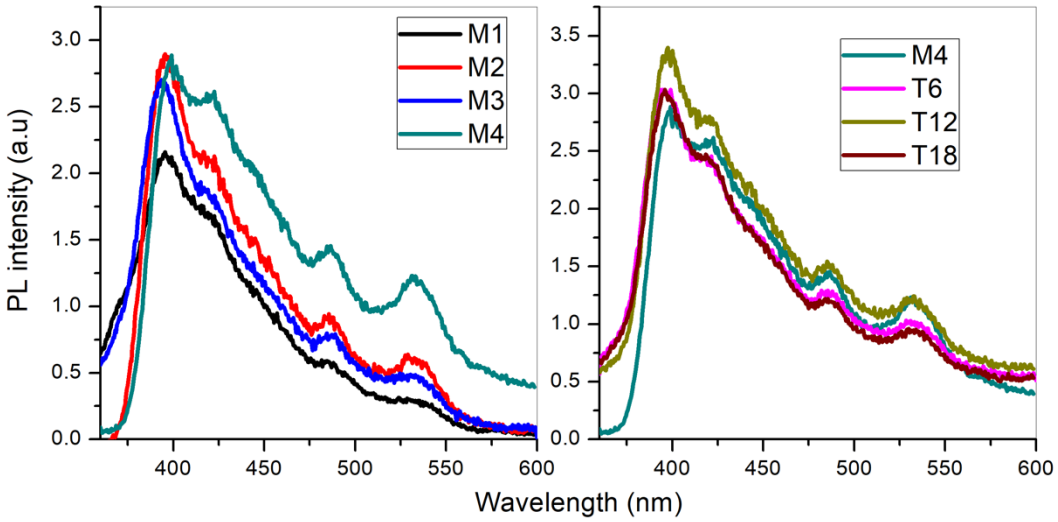

Fig. 4-5 Photoluminescence (PL) spectra of ZnO nanostructures prepared by (a) varying the HMTA and (b) varying the refluxing time. For comparison purpose the spectrum of the M4 is provided in the two sets. The excitation wavelength of 330 *nm* was used for recording the emission spectra for all the samples.

was attributed to the electron-hole recombination between the Zn interstitial defect (Zn_i) and valence band, (ii) the emission peak centered around ~450 *nm* was attributed to the transition of electrons from the doubly ionized Zn vacancy (V_{Zn}^{2-}) to the valence band, (iii) the emission band centered around the ~ 490 *nm* was arised due to the recombination of the conduction band electron at the defect level produced by the oxygen anti site (O_{Zn}) and (iv) the emission band around ~532 *nm* was due to the recombination of electrons with photogenerated holes trapped at the defect level produced by the oxygen vacancy (V_O) [129,130]. The schematic mechanism of free exciton recombination and various relevant native defect emissions are visualized (Fig. 4-8). Apart from these, the emission spectrum of sample M1 consists of small hump in the lower valley side of NBE emission and this small hump centered around the ~371 *nm* (~3.34 eV) was attributed to the recombination of surface exciton (SX) which originated from the broad energy distribution of near-surface states. The higher surface to volume ratio in the nanoprism like morphology when

compared with nanorods morphology contributed to the observation of the SX related emission in the sample M1.

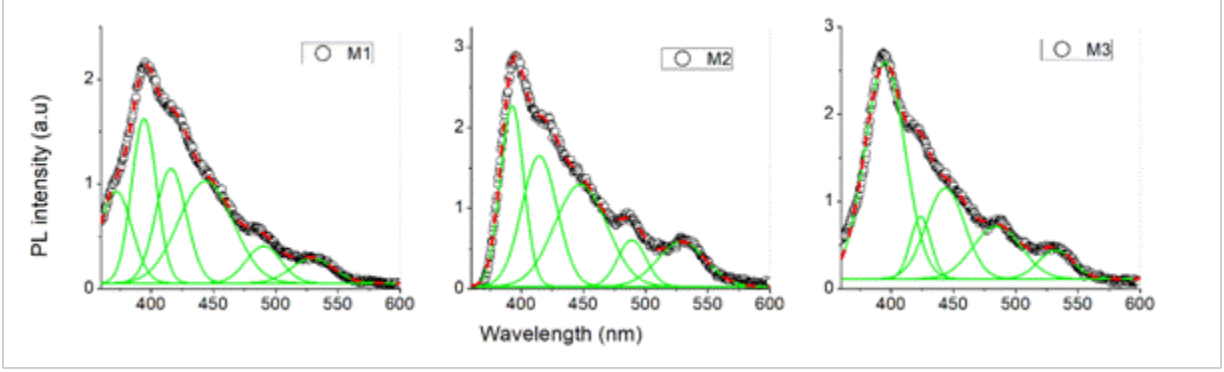

Fig. 4-6 PL spectra of the prepared samples decomposed using the *Gaussian* profile. The symbols are data points, yellow (solid) lines and red (dashed) line are fitting parameters.

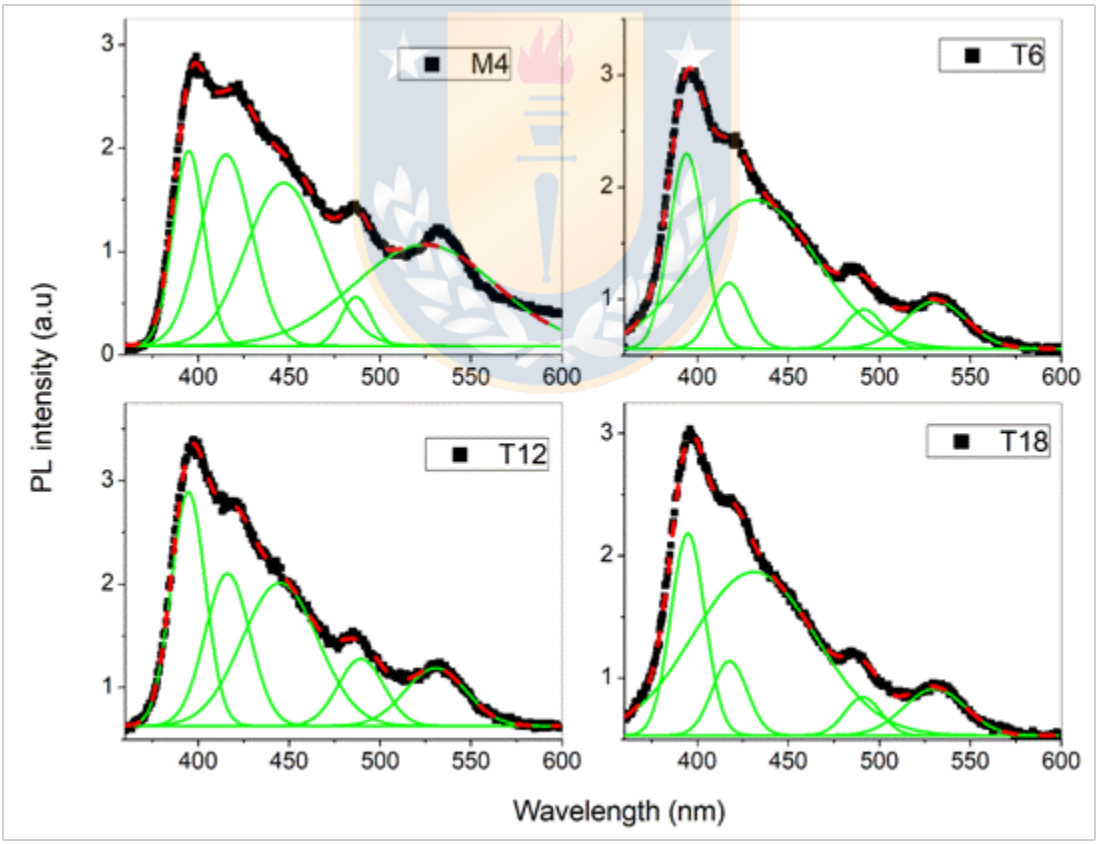

Fig. 4-7 PL spectra of the prepared samples decomposed using the *Gaussian* profile. The symbols are data points, yellow (solid) lines and red (dashed) line are fitting parameters.

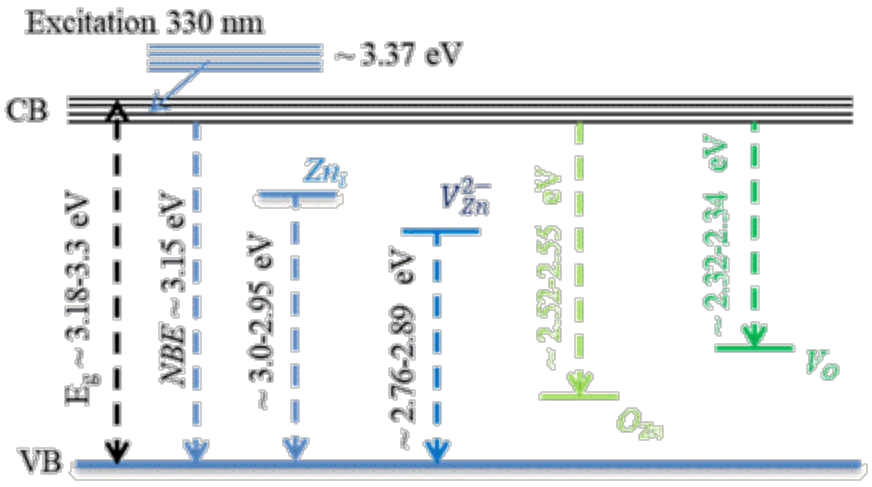

Fig. 4-8 The schematic band diagram of ZnO nanoparticles emission in PL spectroscopy.

The SX emission was quenched in the remaining samples due to the formation of nanostructures with less surface dangling bonds and trapping sites which was supported by the increase in crystallite size and change in morphology from the prism to rod in shape [131,132]. The variation of the peak maximum of the various bands with the synthesis condition is shown in Fig. 4-9a. For further analysis of the optical emission behavior of the samples, the ratio of the intensity variation of the NBE (I_{NBE}) and defects emission (I_{def}) (for this *Zn_i and V_O related emission peaks were considered*) was obtained and shown in Fig. 4-9b. The band edge related emission in ZnO nanostructures is a function of the crystallinity and the NBE is higher for samples with higher crystallinity. All the samples followed this trend and the observed variation in the intensity of the NBE emission was attributed to the variation in the crystallite size. Further, from the Fig. 4-9b it was evident that the sample M3 exhibited the enhanced NBE emission when compared to the defects related emission among the all other samples and this was due to high crystallite size and low microstrain [133,134]. By varying the refluxing time, the samples prepared with equal concentration of precursors (T6, T12 and T18), as mentioned previously the rod morphology was

gradually deteriorated, which means that the particles were formed with large surface area signified the presence of more surface defects such as oxygen vacancies and oxygen interstitials. Thus, increase in the refluxion time led to the formation of more defects and exhibited decreased NBE emission when compared to the sample M3.

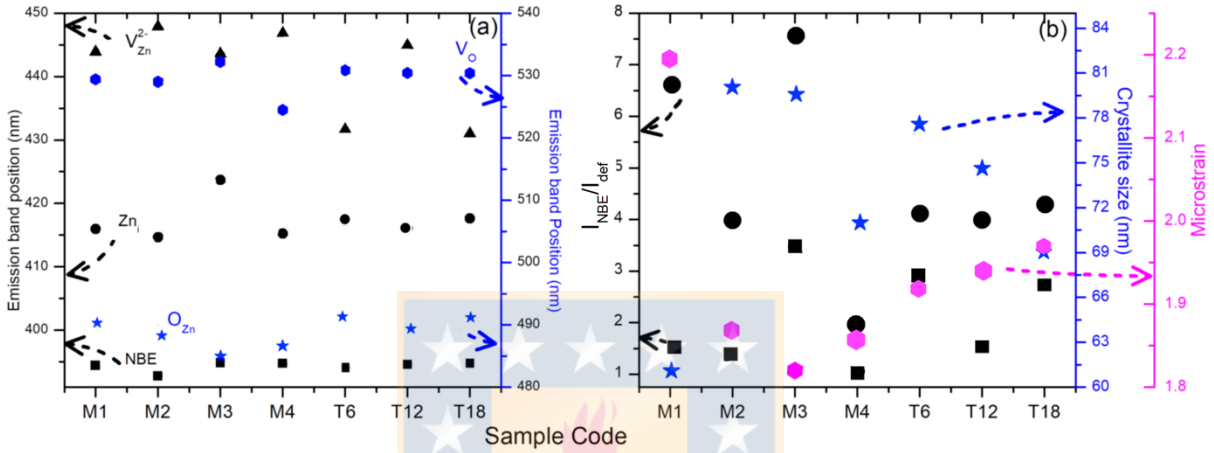

Fig. 4-9 Variation of **(a)** the peak position of the various emission bands and **(b)** I_{NBE}/I_{def} along with the crystallite size and microstrain of the prepared samples. For the calculation of the I_{NBE}/I_{def}, the emission related to defects such as Zn_i (solid square/black) and V_o (solid circle/black) are considered.

4.1.5. Raman spectra

The Raman spectroscopy is a prevalent and highly sensitive technique which can provide information about nature of material, as well as specific aspects of lattice dynamics, likewise secondary phase formation, structural defects and phonon life times. The *wurtzite* phase ZnO nanorods, as a wide band gap semiconductor, contains four atoms at primitive unit cell with two molecules in *Bravais* unit cell. The Raman spectra of the prepared ZnO nanostructures were recorded using the 532 *nm* excitation and shown in Fig. 4-10. The Raman spectra were

decomposed by using *Gaussian* profile and the obtained parameters were tabulated (Table 4-5). The observed Raman peaks located at ~102 and ~441 cm^{-1} were assigned to $E_{2,Low}$ and $E_{2,High}$ modes, respectively. The bands appearing at ~332, ~384 and ~418 cm^{-1} were recognized as $E_{2,High} - E_{2,Low}$, $A_1(TO)$ and $E_1(TO)$ modes, respectively. The modes related to the first order longitudinal optical phonons appeared as a broad band [135] in the range 510-600 cm^{-1}. The broad band appeared in the *LO* phonon range consisted of two phonon modes at ~570 and ~586 cm^{-1} were attributed to the $A_1(LO)$ and $E_1(LO)$ modes. The $A_1(LO)$ was not well resolved in the samples with well-defined morphology except in the sample M1.

These LO phonon modes usually present as a single mode (*quasi-1LO* mode) due to the influence of the free carriers presented in the system. The asymmetric broadening of this *quasi-1LO* mode is due to the *Fano* type interaction between discrete scattering phonon and continuum-states created by the impurities in ZnO nanostructures [136]. The higher order modes related to the various second order processes were identified [137].

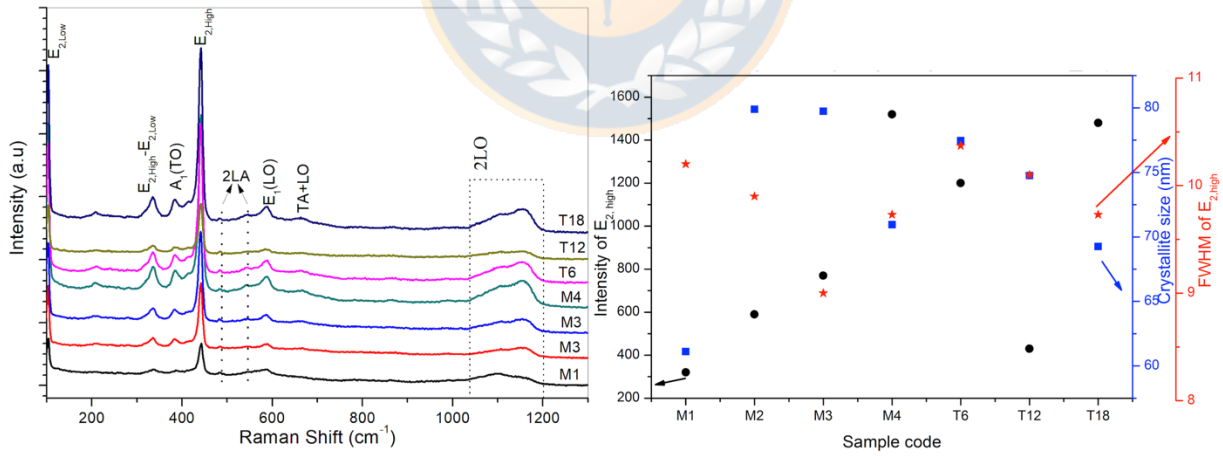

Fig. 4-10 (a) Raman spectra of the prepared ZnO nanostructures **(b)** Variation of FWHM, intensity of $E_{2,High}$ with crystallite size.

Table 4-5 The peak position of the various Raman bands of the prepared ZnO nanostructures.

M1	M2	M3	M4	T6	T12	T18	Ref.	Process
103.2	103.0	102.4	103.1	102.5	102.9	102.7	101 [138]	E_2^{low}
334.8	328.0	329.0	332.2	334.3	334.2	334.1	334 [116],[138]	E_2^{high} -E_2^{Low}
387.2	384.3	384.05	385.3	384.01	383.9	383.3	381 [139],[140]	A_1(TO)
419.5	417.6	-	417.5	421.3	417.4	418.5	420 [116]	E_1(TO)
441.8	441.3	440.6	441.6	441.08	441.2	441.1	438 [140,141]	E_2^{high}
483.1	484.1	482.9	483.3	-	483.9	483.4	483 [138],[140,141]	2LA
543.6	544.1	547.1	554.1	553.5	557.3	546.0	540 [140], 551 [116]	2LA; B_2^{low}
569.2	573.3	-	-	-	-	-	569 [140]	A_1(LO)
587.4	587.5	586.0	586.9	586.7	587.0	585.8	586 [140]	E_1(LO)
-	666.3	660.8	665.6	660.6	663.5	662.9	666 [140,141]	TA+LO
781.81	-	-	-	-	-	-	782 [142]	LA+TO
-	987.4	966.2	-	-	-	-	989 [142]	2TO
1047.4	1073.4	-	1077.1	-	-	-	1072 [140,141]	TO+LO
1102.1	1118.3	1113.6	1122.1	1107.9	1107.7	1111.2	1122 [116]	TO+LO
1161.3	1160.2	1160.1	1160.8	1158.0	1159.5	1159.6	1158 [5]	$2A_1$(LO), $2E_1$(LO); 2LO

In general, the signature of $E_{2,High}$ phonon has been used to investigate the variations in crystallite size and defects chemistry in ZnO nanostructures [143]. Yoshikawa et al. [144] reported that the full width at half maximum (FWHM) of $E_{2,High}$ mode exhibited an inverse relation with crystallite size. In the present study, the samples M1, M2 and M3 followed the similar trend. In contrast, the samples prepared by varying the refluxing time (M4, T6, T12 and T18) exhibited a direct relation with the crystallite size. Thus, in spite of the effect of the crystallite size, the other parameters like dislocation and defects concentration has an influence on the signature of the $E_{2,High}$

mode in the samples prepared by varying the refluxing time [143,145]. The intensity of the $E_{2,High}$ mode was high in the case of highly crystalline samples. The variation of the intensity of the $E_{2,High}$ with crystallite size is shown in the Fig. 4-10b. From the Fig. 4-10b it is evident that $E_{2,High}$ was more intense in the case of the samples M4 and T18 but the crystallite size was low when compared with the sample M3. This discrepancy was due to the polydisperse nature of the nanorods morphology when compared with the monodisperse nature of the M3 sample. Further we obtained the phonon life times of the observed Raman modes. The phonon life time is an important in deciding the functionality of semiconductors in static and dynamic applications. It has been a center of attention of materials researchers in the prediction of thermal transport properties for opto-electronics applications [135]. The parameters that led to shortening life time are imperfections crystals [146] and crystallinity size [147]. The crystal with imperfections can make perturbation in symmetry of the crystal and thus reduce the phonon life time. The phonon life time can be interpreted from the Raman spectral modes by using the energy-time uncertainty relation:

$$\frac{1}{\tau} = \frac{\Delta E}{\hbar} = 2\pi c\,\Gamma$$

where, ΔE is uncertainty in the energy of the phonon, $\hbar$ is the Planck constant, and Γ is the full width at half maximum (FWHM) of Raman band under consideration. The analysis of $E_{2,High}$ and $E_1(LO)$ revealed the correlation between phonon lifetime and crystallinity size [147]. It was evident that increase in value of crystallinity led to decrease in the phonon lifetime. The obtained values are tabulated on Table 4-6 for comparison.

Table 4-6 Phonon life time for ZnO nanorods.

Phonon mode/Sample code	τ (ps)						
	M1	**M2**	**M3**	**M4**	**T6**	**T12**	**T18**
$E_{2,High}$	0.523	0.528	0.512	0.544	0.511	0.525	0.541
E_1(LO)	0.233	0.352	0.273	0.287	0.280	0.277	0.220

4.1.6. Photocatalysis studies

The photocatalytic activity of the prepared ZnO nanostructures with different morphology (prism, rod and bipods) for the degradation of MB dye was analyzed (Fig. 4-11). The prominent absorption peak at 665 *nm* corresponds to the MB dye was considered for monitoring the photocatalytic activity [148]. The removal efficiency of catalyst from the photocatalytic degradation studies was calculated using the formula [148,149]:

$$\eta = \frac{(C_0 - C_t)}{C_0} \times 100$$

where 'C_0' is the initial concentration, 'C_t' is the concentration at a specific time (t) after visible light irradiation, and 'η' is the efficiency of photocatalytic degradation.

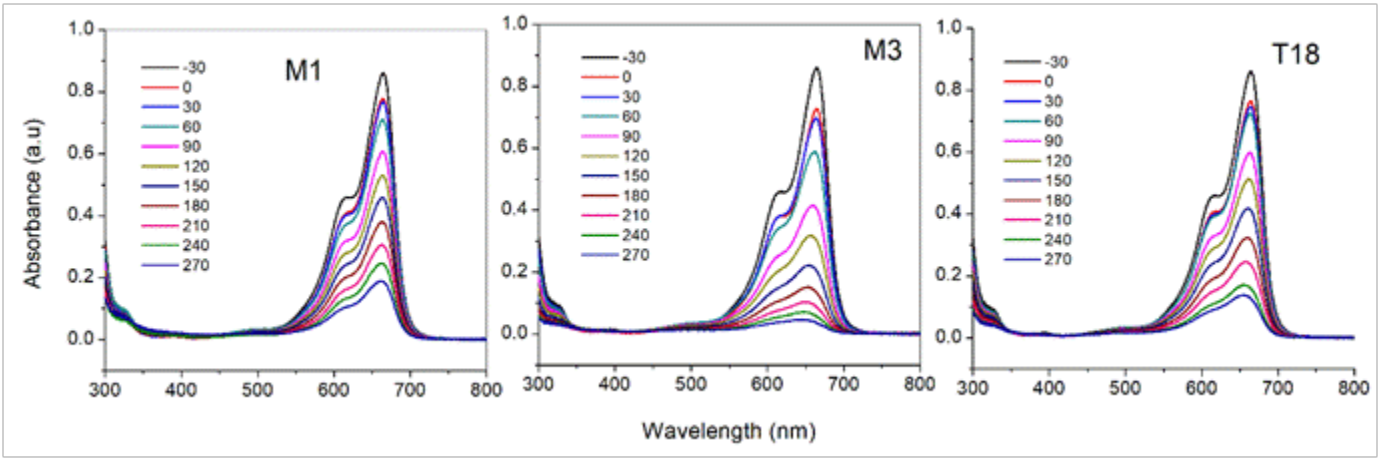

Fig. 4-11 The optical absorption spectra of the aliquots in the photocatalysis studies.

The three samples under consideration were exhibited a very good efficiency in degrading the dye through photocatalysis (Fig. 4-12a). The rate constant values were obtained from the linear fit of the plot of "-ln(C_t/C_0) *vs t*" (Fig. 4-12a). From the Fig. 4-12b it is clearly evident that the sample M3 which has high crystallinity and less defects related emission has superior degradation activity of the dye.

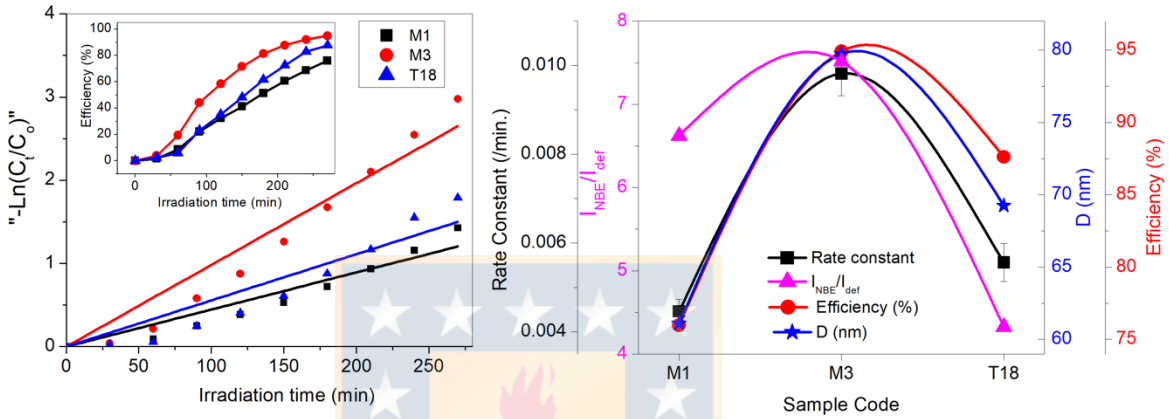

Fig. 4-12 Photocatalytic performance of the prepared ZnO nanostructures with different morphology. The plots of **(a)** first order kinetics of the various photocatalysts and **(b)** variation of rate constant along with efficiency, crystallite size and I_{NBE}/I_{def} of different ZnO nanostructures samples (PL intensity related to oxygen defects was considered for calculating the ratio).

Table 4-7 The rate constant, photocatalysis efficiency, crystallite size and I_{NBE}/I_{def} of ZnO nanostructures.

Samples	η **%**	**rate constant** min^{-1}	**crystallite size nm**	I_{NBE}/I_{def}
M1	76	4.1×10^{-3}	61.11	6.6
M3	94	9.6×10^{-3}	79.74	7.4
T18	87	5.5×10^{-3}	69.26	4.2

I observed that the optimal level of 0.05 M of HMTA with 3 h refluxing reaction time, let to the improvement of crystallinity and favored the formation of rod like nanostructures. For instance, the sample M3 exhibited monodisperse hexagonal rods like morphology with high crystallite size, low microstrain, and high band gap values. these ideal parameters leas to the observation of high near band gap emission and less intense defects related emission which subsequently favored the enhanced photocatalytic activity when comper with the other prepared ZnO samples. furthermore, I have selected sample M3 as the core in order to preparation ZnO@CeO_2 core shell samples.

4.2. CeO_2 nanostructure

4.2.1. Structural analysis

The XRD patterns of the prepared samples are shown in Fig. 4-13. For all the samples, the peaks are well indexed for cubic fluorite structured CeO_2 (JCPDS# 655923). The absence of any additional peaks confirms the successful formation of the well crystalline CeO_2 which is free of any secondary phases. In order to analyze the effect of the synthesis parameters such as different power and different time of microwave irradiation, the XRD data of the samples were fitted with a Lorentzian profile to get the exact peak positions and full width at half maximum (FWHM). The obtained parameters were used for the calculations of lattice parameters and for Williamson-Hall (W-H) analysis. The structural parameters of CeO_2 structures are given in Table 4-8.

Table 4-8 For comparison of structural parameters of CeO_2 obtained from XRD by considering the (111) peak. *- dominant morphology in the samples.

Sample	**2θ (deg.)**	**FWHM**	**d (*nm*)**	a (*nm*)	**V (*nm*^{3})**	**Morphology**
L4	28.53	1.604	0.313	0.5413	0.15862	Spheroidal*+Nanorod
L8	28.49	1.439	0.313	0.5420	0.15919	Spheroidal*
L12	28.53	1.469	0.312	0.5413	0.15857	Nanocube*
M4	28.50	1.979	0.313	0.5418	0.15906	Spherical*
M8	28.54	1.548	0.312	0.5410	0.15833	Spheroidal+ Nanorod*
M12	28.52	1.902	0.313	0.5414	0.15872	Spheroidal+ Nanorod*
H4	28.54	1.008	0.312	0.5410	0.15834	Nanosphere*
H8	28.51	2.129	0.313	0.5416	0.15884	Nanorod*
H12	28.49	1.609	0.313	0.5419	0.15917	Nanorod*

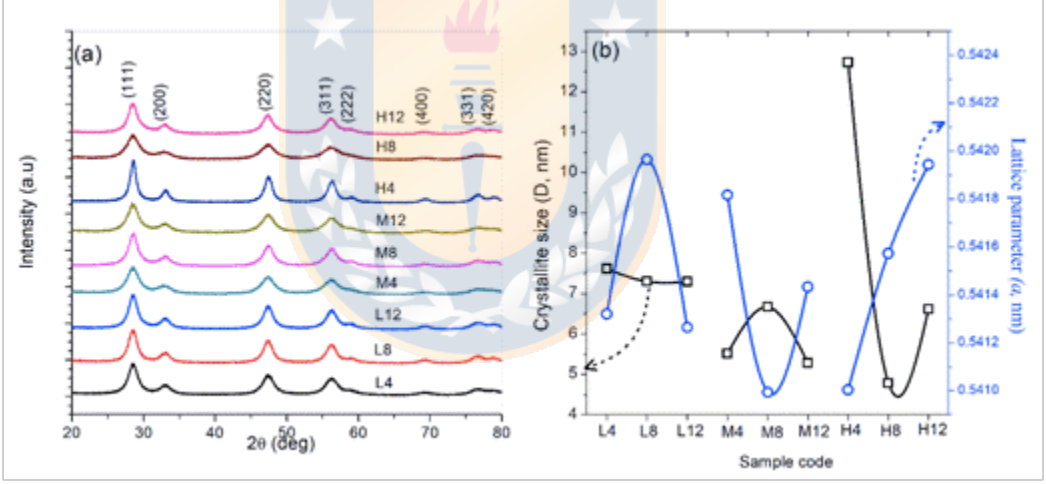

Fig. 4-13 (a) X-ray diffractograms of the as-synthesized pure ceria nanostructures. **(b)** Variation of lattice parameter and crystallite size of the prepared samples.

The morphological changes observed in the samples with the variation in the synthesis conditions and it is discussed using the morphological studies. The variation of the calculated lattice parameter along with the crystallite size is shown in Fig. 4-13b. It is evident that the

crystallite size played a main role in the observed lattice deformation or lattice contraction in ceria nanostructures. In connection to this observation, the work reported by Chen et al. is noteworthy [87]. They observed a complex variation of lattice parameter with crystallite size. They reported that the lattice contraction is dominant when the crystallite size decreases from 500 to 15 *nm*, and expansion is dominant when the crystallite size decreases down from 15 to 2 *nm*. In other words, the increase of crystallite size (up to 15 *nm*) exhibited contraction of lattice parameter and a further increase in crystallite size (above 15 *nm*) the lattice parameter exhibited expansion. From the Fig. 4-13b, it is evident that the crystallite size and lattice parameter exhibited an inverse relation. Thus the observed variations in the lattice parameter is attributed to the variation of the crystallite size of the prepared samples [87]. Perhaps, the incoherence exhibited by the samples L12 and H12 can be attributed to the morphological changes when compared with the other samples of the similar set, which is discussed in the next section.

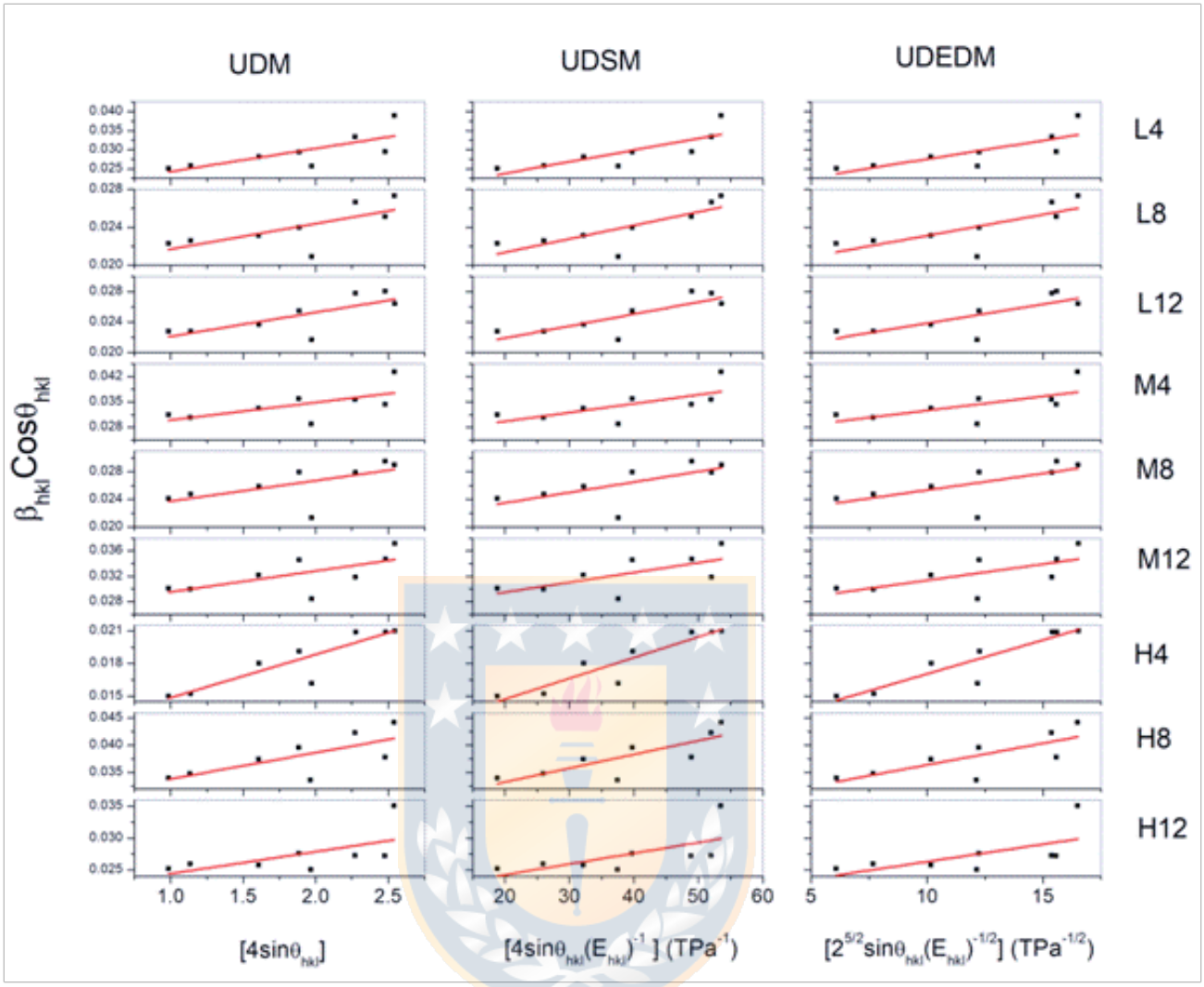

Fig. 4-14 W-H analysis plots obtained from the XRD data using the UD, UDS, UDED models.

In the UD model, the microstrain is considered as uniform in all crystallographic directions and the slope from the plot of the $\beta_{hkl}\cos\theta_{hkl}$ *vs* $4\sin\theta_{hkl}$ is used for obtaining the microstrain value for all the samples. The W-H plots based on the UD, UDS and UDED models are used for further analysis (Fig. 4-14) and the intercept of each plot is used for obtaining the crystallite size of each sample. The variation of the microstrain, stress, deformation energy density and crystallite size for different synthesis conditions is shown in Fig. 4-15. The samples prepared with low power (L) and medium power (M) exhibited relaxation in microstrain with an increase in the reaction

time, respectively. The crystallite size variation exhibited a direct relation with the microstrain in the samples prepared with low power (L4, L8 and L12). Whereas the crystallite size variation shown an inverse relation with the microstrain in the samples prepared with medium (M) and high power (H), respectively. The sample prepared with high power (H4) has high crystallite size among the all other samples. We observed that the samples prepared with the low power possess merely equal crystallite size. The variation in crystallite size is very high in the samples prepared with high power. Noted that there is no particular trend in the variation of crystallite size with respect to the time duration of synthesis for a particular power of microwave irradiation.

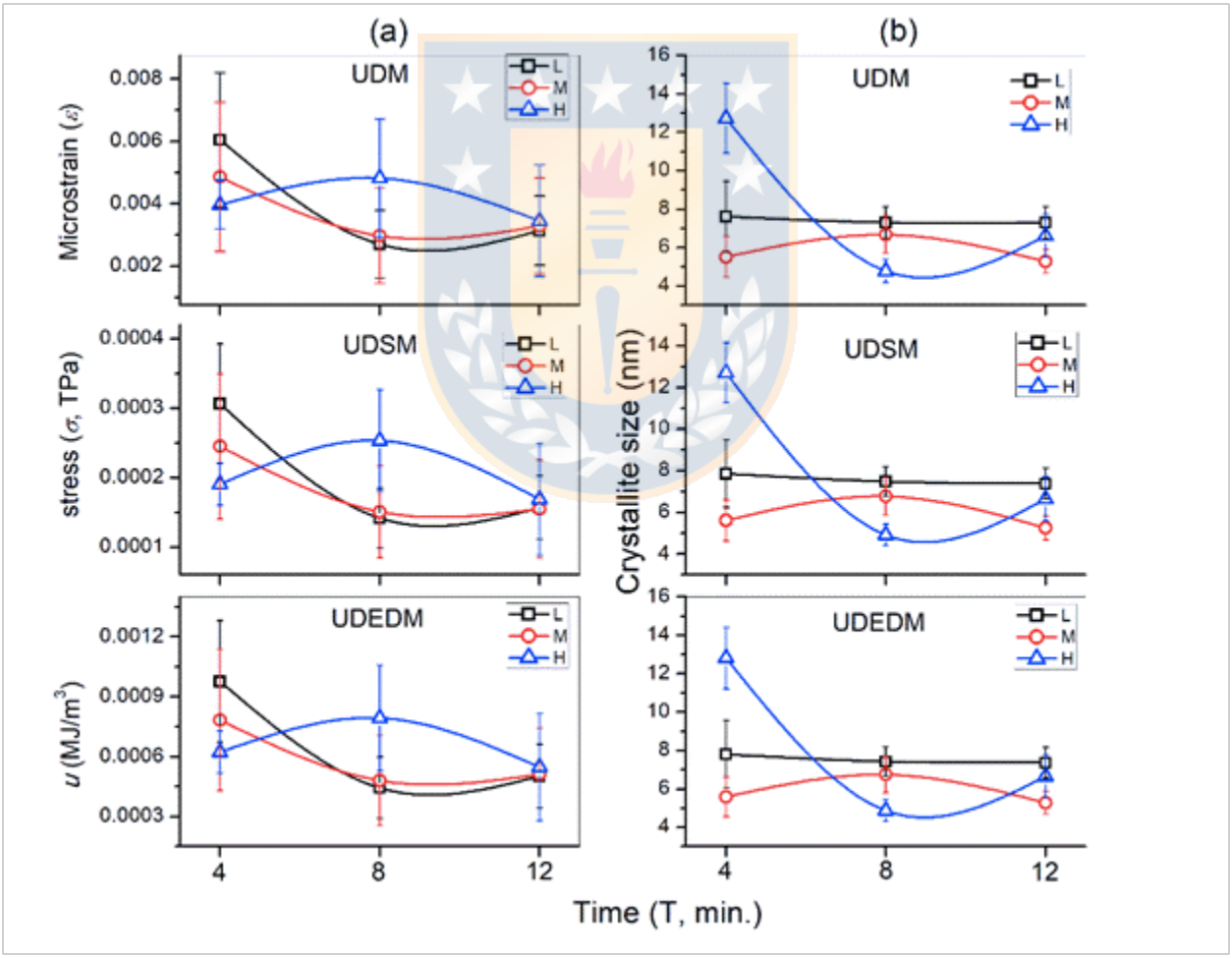

Fig. 4-15 The variation of **(a)** microstrain, stress and deformation energy density; **(b)** crystallite size with the preparation time for different powers based on the UDM, UDSM and UDEDM.

4.2.2. Morphological analysis

TEM micrographs of all the prepared samples are depicted in Fig. 4-16. The sample (L4) which was prepared with low power and for low time duration exhibited a random morphology (spheres and rods) and the size of the spherical particles is merely in the range of the crystallite size calculated from W-H analysis. From the images, it is depicted that the samples prepared with a fixed time (of 4 min.) and for different powers (L4, M4 and H4) exhibited an increase in monodispersity and uniformity in the nature of the size and shape of the nanostructures. Remarked that the sample synthesized with high power (H) irradiation for lower time duration resulted in the monodisperse spherical morphology. It is evident from the figure that the samples prepared with a fixed power (L) for different time durations (L4, L8 and L12) also exhibited morphological changes from sphere to cube-like nanostructures. The size of the side facet of the ceria nanocube structures of L12 sample is merely in the range of the crystallite size calculated from the XRD.

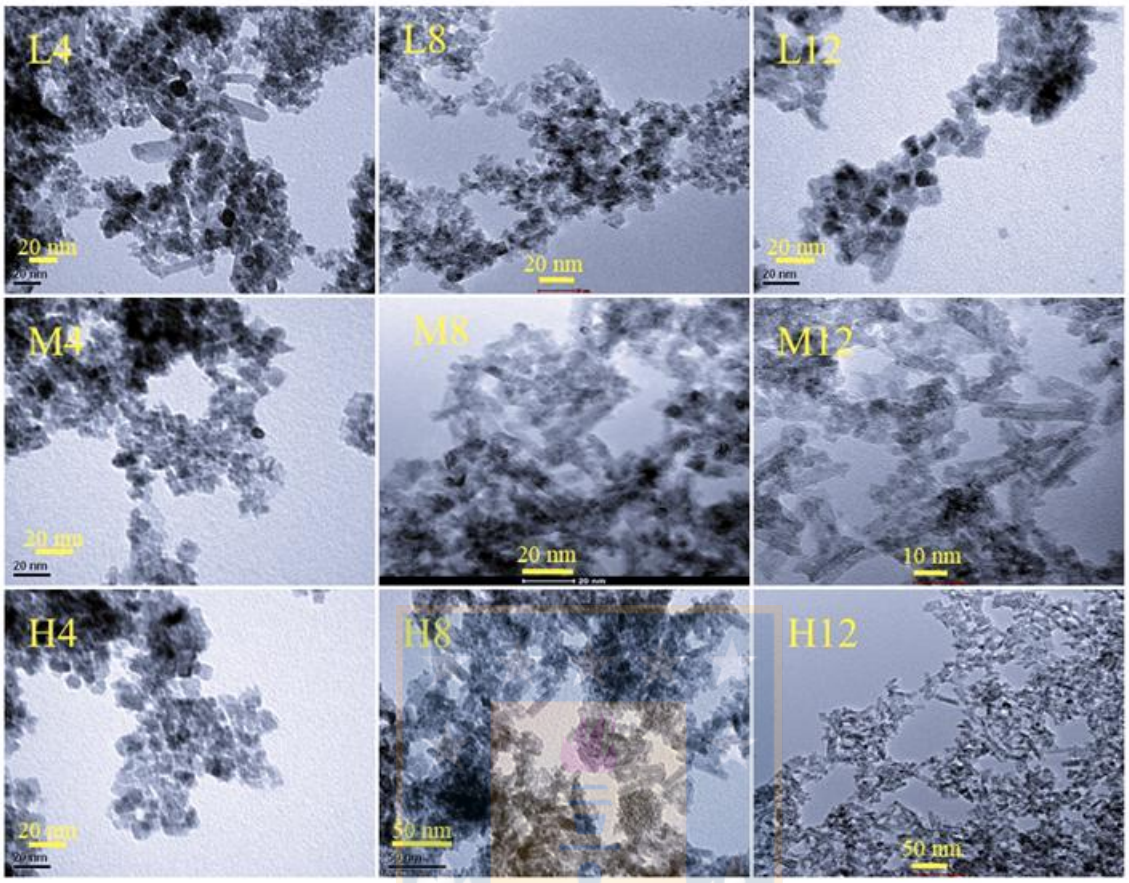

Fig. 4-16 TEM images of the ceria nanostructures prepared by varying the power (P) and time duration (T) of preparation.

Thus, the variation of the time period of synthesis with fixed power (low power, L) also led to an increase in monodispersity and uniformity in the nature of the size and shape of the nanostructures. By comparing the morphology of the samples prepared with high power (H4, H8 and H12) it is evident that the increase of time period of synthesis led to the change of the morphology from the spherical to uniform rods like nanostructures. The sample prepared at high power and time resulted in ceria nanorods with dimensions in the range of 6−8 *nm* and 34−36 *nm* as diameter and length, respectively. The possible reaction mechanism for the synthesis of nanoceria is:

$$Ce^{2+} + OH^- \rightarrow CeO_2(NP) + H_2O$$

The microwave irradiation led to the rapid hydrolysis, the $Ce(OH)_2$ core nuclei gets aggregated and led to the formation of the nanostructures with random morphology. The microwave irradiation in the subsequent reaction intervals led to the deterioration and re-agglomeration of the smaller nanostructures. Thus, in the subsequent reaction intervals, the possible reaction mechanism for the formation of rods is:

$$CeO_2(OH)_4 + OH^- \rightarrow CeO_2(NR) + H_2O + OH^-$$

Sakthivel et al. reported about the shape evolutions in ceria nanostructures prepared by hydrothermal method and perceived that the dissolution and recrystallization of certain facets of ceria at elevated hydrothermal temperature resulted in the formation of nanorods and nanocubes [84]. Lai et al. observed, due to dissolution-recrystallization by tuning the hydrothermal treatment time, morphological evolution between the nano-octahedron and nanorod of ceria [150]. The TEM image of the sample L4, which exhibited that the majority nanostructures of spherical morphology and with a nominal quantity of nanorods, supports our assumption about the morphology changes. By considering the samples prepared with high power (H4, H8 and H12), the morphology is gradually transformed into nanorods (from nanospheres) with increasing the time of microwave irradiation in the synthesis sequence. The sample H8 exhibited both rods and spherical particles which depicts the transformation of the spheres (H4) to nanorods (H12) clearly supports the influence of the microwave irradiation in the subsequent reaction intervals for morphological transformations. By considering the samples prepared with fixed time (T=12) for different powers (L12, M12 and H12) also depict the morphological transformations from nanocubes (L12) to nanorods (H12) which strongly suggest the particle growth by the agglomeration of the smaller nanostructures during the successive intervals of the reaction sequence. Overall it is interesting to

notice that the time interval (for every 2 min a cooling time of 1min), power (P) and total reaction time (T) during the synthesis played a major role in the morphological variations of the prepared nanostructures [150].

4.2.3. Optical absorption studies

The optical absorption spectra of all the samples are shown in Fig. 4-17a. As discussed earlier, previous reports suggest that the band gap of ceria nanostructures greatly influenced by the size and morphology. The optical absorption data are used to calculate the band gap of the nanostructures. The band gap (Eg) and the absorption coefficient (α) of the nanostructures are connected by the relation$\alpha hv = C(hv - E_g)^n$. Here, "C" is the constant, "n=1/2" for a direct allowed transition (direct band gap) and 'hv' is the photon energy [26]. The optical absorption coefficient (α) can be obtained from the optical absorbance (A) by using the relation,

$$\alpha = \frac{2.303 \times 10^3 \, A\rho}{lc}$$

where ρ is the the real density of the ceria (7.28 g/cm^3),'c' is the concentration of the suspension and 'l' is the path length of cuvette used for optical absorption measurements [151]. The band gap energy values are obtained by extrapolating the linear portion from the plots of $(\alpha hv)^2$ vs hv. The obtained band gap values from the *Tauc* plots are merely equal or greater than that of the bulk ceria powders (3.15 eV), which is mainly ensued from the size effect in ceria nanostructures. In general, CeO_2 nanostructures consists of Ce^{3+} ions on the surface and these ions are responsible for the formation of oxygen vacancies at the surface level. Usually, the decrease of particle size is associated with the increase of Ce^{3+} ions on the surface of the nanostructures. The morphological changes observed with varying the synthesis conditions may also effect the valence transition $Ce^{4+} \rightarrow Ce^{3+}$, which in turn influence the band gap of the ceria [92,152]. The variation of the band gap with the crystallite size for different synthesis conditions is shown in Fig. 4-17b. The variation

of crystallite size vs microstrain and the variation of band gap vs crystallite size merely followed the similar trends.

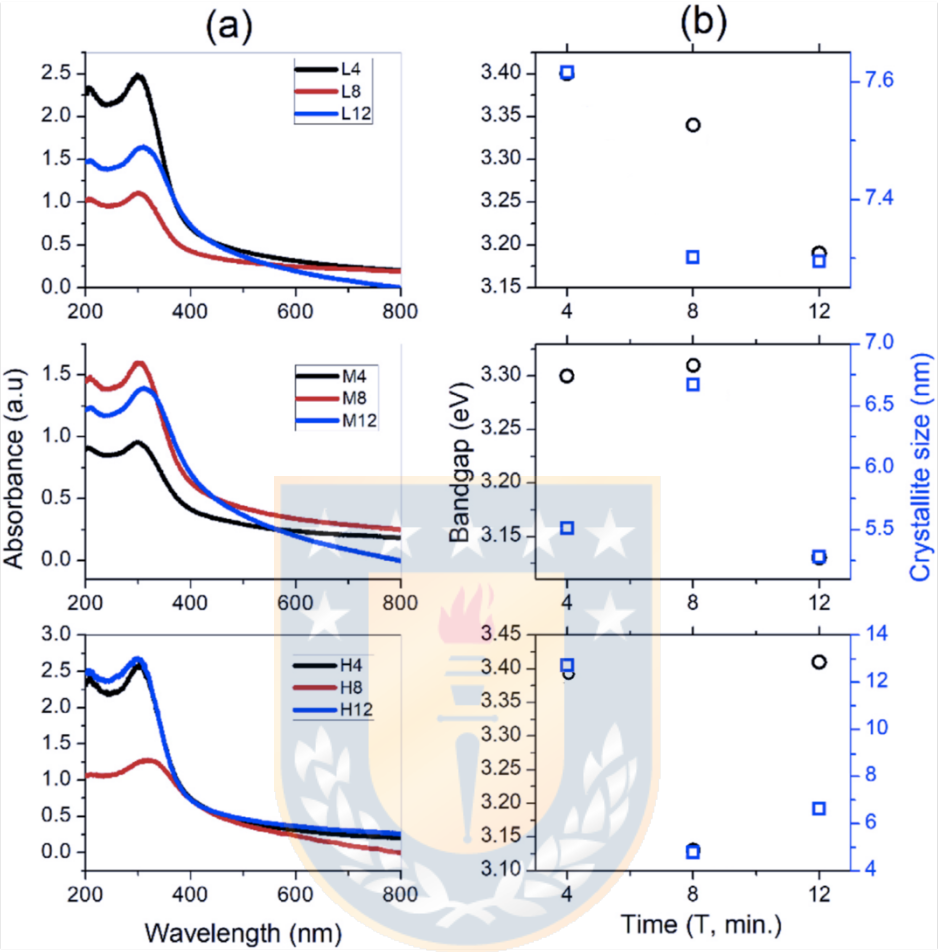

Fig. 4-17 Variation of (a) Optical absorption edge and (b) variation of the band gap and crystallite size with the preparation time. The plots are categorized based on the power of microwave irradiation used for preparation.

We observed that the direct band gap decreases with the crystallite size of the ceria nanostructures. In general, in case of CeO_2 nanostructures, the redshift of the band gap is due to shape effects and the increase of Ce^{3+} concentration which in turn increases the oxygen related defects and leads to the formation of defects related band within the band gap of the material [152,153]. Thus, it is clearly evident that the decrease in crystallite size led to a decrease in the band gap of the

nanostructures [154]. Perhaps, the observed variation in this trend for the samples L12, M8 is attributed to the changes in the microstrain and morphology [87,153].

4.2.4. Photoluminescence (PL) studies

The room temperature PL emission spectra of the prepared samples are shown in Fig. 4-18a. All the samples exhibited a strong emission band in the UV region related to the band edge emission and a weak broad emission in the visible region due to various structural defects present in the ceria nanostructures. To get insight into the influence of the synthesis conditions on the emission of the ceria nanostructures, emission data in the range of interest was fitted using the Lorentzian profile (Fig. 4-19) and the obtained parameters are tabulated on Table 4-9. For instance, the fitted PL data of the sample L4 exhibited five emission bands centered on 399.3 (~3.1), 421.6 (~2.9), 449.4 (~2.8), 486.2 (~2.6) and 533.4 (~2.3) *nm* (*eV*), respectively. From the fitted data, it was observed that all the samples exhibited a similar trend of emission with a noticeable variation in the intensities related to various peaks. The emission band centered on ~ 399 *nm* corresponds to the band gap related emission of the ceria nanostructures which is originated from the recombination of electrons from the localized Ce-4*f* state to holes in the O-2*p* valence band [82,155]. The emission band centered on ~449 *nm* can be attributed to the Ce^{3+} fluorescent center present over the surface of the nanostructures.

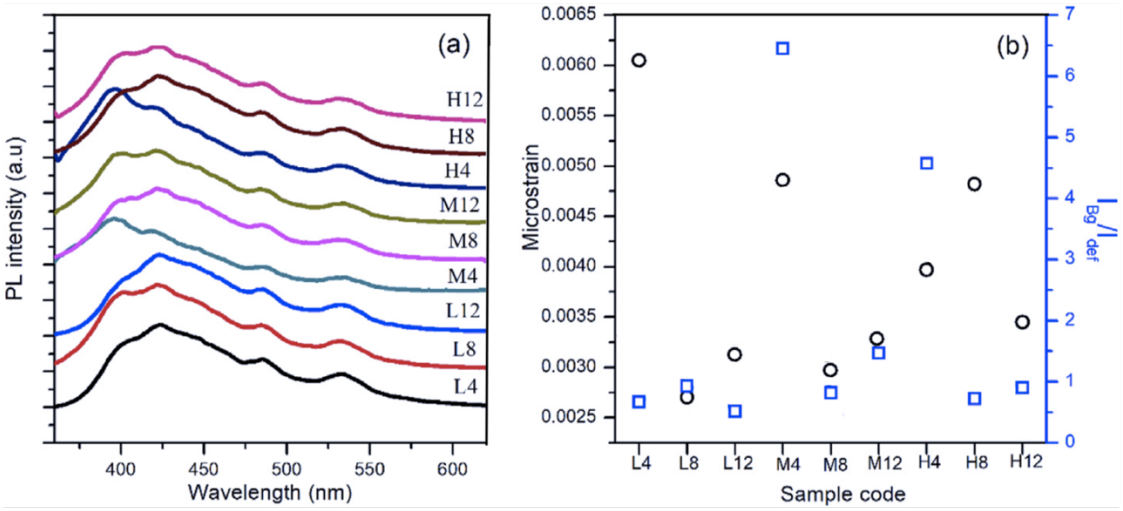

Fig. 4-18 (a) PL spectra of the ceria nanostructures prepared under different conditions. **(b)** Variation of the microstrain and the ratio of the intensity of band gap related emission (I_{Bg}) and defects related emission (I_{def}).

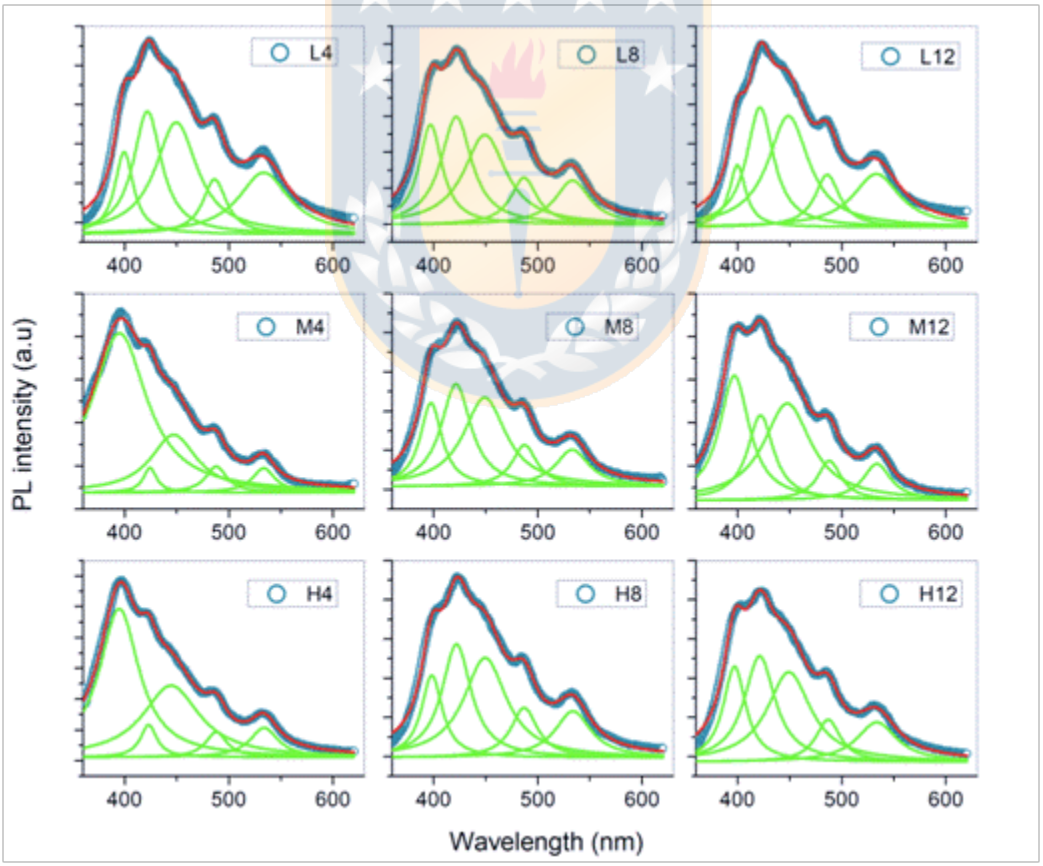

Fig. 4-19 Emission spectra decomposed by considering the *Loerntzian* profile. Circles are data points while solid lines are numerical fits using *Lorentzian* profile.

Table 4-9 The parameters like emission peak center, FWHM and intensity of the decomposed peaks from the PL data.

Peak center	FWHM	Int.	Peak center	FWHM	Int.	Peak center	FWHM	Int.
L4			L8			L12		
399.3	21.520	1.314	396.9	27.108	1.745	399.7	19.277	0.991
421.6	32.955	1.962	421.5	35.987	1.884	421.4	31.501	1.915
449.4	48.873	1.787	449.0	49.400	1.566	448.7	47.702	1.776
486.2	27.831	0.876	486.7	30.720	0.820	486.0	29.076	0.836
533.4	58.984	0.985	533.3	40.645	0.771	533.2	55.017	0.850
M4			M8			M12		
394.9	63.303	2.316	397.3	25.554	1.335	396.8	34.889	1.812
424.1	15.693	0.359	421.3	34.847	1.636	422.0	30.514	1.236
447.0	54.050	0.839	448.9	49.770	1.422	447.7	55.623	1.407
487.8	24.406	0.380	487.1	28.809	0.665	488.0	27.838	0.575
533.4	26.491	0.353	533.1	39.182	0.589	533.7	32.779	0.529
H4			H8			H12		
394.6	46.086	3.023	398.1	24.576	1.316	396.9	26.459	1.525
422.9	19.131	0.662	421.8	34.191	1.813	421.1	36.075	1.692
444.5	66.270	1.461	449.3	50.125	1.596	449.2	51.083	1.433
487.9	24.626	0.519	486.8	30.976	0.800	486.9	28.455	0.678
533.8	33.025	0.601	533.7	41.983	0.744	533.7	46.590	0.634

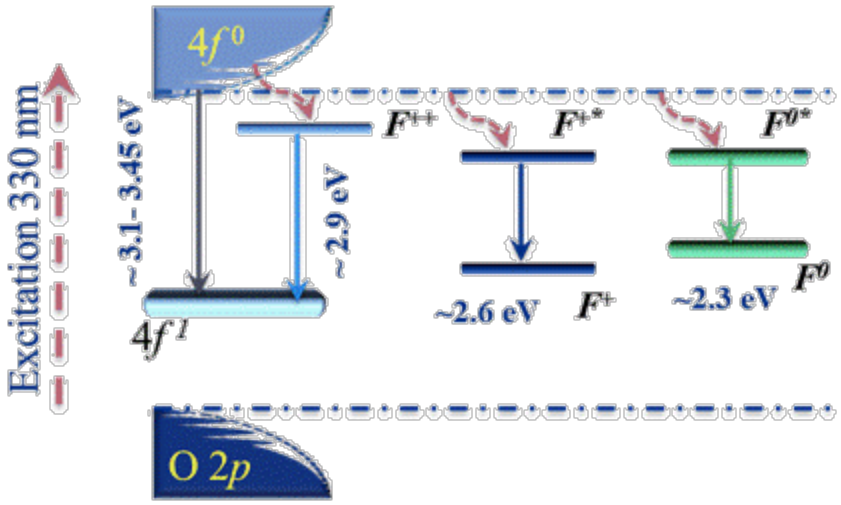

Fig. 4-20 Schematic representation of *F-centers* related to oxygen vacancies which are responsible for the visible range emission in the ceria nanostructures.

This emission band associated with the transition from the *4d* to the *4f* of the Ce^{3+} in the ceria nanostructures [156]. The other three bands in the visible region are due to the presence of various oxygen vacancies related defect levels which lie within the band gap of ceria. The presence of Ce^{3+} led to the splitting of 4f band into 4*f* full ($4f^1$) and 4*f* empty ($4f^0$) bands [92]. The nanostructures of ceria are known to exhibit three types of defect centers by capturing two, one or no electrons which are denoted as F^0, F^+ or F^{++} centers, respectively. These defects related *F*-centers lie below the $4f^0$ state within the band gap of the ceria. The recombination of excited electrons due to these *F*-centers results in the visible range emission in ceria [92]. The possible radiative transitions related to the PL emission peaks are depicted in the proposed energy level diagram are display in Fig. 4-20. Thus, the observed different emission bands in the visible region in our samples signify the presence of various oxygen related defects in the nanostructures. To better understand the influence of the synthesis parameters on the emission properties the ratio of the intensity of band gap related emission (I_{Bg}) and defects related emission (I_{def}) was calculated.

For this, the peaks centered on 399 *nm* (I_{Bg}) and 421 *nm* (I_{def}) were considered. The variation of this ratio along with the microstrain of the prepared samples was plotted and shown in Fig. 4-18b. In ceria type nanostructures, the increase of microstrain usually led to decrease of crystallite size and band gap, respectively [86,87]. The relaxation of microstrain signifies the presence of more defects in the structure and it favors the enhancement of defects related emission in the visible region [79,89]. From the Fig. 4-18b, it is evident that the samples prepared with medium power followed this assumption and signifies the influence of microstrain on the defects related emission. The little discrepancies observed in the case of the samples prepared with the low and high power due to the morphological changes as discussed in earlier sections.

4.2.5. Photocatalytic activity studies

The photo-degradation activities of the prepared ceria nanostructures with different morphology were determined by monitoring the degradation of MB dye. For the photocatalytic activity studies the samples prepared with Low power (L4, L8 and L12), and the samples prepared with different power (L12, M12 and H12) for a time of t=12 min. were considered. The characteristic absorption band of MB dye was monitored by using optical absorption spectroscopy for the analysis of the photocatalytic activity. The Fig. 4-21 are shown absorption spectra of the aliquots were recorded to monitor the time-dependent photodegradation of MB dye.

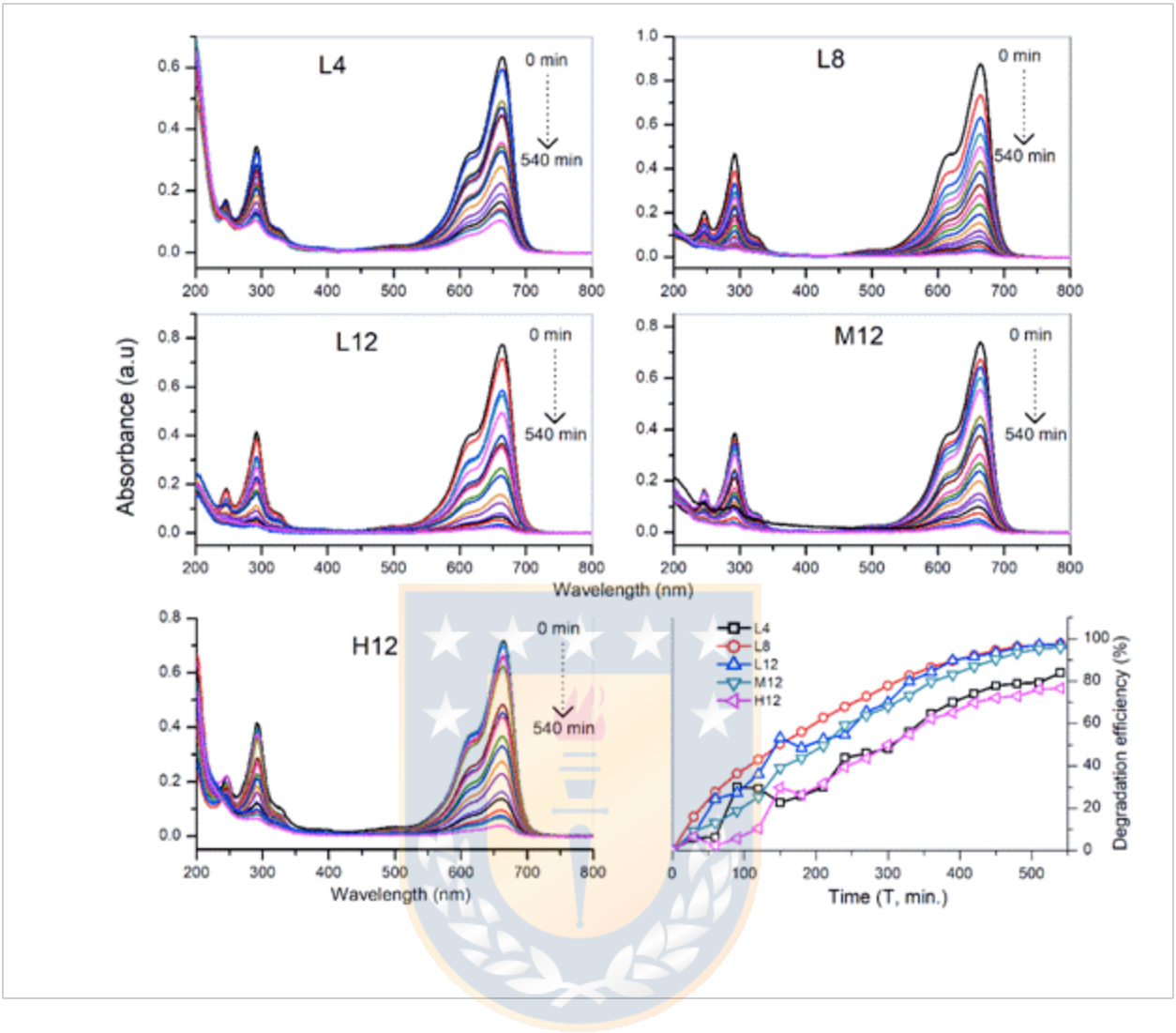

Fig. 4-21 Optical absorption of the aliquots obtained at an interval of 30 *min* from the photocatalysis chamber for different photocatalysts. The degradation efficiency of the samples for degradation of dye under visible light irradiation.

The absorption peak corresponds to MB was gradually decreased as a function of time of visible light irradiation. The absorption spectra of the aliquots collected from the photocatalysis chamber was used for the further calculations. The efficiency of catalyst for the photocatalytic degradation of the dye solution was calculated using the formula:

$$\eta = \frac{(C_0 - C_t)}{C_0} \times 100$$

where C_0 is the initial concentration, $C_0$is the concentration at a specific time (t) after visible light irradiation, and 'η' is the efficiency of photocatalytic degradation [157]. The variation of degradation efficiency with irradiation time for different samples is shown in Fig. 4-21. The observed maximum degradation efficiency of the samples is 83.91, 97.72, 97.29, 95.95 and 76.67 % for L4, L8, L12, M12 and H12, respectively. All the samples exhibited a very good efficiency in degrading the dye through photocatalysis. The apparent rate constant values were deducted by considering the first order kinetics as $ln\left(\frac{C_0}{C_t}\right) = kt$, where, k is the apparent rate constant of the photocatalysis reaction.

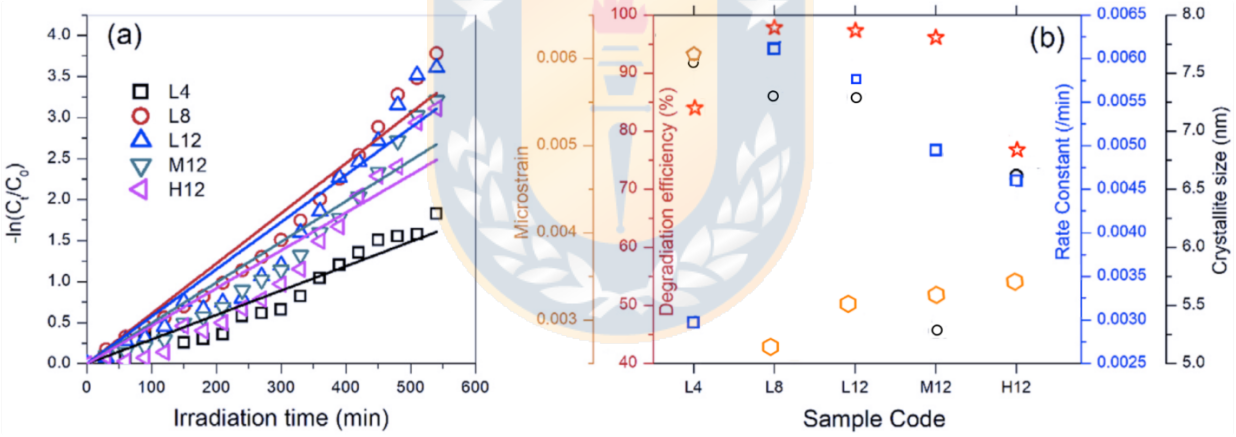

Fig. 4-22 Photocatalytic performance of the prepared ceria nanostructures with different morphology. The plots of **(a)** first-order kinetics of the various photocatalysts **(b)** variation of the rate constant along with efficiency, microstrain and crystallite size of different ceria nanostructured samples for degradation of dye under visible light irradiation.

The slope values obtained from the linear fit of the plot of $-\ln(C_t/C_0)$ vs t gives the value of the rate constant of a particular photocatalyst under consideration [157]. As shown in Fig. 4-22, by using the first order kinetics the first order rate constants were found to be 0.00297, 0.00611,

0.00576, 0.00495 and 0.0046 (/*min*) corresponds to L4, L8, L12, M12 and H12, respectively. The variation of rate constant along with the crystallite size values for different samples is shown in Fig. 4-22b. It is clearly evident that the samples L8 and L12 exhibited the highest photocatalytic activity compared to other samples. It is observed that the photocatalytic activity is decreasing with increasing the crystallite size, except for the sample M12 [157,158]. The photocatalytic activity of ceria nanostructures highly depends on the competency to separate the electron-hole pairs than recombination. When a photocatalyst interacted with photons (light source of irradiation), the electrons from the valence band (VB) get excited to the conduction band (CB) by leaving holes in the VB. The tendency of the excited electrons is to get recombine with holes by relaxing to the lower energy levels. When the charge separation activity of the photocatalyst is dominant over the recombination process, the excited electrons segregate over the surface of the nanostructures and leads to the generation of the free radicals. Thus, the charge separation capacity and generation of free radicals by a nanostructured catalyst will play a major role in the photocatalytic activity. The migration of the photo-generated electrons highly depends on the morphology and size of the nanostructures. The ceria nanostructures with spherical morphology, which possess high active surface area favored the enhanced photocatalytic activity when compared to other morphology such as nanocubes and nanorods of ceria [159]. Thus, the observed lower activity in the case of the samples L4, M12 and H12 can be attributed to their morphological changes. Also, the charge separation process tends to highly influenced by the microstrain, which in turn influenced by the defects in the nanostructures as discussed in the earlier section. In nanostructured photocatalysts, the relaxation of microstrain (low strain) favors the enhancement of photocatalytic activity by improving the charge separation [88,91]. For comparison, the variation of the microstrain and rate constant for different samples is shown in Fig. 4-22b. Thus,

it is clearly evident that the samples with lower microstrain exhibited the enhanced catalytic activity when compared with the other samples. Consequently, the observed nominal variation in the degradation efficiency of the different catalysts is attributed to microstrain variations in the samples. Shortly, The sample L8 is semi spherical morphology with high photocatalysis activity.

The crystallization of ceria nanostructures is ultrafast, (achieved within a few minutes) and signifies the imminent success of this synthesis technique for large scale. The observed variation (increases) in the band gap of ceria nanostructures was attributed to the variation (increase) in the crystallite size. In comparison, the sample L8 with nearly spherical morphology exhibited high degradation efficiency of 97.72%, the results suggested that the relaxation of microstrain (low strain) improved the charge separation and favored the enhancement in photocatalytic activity.

4.3. CeO_2 decorated ZnO nanostructures

The XRD patterns of CeO_2, ZnO and CeO_2 decorated ZnO nanostructures are depicted in Fig. 4-23. All peaks corresponding to the structure of CeO_2 nanoparticles (*JCPDS No*: 65-5923), and hexagonal wurtzite structure of ZnO (*JCPDS No*: 01-089-1397) are indexed well. The XRD of composite nanostructures confirmed the presence of CeO_2 along with the ZnO without any impurity phases. Table 4-10 shows the calculated lattice parameters from the XRD using Scherrer's formula.

Table 4-10 The structural parameters of CeO_2 and ZnO obtained from XRD analysis.

Pure Samples	**2θ**	**plane (hkl)**	**FWHM**	**D**	**a (Å)**	**c (Å)**	$\frac{c}{a}$	**v (Å³)**
CeO_2	28.52	(111)	0.908±0.006	0.312	5.41	-	-	158.89
ZnO	31.75	(100)	0.244±0.002	0.281	3.25	-	1.60	47.63
	34.40	(002)	0.234±0.004	0.260	-	5.20		

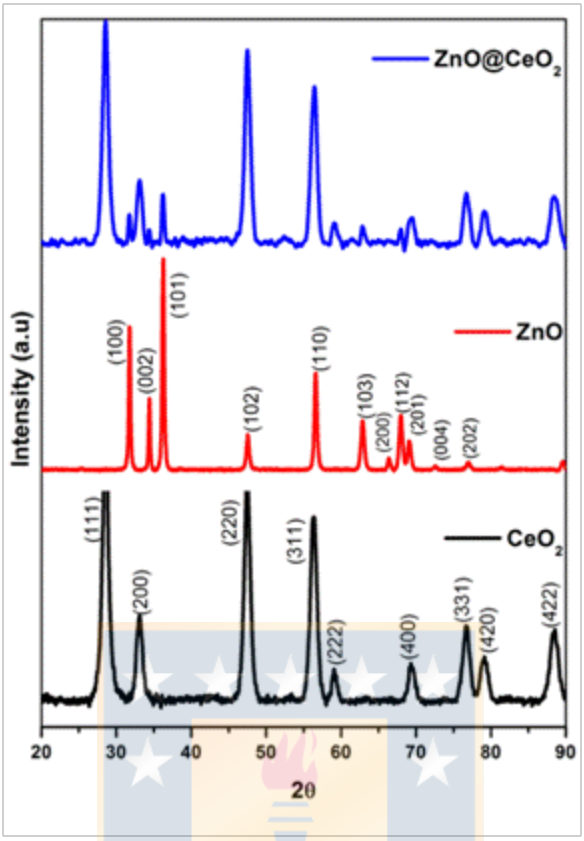

Fig. 4-23 XRD patterns of CeO_2, ZnO and ZnO@CeO_2 nanostructures.

The size and morphology of prepared nanostructures and the deposition of CeO_2 were investigated by using TEM analysis as shown in Fig. 4-24(a-d). Fig. 4-24(b) shows a TEM image of single ZnO oval with length and width of ~1μm and ~434 *nm,* respectively. The selected area electron diffraction (SAED) patterns of ZnO are indexed to hexagonal ZnO with a single crystalline, which supported the XRD results. Fig. 4-24(c) shows ~9 *nm* cubes with a lattice fringes of 0.265 *nm*, corresponding to the planar distance between the (200) planes of CeO_2. Moreover, as it can be seen in Fig. 4-24(d and e) the composite nanostructures depicted that the CeO_2 nanocubes were successfully decorated on the surface of oval ZnO nanostructures, which confirms the successful decoration of CeO_2 on the ZnO. Fig. 4-25 shows the SEM and EDS spectra of ZnO, CeO_2 and ZnO@CeO_2. The elemental analysis and linear analysis (Fig. 4-25) confirmed the presence of Zn, Ce and O in the prepared nanostructures.

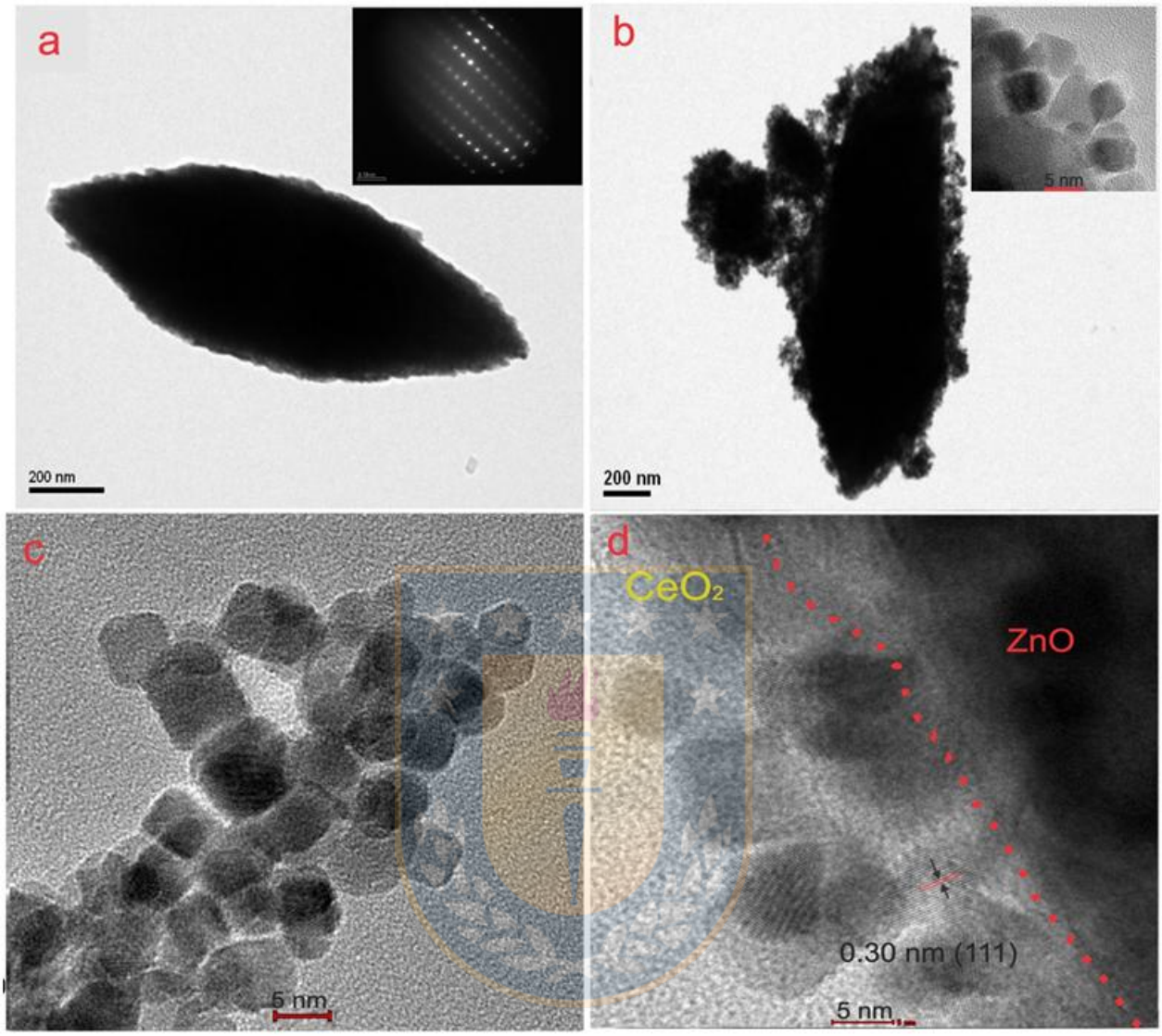

Fig. 4-24 Morphology of **(a)** ZnO **(c)** CeO_2, **(b)** and **(d)** CeO_2 on the surface of ZnO nanostructures.

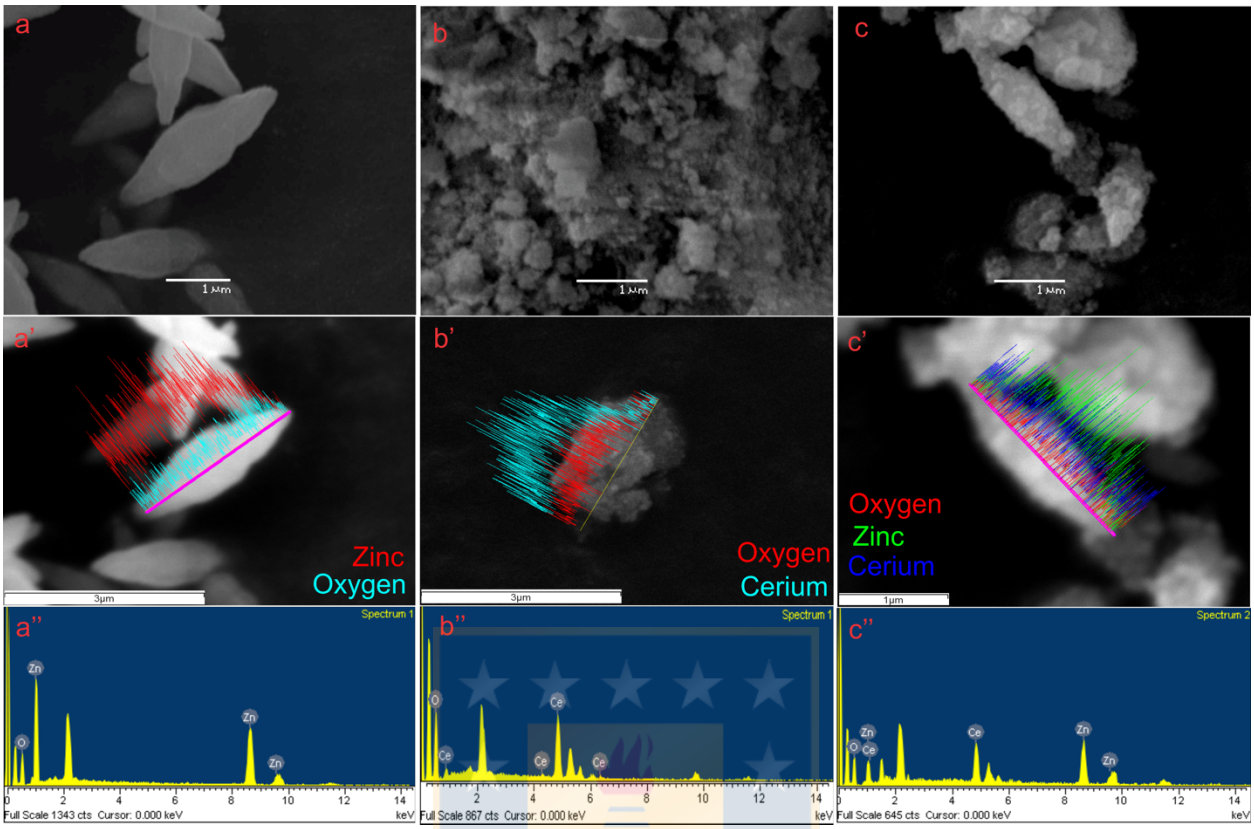

Fig. 4-25 SEM images and EDS analysis of **(a)** ZnO; **(b)** CeO_2; **(c)** CeO_2 on the surface of ZnO nanostructures.

4.3.1. X-ray photoelectron spectroscopy (XPS) studies

The elemental composition and chemical state of ZnO@CeO_2 nanostructures were confirmed using X-ray photoelectron spectroscopy (XPS). Fig. 4-26 (a-c) displays the XPS survey of ZnO@CeO_2 composite and also provided with high level spectra for O 1s, Ce 3d and Zn 2p. The ZnO@CeO_2 surface is composed of only Ce, Zn, O, and C. The XPS results of pure ZnO and CeO_2 samples are shown in Figs. 4-27 and 4-28. The binding energy peak at 285 *eV* was related to C *1s* of the adventitious surface carbon [160]. The Ce 3d core level spectrum consists of integrated peaks related to Ce^{3+} and Ce^{4+} ions. The Ce^{3+} $3d_{5/2}$ and Ce^{3+} $3d_{3/2}$ were located at 882.12 and 900.43 *eV*, respectively. The main peaks of Ce^{4+} $3d_{5/2}$ and Ce^{4+} $3d_{3/2}$ were identified at 897.75 and 916.35 *eV*, respectively [161]. The *Zn 2p* core level spectrum consists of peaks related to *Zn*

2p3/2 and *Zn 2p1/2* which were located at 1021.74 and 1044.84 *eV*, respectively. The two peaks of O 1s spectra located at 528.9 and 530.8 eV were assigned to Ce-O bond in CeO_2 [162,163] and Zn-O band in ZnO [35,164,165], respectively.

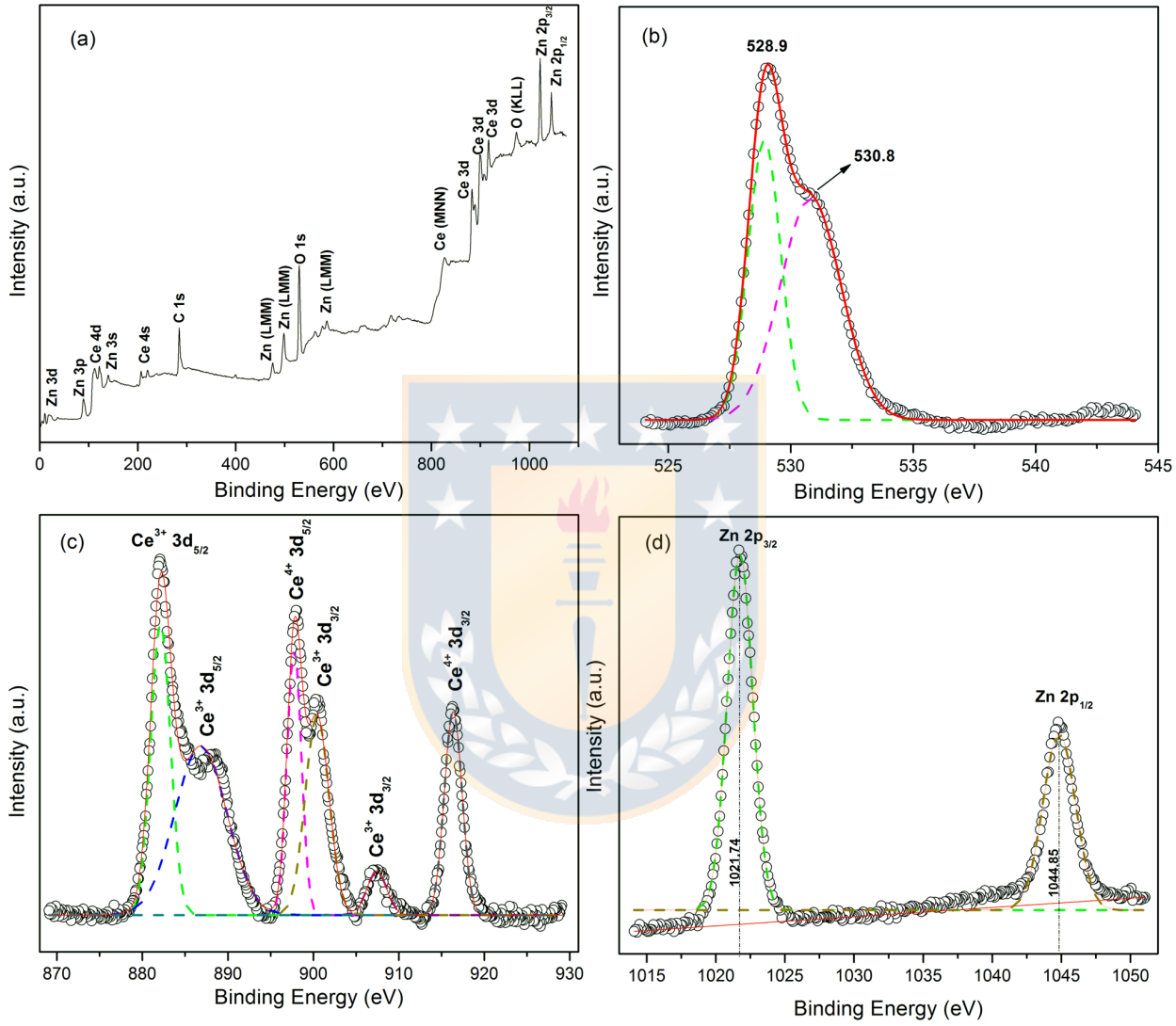

Fig. 4-26 (a) XPS survey, (b) *O 1s*, (c) *Ce 3d*, **(d)** *Zn 2p* core level spectra collected for CeO_2 on the surface of ZnO nanostructures.

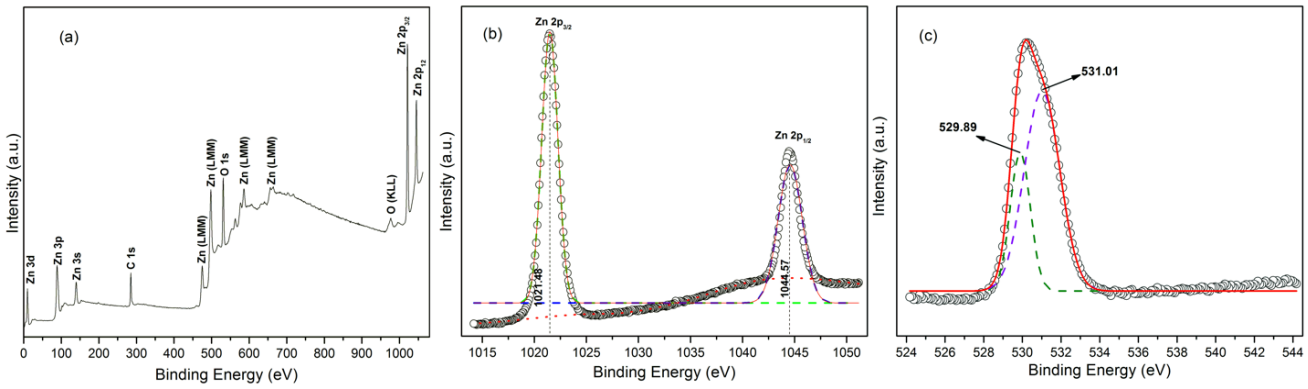

Fig. 4-27 (a)XPS survey, **(b)** Zn 2p, and **(d)** O 1s core level spectra collected for ZnO nanostructures.

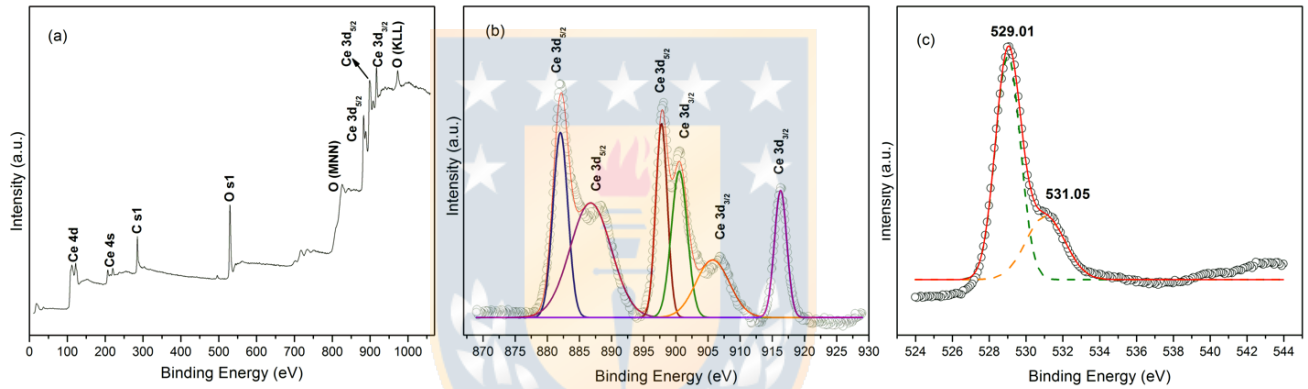

Fig. 4-28 (a) XPS survey, **(b)** Ce 3d, and **(c)** O 1s core level spectra collected for CeO_2 nanostructures.

Table 4-11 X-ray photoelectron spectroscopy (XPS) results for ZnO, CeO_2 and ZnO@CeO_2

sample	Binding energy (eV)							
	O 1s **Ce-O**	O 1s **Zn-O**	Zn $2p_{1/2}$	Zn $2p_{3/2}$	Ce^{3+} $3d_{5/2}$	Ce^{3+} $3d_{3/2}$	Ce^{4+} $3d_{5/2}$	Ce^{4+} $3d_{3/2}$
ZnO	-	530	1021.48	1044.57	-	-	-	-
CeO_2	529	-	-	-	881	889.74	897.50	917.10
ZnO@CeO_2	528.9	530.8	1021.78	1044.84	882.12	900.43	897.75	916.35

4.3.2. Optical properties of CeO_2 decorated ZnO

The diffuse reflectance spectra (DRS) of ZnO, CeO_2 and ZnO@CeO_2 nanostructures in the range of 200-800 *nm* are shown in Fig. 4-29. The band gap was obtained from the UV-Vis DRS spectra by using the *Kubelka-Munk* Function F(R) [118,166,167]. The optical band gap energy (E_g) was obtained by extrapolating the linear portion of each plot (Fig. 4-29b). The E_g values of CeO_2 and ZnO were determined to be 3.239 and 3.259 *eV*, respectively. These can be ascribed to the transitions of charge-transfer between O 2*p* and Ce 4*f* orbitals in CeO_2 and excitonic absorption of ZnO nanostructures [108,168]. The CeO_2 decorated ZnO nanostructures exhibited a slight shift (3.34 *eV*) in the band gap. Fig. 4-29 depicts the room temperature PL spectra of CeO_2, ZnO and ZnO@CeO_2 nanostructures. The PL spectra of CeO_2 showed dominant broad ultraviolet and less intense visible emission.

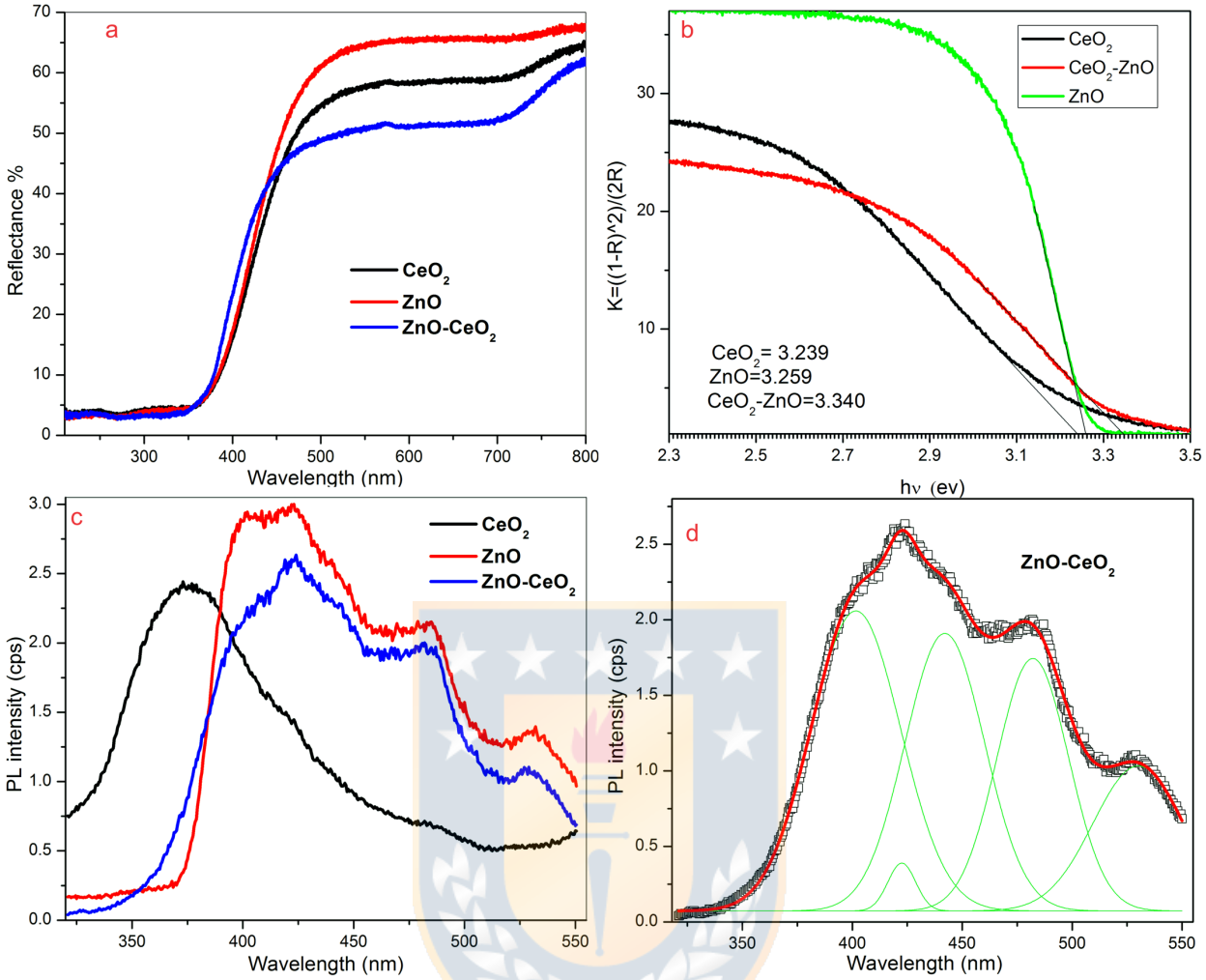

Fig. 4-29 (a) DRS spectra of CeO_2, ZnO and CeO_2 decorated ZnO nanostructures, **(b)** the plot of $\frac{(1-R)^2}{2R}$ vs. *hv*, **(c)** PL spectra of CeO_2, ZnO and CeO_2 decorated ZnO nanostructures and **(d)** Gaussian decomposed PL spectra of CeO_2 decorated ZnO nanostructures.

To identify the individual emission bands, each spectrum was fitted using a Gaussian function (Fig. 4-30), and the same for ZnO@CeO_2 nanostructures is shown in Fig. 4-29d. The fitted PL spectra of CeO_2 consist of a strong UV band (356 *nm*) and two less intense visible emission bands (441 and 482 *nm*). The strong UV band can be attributed to the hopping of electrons in the localized Ce 4*f* state to holes in the O 2*p* valence band, whereas the visible emission bands

can be attributed to the presence of defects such as oxygen vacancies [169]. Similarly, the fitted PL data of ZnO exhibited a strong peak in UV (394 *nm*) and two less intense visible emission bands (483 and 529 *nm*). The emission peak located at 394 *nm* was due to free exciton related to the near band emission (NBE) in ZnO nanostructures [125]. The UV emission band can be attributed to the band to band transition and the visible emission bands were resulted from the transition of electrons in the defect levels such as zinc vacancy, zinc interstitial, oxygen vacancy and oxygen interstitial [116]. The composite nanostructures exhibited the blue shift in the PL bands due to the strong interaction between CeO_2 and ZnO [170].

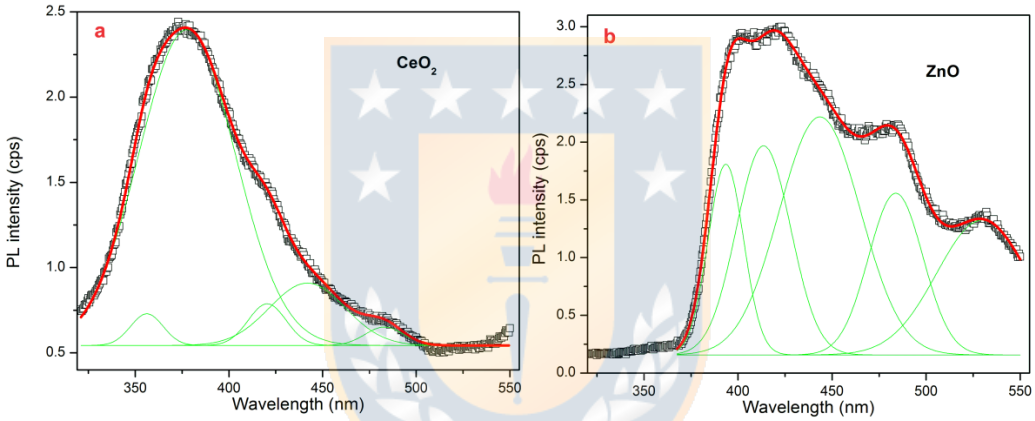

Fig. 4-30 Gaussian decomposed PL spectra of CeO_2 and ZnO.

4.3.3. Photocatalytic activities of CeO_2 decorated ZnO

The photocatalytic properties of the CeO_2, ZnO and ZnO@CeO_2 nanostructures were examined by degradation of MB. The characteristic absorption at 664 *nm* of MB was taken into consideration to monitor the photocatalytic degradation process (Fig. 4-31).

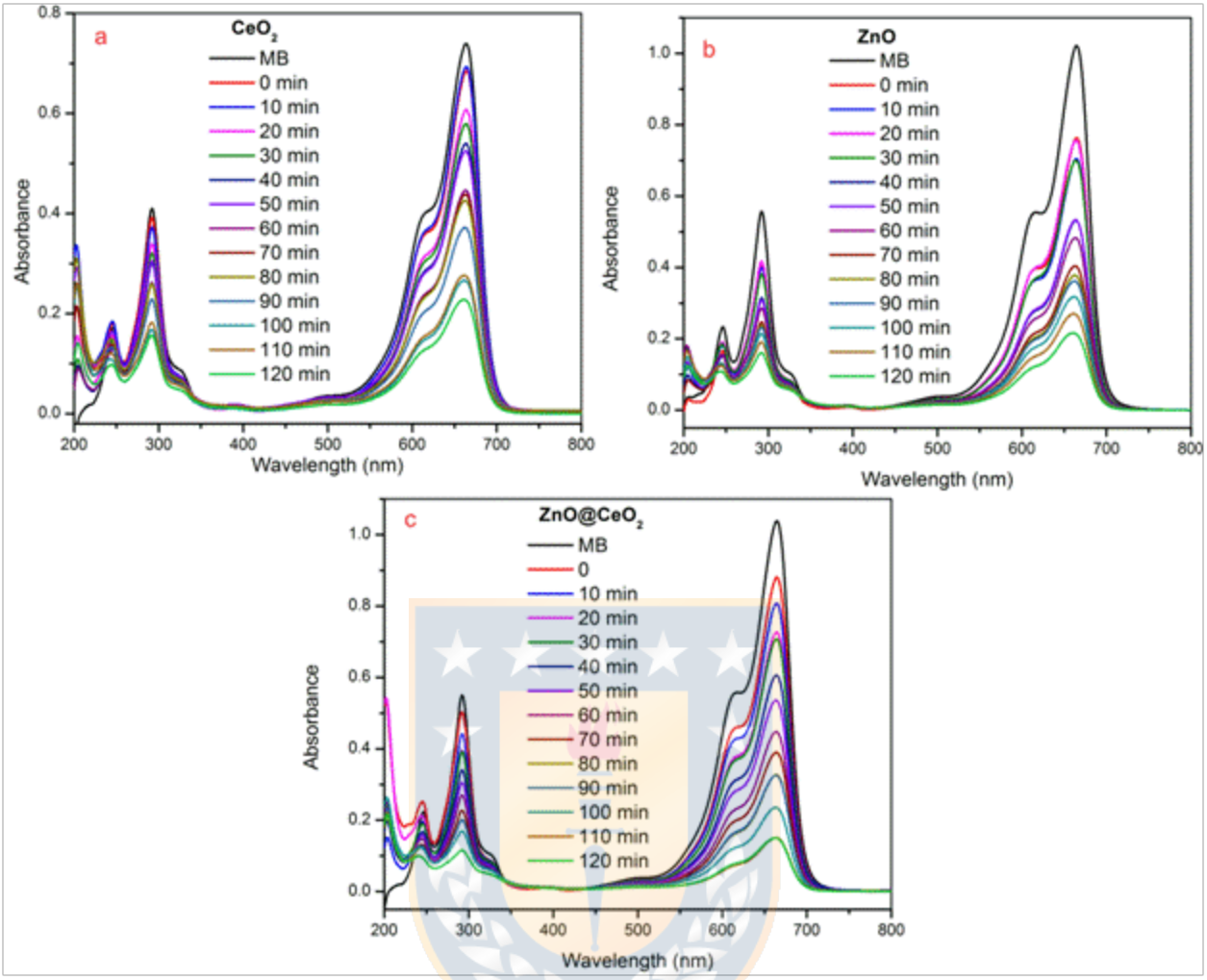

Fig. 4-31 UV-visible absorbance spectra of photodegradation of MB in the presence of CeO_2, ZnO and CeO_2 coated ZnO nanostructures.

The degradation efficiency of MB in an aqueous solution (5mg/l) containing the prepared catalysts nanostructures (10mg) under visible light radiation with respect to the time is shown in Fig. 4-32(a). The decoloration efficiency was calculated through the following relation,

$$\text{Decoloration efficiency} = \left(1 - \frac{C_o}{C}\right) \times 100$$

where, C_o and C are the absorbance maxima of the MB dye before and after visible light irradiation, respectively. For an exposure duration of 120 min, the pure CeO_2 and ZnO nanostructures exhibited a degradation of 69.20 and 80.25%, respectively. The photocatalytic degradation performance of the ZnO@CeO_2 nanostructures against MB was considerably improved so that the decoloration efficiency was observed as 85.01%. The improved separation of photogenerated charge carriers, electrons and holes in the composite nanostructures led to the enhancement of the photocatalytic activity [104,171]. The photocatalytic degradation of MB under visible light obeying pseudo-first order kinetics is expressed by [172],

$$\ln\left(\frac{C}{C_0}\right) = -k_{app} \times t$$

where t is time duration and k_{app} is the apparent rate constant which was found to be 0.00816±4.160E-4, 0.01387±5.937E-4 and 0.0136±9.105E-4 for CeO_2, ZnO and ZnO@CeO_2 nanostructures, respectively (Fig. 4-32b). In order to assess the stability of the photocatalyst, recycling experiments for the degradation of MB were performed with 1each catalyst upto four cycles (Fig. 4-33). The MB degradation efficiency of ZnO-CeO_2 was higher than those of pure CeO_2 and ZnO. The calculated reaction rate constant of four cycles are tabulated in Table 4-12.

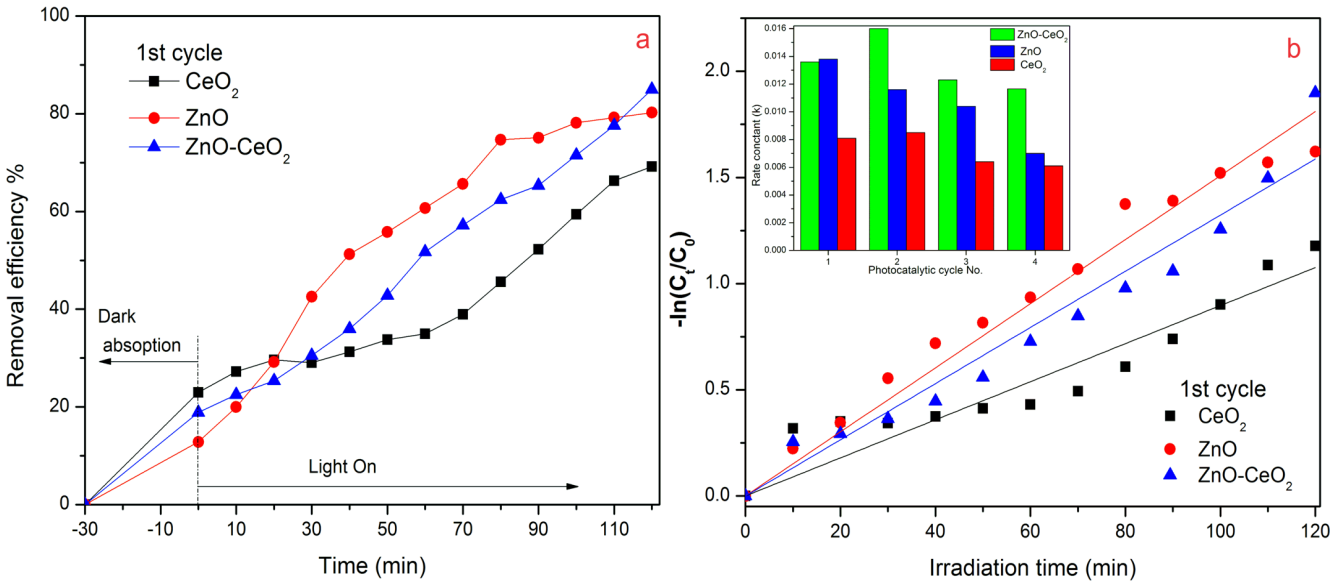

Fig. 4-32 (a) Decoloration efficiency of MB under visible light irradiation **(b)** Degradation of MB, $-\ln(C/C_0)$ plotted as a function of visible light irradiation time.

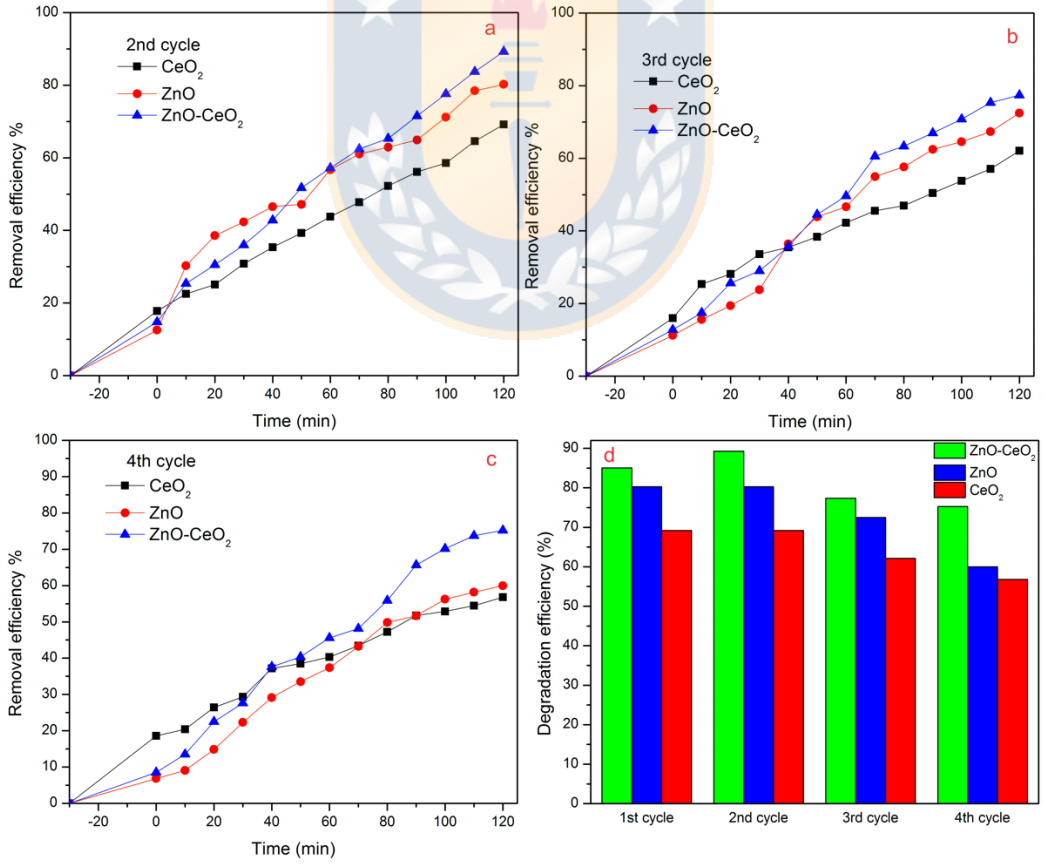

Fig. 4-33 Recycle performance and efficiency of MB under visible light irradiation.

Table 4-12 Degradation efficiency (Df) and rate constant (*k, min^{-1}*) of all prepared photocatalysts.

Sample	1st cycle		2nd cycle		3rd cycle		4th cycle	
	Df (%)	*k* (min^{-1})	Df (%)	*k* (min^{-1})	Df (%)	*k* (min^{-1})	Df (%)	*k* (min^{-1})
ZnO	80.25	0.0138	80.25	0.0116	72.46	0.0104	59.97	0.007
CeO_2	69.20	0.0081	69.16	0.0085	62.11	0.0064	56.78	0.0061
ZnO-CeO_2	85.01	0.0136	89.29	0.0160	77.36	0.0123	75.23	0.0116

In general, the photocatalytic reaction involves the light absorption using a semiconductor material by e^- transfer from the valence band (VB) to the conduction band (CB) and creating h^+ in the VB. The photocatalytic mechanism typically contains three main components: hydroxyl radical, superoxide anion radical and h^+, where $\bullet OH$ is the principal oxidant in the photocatalytic conversion of the organic pollutant [173]. The conduction and valence bands of ZnO lie below the conduction and valence band of CeO_2, respectively. Hence, under visible irradiation, the photogenerated electrons from CB of CeO_2 are moved to the CB of ZnO where they react with adsorbed oxygen atom and produces superoxide radical ($O_2^{\cdot-}$). The $O_2^{\cdot-}$ radicals then combined with an electron to form hydrogen peroxide. Furthermore, the photogenerated holes (h^+) are moved from the VB of ZnO to the VB of CeO_2. Therefore, the combination of electrons and holes pairs was prevented, which led to the enhancement of photocatalytic efficiency of ZnO@CeO_2 nanostructures in photocatalysis [171]. The reactive oxygen species (ROS) can generate on the photocatalytic activity of semiconductor nanoparticles. The VB and CB of semiconductor materials determine the type of ROS. Typically, ROS includes a singlet molecular oxygen ($^1O_2$), hydroxyl radical ($\cdot OH$) and superoxide radical ($O_2^{\cdot}$). The mechanism is summarized in the following reactions [171];

$$ZnO + hv \rightarrow e^- + h^+$$

$$CeO_2 + hv \rightarrow e^- + h^+$$

$$e^-_{(CB\ ZnO)} + O_2 \rightarrow O_2^{\cdot -}$$

$$2^{\cdot}OOH \rightarrow H_2O_2 + O_2$$

$$H_2O_2 + e^- \rightarrow {}^{\cdot}OH + OH^-$$

$$O_2^{\cdot -} + MB_{(Dye)} \rightarrow CO_2 + H_2O$$

$$h^+_{(VB\ CeO_2)} + OH^- \rightarrow {}^{\cdot}OH$$

$${}^{\cdot}OH + MB_{(Dye)} \rightarrow CO_2 + H_2O$$

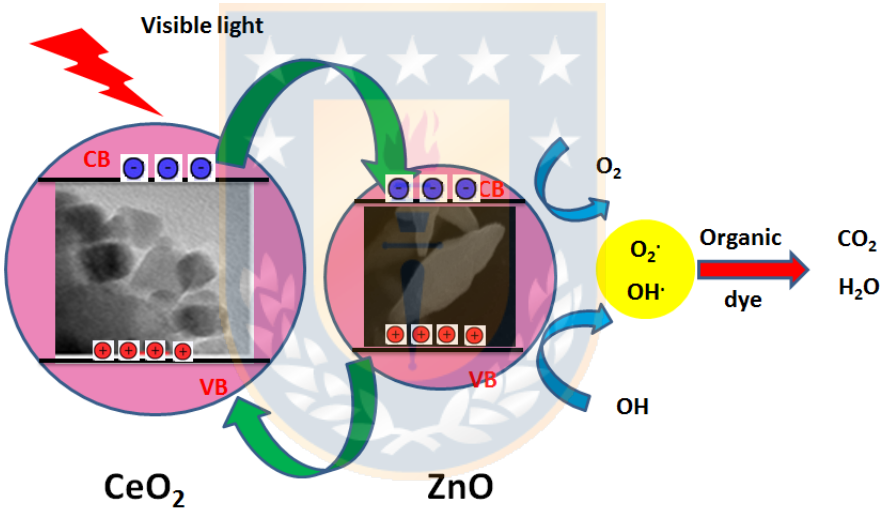

Fig. 4-34 Schematic representation of photocatalytic mechanism of CeO_2@ZnO.

By the decoration of CeO_2 on the surface of ZnO, the nanostructures effectively extends the spectral response in visible region through overlapping and bending of their energy bands and hence new energy level was formed with lesser band gap. This resulted in the reduction of electron-hole pair recombination which led to the enhancement of the photocatalytic efficiency of ZnO@CeO_2 in the visible region [171].

4.4. $ZnO@CeO_2$ core shell nanostructures

Different strategy has been adopted in order to achieve uniform ceria shell on the ZnO core, as follows; The core materials consists of pristine ZnO was prepared through simple wet chemical precipitation. These primitive ZnO rod structures were used to prepare $ZnO@CeO_2$ core shell nanostructures selected from our rod ZnO product with minimum defect and more uniform size. The ZnO nanostructures were dispersed ultrasonically in a solution of water and ethanol with an equal ratio. Then, 8.68 mg of cerium (III) nitrate hexahydrate ($Ce(NO_3)_3 \cdot 6H_2O$) was added into the above solution and sonicated. Afterwards, 15 mL of HMTA solution (0.02 gL^{-1}) was added into the final mixture under stirring. Then the temperature of the mixture was increased to 90 °C and kept under reflux for 2 h. A similar procedure was repeated for the different amounts (30 and 50 mL) of HMTA solution.

In the same way, another set of samples were prepared by hydrothermal (150 °C, 3h) technique instead of reflux in the above-mentioned reaction sequence. The products were collected by centrifugation and washed with water and ethanol to remove unreacted products. The obtained products were dried at 60 °C for 6 h and subjected to calcination at 350 °C for 1 h.

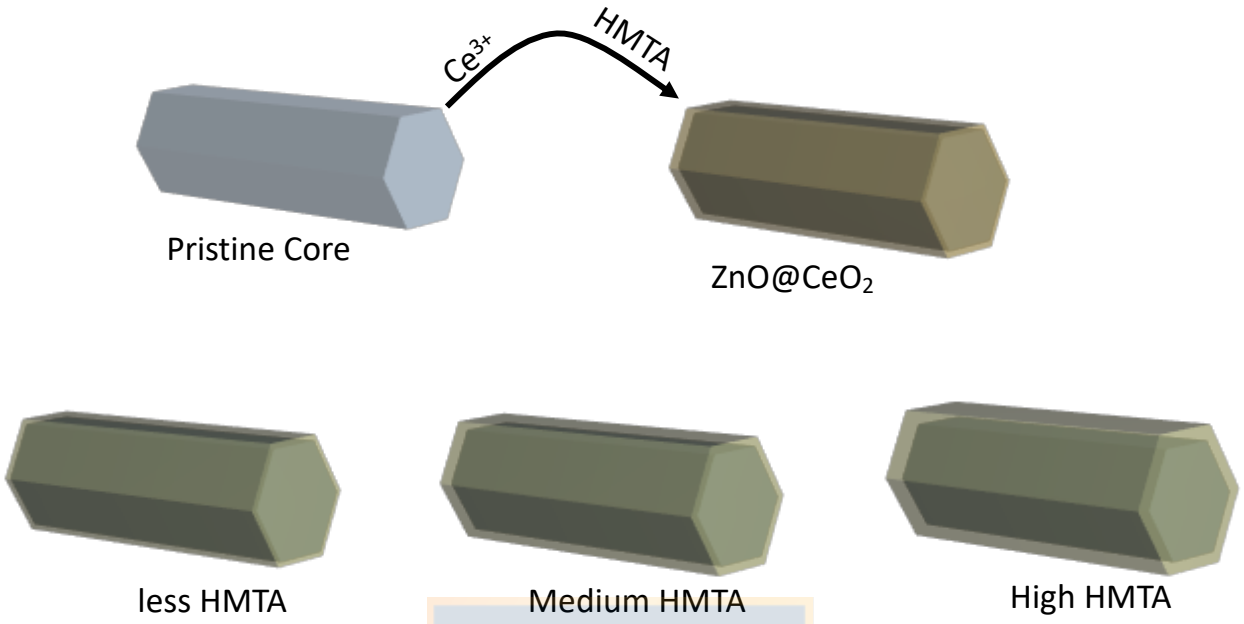

Fig. 4-35 Schematic formation of ZnO@CeO_2 core shell with difference shell thickness.

4.4.1. ZnO@CeO_2 morphological studies

The FE-SEM and TEM micrographs of all the prepared core-shell nanostructures by co-precipitation and hydrothermal technique are depicted in Figs. 4-36 and 4-37, respectively. The six sided ZnO rods were clearly identified which was demonstrated as inset of Fig. 4-37a. The observation of uniform shell layer consisting of the aggregation of fine CeO_2 nanoparticles covering the surface of ZnO (Core) confirmed the successful formation of ZnO@CeO_2 core-shell nanostructures. Figs. 4-36 and 4-37 (A', B' and C') show the TEM image of ZnO@CeO_2 core-shell. The thickness of shell was estimated from the TEM images. Furthermore, the HRTEM images depicted that the ceria nanoparticles are well surrounded the surface of ZnO which was confirmed by the characterization of lattice fringes in high resolution TEM image.

In this study, to the preparation of core-shell ZnO@CeO_2, the HMTA play important role in the realization of thin layer of nanoparticles of CeO_2 on ZnO rods through co-precipitation and

hydrothermal methods. The elemental analysis of ZnO@CeO2 core shell structures were examined through SEM-EDS mapping and results are summarized in Table 4-13.

Table 4-13 Elemental composition of ZnO@CeO_2 core shell structures

$ZnO@CeO_2$ core shell	**Method**	**HMTA (ml)**	**O (wt%)**	**Zn (wt%)**	**Ce (wt%)**
	Hydrothermal	15	14.65	83.90	1.45
		30	18.07	76.00	5.93
		50	24.01	67.35	8.64
	Co-precipitation	15	24.73	73.09	2.18
		30	22.22	72.25	5.53
		50	25.68	67.30	7.02
ZnO (Core)			25.64	74.36	-

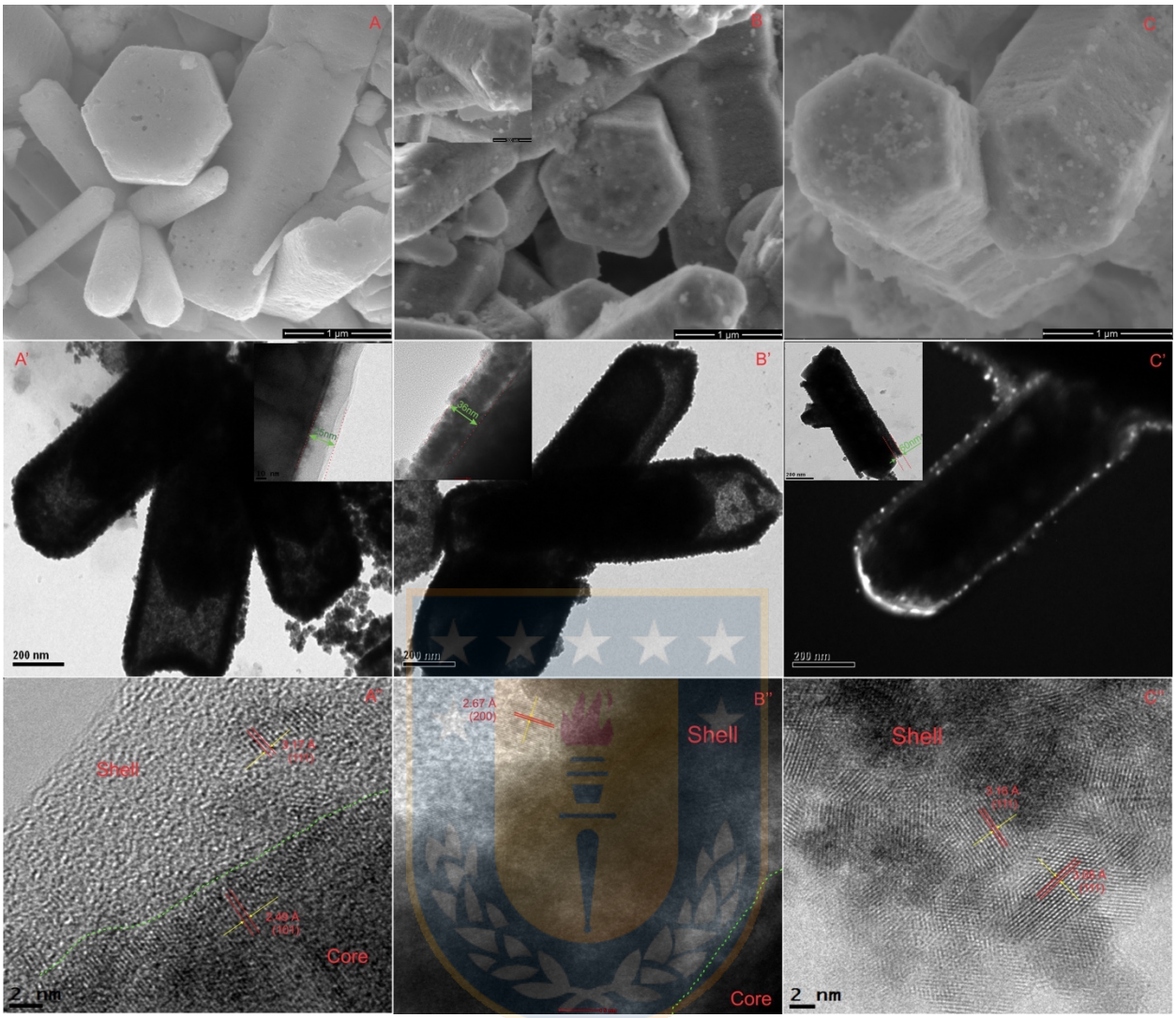

Fig. 4-36 SEM, TEM and HRTEM images of ZnO@CeO_2 core shell structure via coprecipitation **(A)** 15 ml **(B)** 30 ml **(C)** 50 ml of HMTA. The inserts in TEM images (A', B' and C') show the thickness of shell.

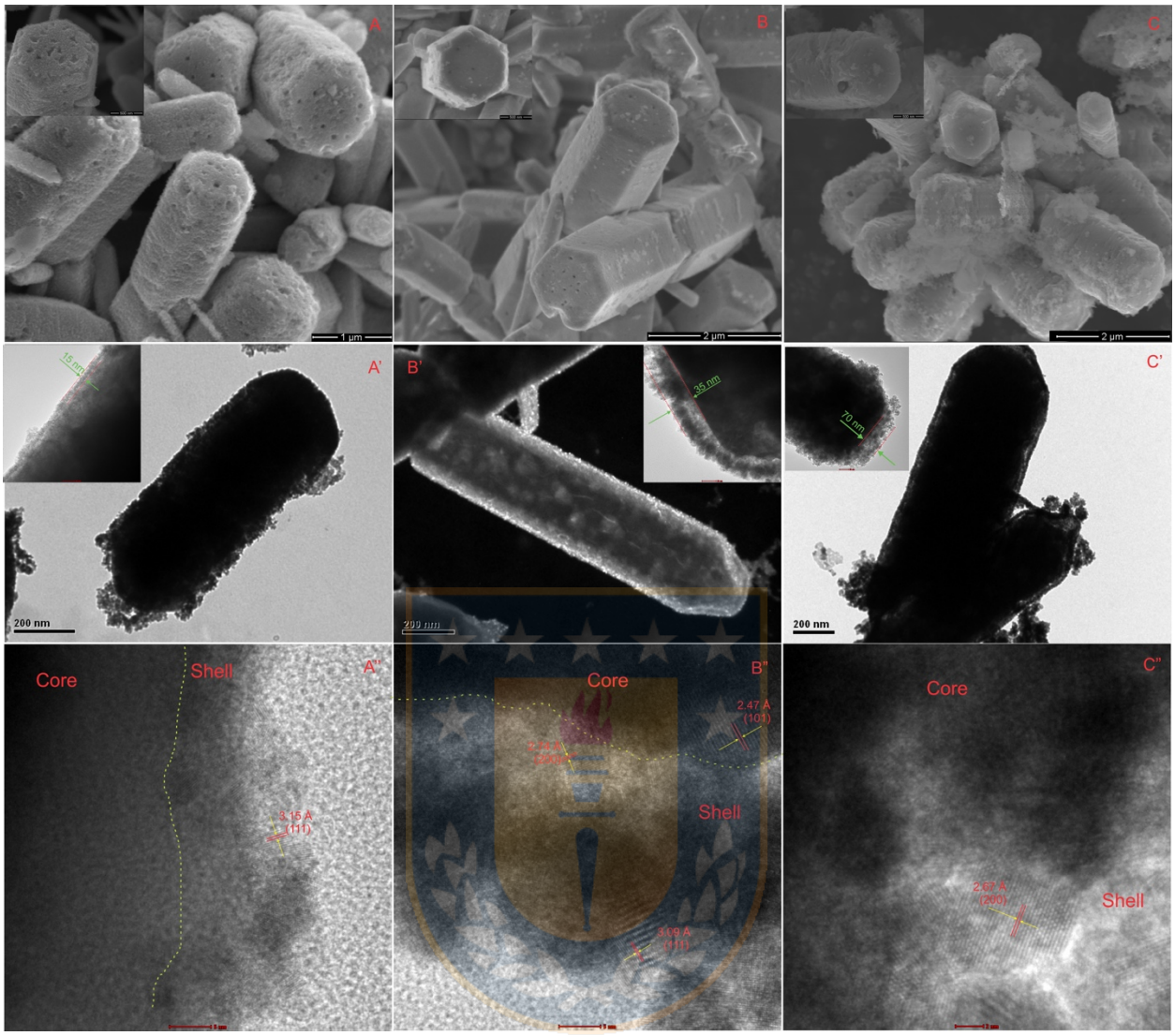

Fig. 4-37 SEM, TEM and HRTEM images of $ZnO@CeO_2$ core shell nanostructures prepared via hydrothermal method using **(A)** 15 ml **(B)** 30 ml and **(C)** 50 ml of HMTA. The insets in TEM images (A', B' and C') provided with the thickness of shell.

It is important to point that without HMTA, the independent nucleation of ceria led to precipitation of ZnO/CeO_2 composites structures [33,174]. HMTA has a heterocyclic structure with three rings of configuration and four nitrogen atoms [175]. Therefore, HMTA decomposes to formaldehyde and ammonia in aqueous medium upon heating [176,177]. Later it provides

controlled source of hydroxyl ion (OH^-) by increasing the temperature to precipitation chemical reaction [178].

$$(CH_2)_6.N_4 + 9H_2O \rightarrow 4NH_2^+ + 3OH^- + 6CH_2O$$

The available OH^- reacts in Ce^{3+} ions of cerium(III) nitrate hexahydrate to form unstable cerium hydroxide, which will smoothly undergoes oxidation process to cerium(IV) hydroxide in the form of precipitate [179]. The cerium(IV) hydroxide is hydrolyzed to cerium oxide by losing the hydroxyl groups [176].

$$Ce(NO_3).6H_2O \rightarrow Ce^{3+} + 3HO^- + 6H_2O$$

$$2Ce + 6H_2O \leftrightarrow 2Ce(OH_3) + 3H_2$$

$$2Ce(OH_3) + H_2O \rightarrow 2Ce(OH)_4$$

$$Ce(OH)_4 \rightarrow 2Ce(OH)_4 + 2H_2O + 4H^+$$

From the morphological studies, it was observed that the ceria shell thickness was increased with the amount of HMTA.

4.4.2. ZnO@CeO_2 structural analysis

Fig. 4-38 shows the XRD patterns of the prepared ZnO@CeO_2 core shell nanostructures. The XRD peaks were well indexed to wurtzite hexagonal ZnO and cubic fluorite CeO_2 structures with the *JCPDS* #04-04593 and #36-1451, respectively. The absence/no additional peaks signified the successful formation of the ZnO@CeO_2 core shell nanostructures without nay impurity phases.

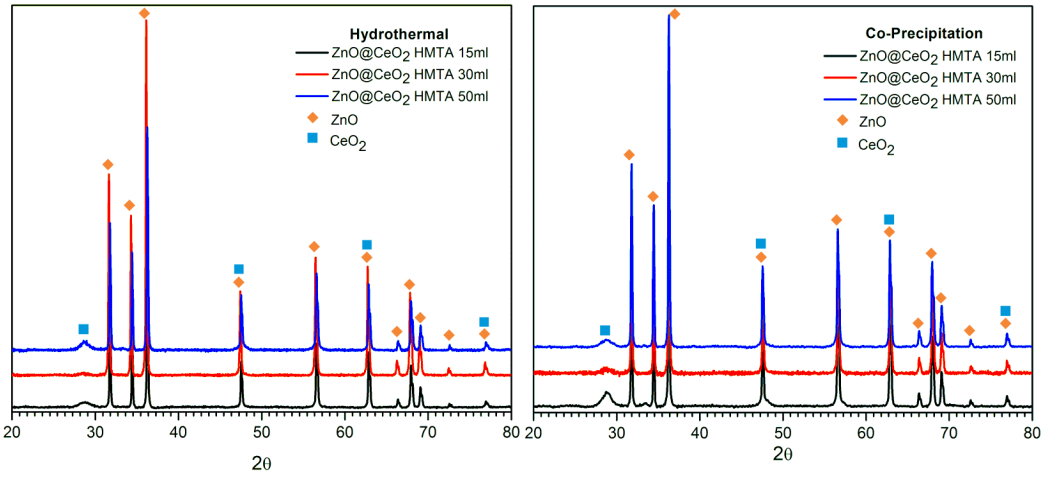

Fig. 4-38 XRD patterns of ZnO@CeO_2 core shell nanostructures obtained from two different methods.

The XRD pattern of samples exhibited various peaks centered at around 31.6°, 34.4°, 36.1°, 56.5°, 66.34°, 67.85°, 69.11°, and 72.64°are indexed with (100), (002), (101), (110), (200), (112), (201) and (004) reflection planes of ZnO crystal structure, respectively. The broad peaks located at 28.8° and 33.3° are corresponds to (111) and (200) planes of a ceria nanoparticles. The average crystallite size of CeO_2 and ZnO were calculated by using Debye Scherrer equation and given in Table 4-14. The XRD peaks located at 47.48°, 62.83°and 76.91° were duplicated between ZnO and CeO_2. The crystallite size values were estimated by using the Scherrer equation [116]. For co-precipitation synthesis of ZnO@CeO_2, the acquired values of crystallite size of CeO_2 (shell) were found in 7.11, 7.13 and 6 *nm* corresponding to with 15, 30, and 50 mL HMTA, respectively. Whereas in the case of the hydrothermal method, these were 10.6, 7.2, and 14.6 *nm* corresponding to 15, 30 and 50 mL HMTA, respectively. The lattice parameters *a* and *c* of ZnO (core) were found to be 3.2 and 5.2 Å, respectively. For all the repapered samples, those values are almost same as that of pure nano ZnO.

Table 4-14 Parameters obtained from XRD pattern of ZnO@CeO_2 core shell structure.

HMTA	Co-Precipitation				Hydrothermal			
	ZnO		CeO_2		ZnO		CeO_2	
	a	c	crystallite size	a	a	c	crystallite size	a
15	3.253	5.21	7.11	5.37	3.246	5.199	10.6	5.38
30	3.240	5.20	7.13	5.36	3.245	5.198	7.2	5.37
50	3.256	5.21	6	5.38	3.252	5.20	14.6	5.39

4.4.3. Diffused reflectance spectra (DRS) studies

To study the optical properties of ZnO@CeO_2 core shell nanostructures, all samples were characterized by using UV-vis diffused reflectance spectra (DRS). The percentage of reflectance was used for *Kubelka-Munk* equation $F(R) = \frac{(1-R)^2}{2R}$, where R is the diffuse reflectance. The band gap of prepared samples was estimated by extrapolating the linear portion of $(F(R)h\nu)^2$ *vs* hν plots. The calculated band gap of ZnO@CeO_2 core shell and core is listed in Fig. 4-39. The estimated band gap energy of ZnO (core) is 3.289 eV which is in pursuant to previous reports [180,181].

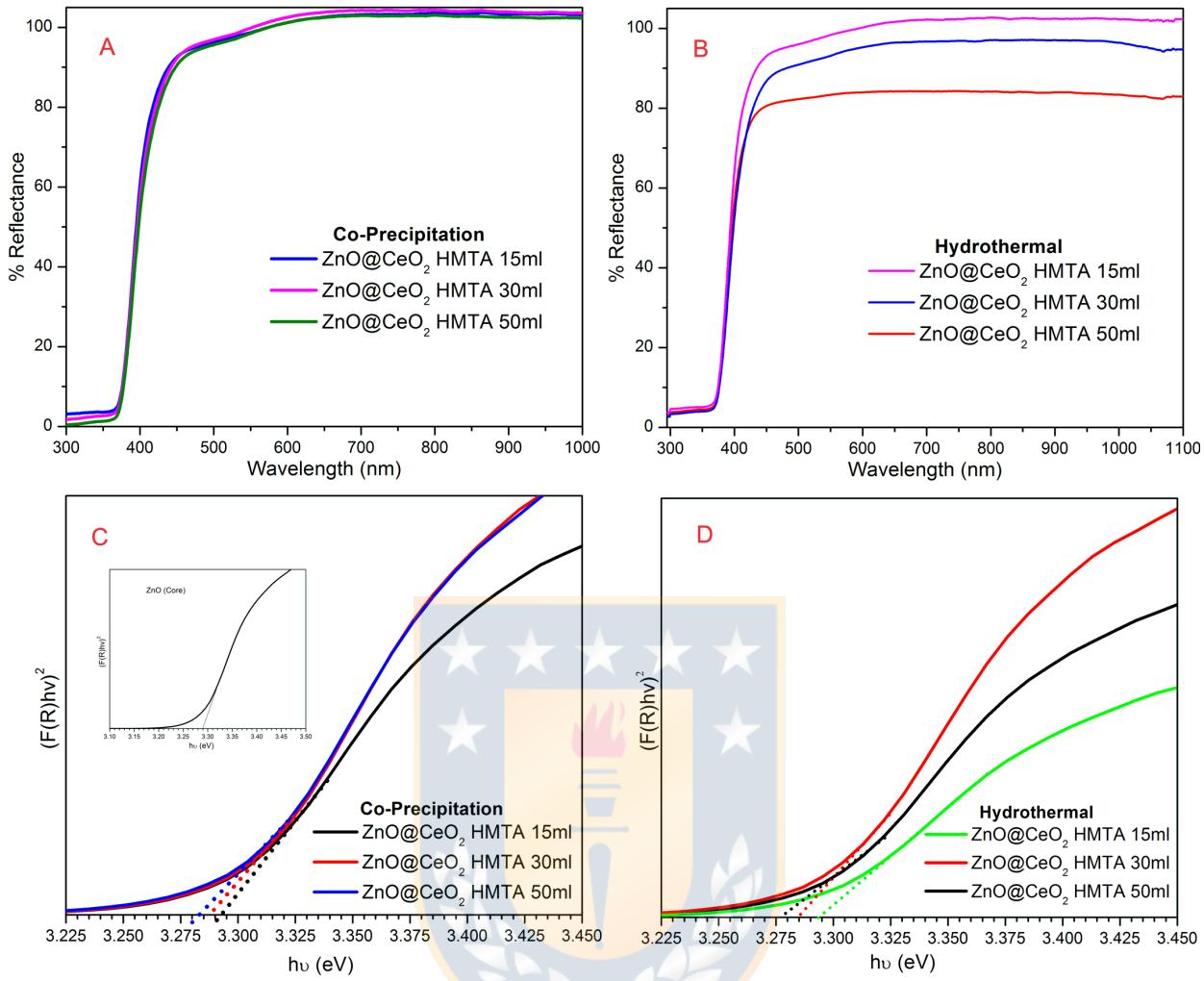

Fig. 4-39 (A & B) UV-vis diffuse reflectance spectra of ZnO@CeO_2 core shell structure synthesis via two different methods, coprecipitation and hydrothermal and (C & D) plots of '$(F(R)\ hv)^2$'*vs 'hv'* for the estimation of direct band gap. The inset of C is provided with *tauc* plot of pure ZnO (core).

Furthermore, the estimated band gap of the core is lower than the band gap of bulk ZnO, which may be ascribed to defects of ZnO such as ionized oxygen vacancies. The calculated band gap values ZnO@CeO_2 nanostructure synthesized by co-precipitation method were found to be 3.286, 3.282, and 3.280 eV. The band gap values for the samples obtained from the hydrothermal

method were found to be 3.293, 3.288, and 3.283 eV. Thus, from the tabulated values of band gap (Table 4-15), it was evident that the band gap of ZnO@CeO_2 core shell nanostructures was decreased with an increase in the shell thickness as illustrated in Fig. 4-40.

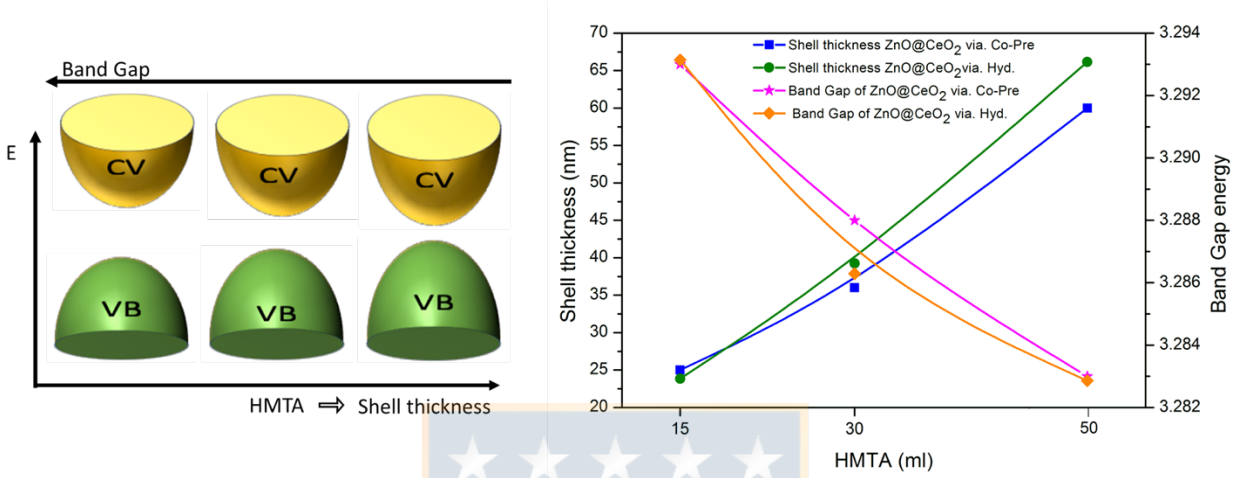

Fig. 4-40 Bandgap of ZnO@CeO_2 core shell NPs as fraction of shell thickness.

Table 4-15 Band gap and shell thickness are tabulated for comparison

Mode/HMTA content	15		30		50	
	Band gap	Shell thickness (*nm*)	Band gap	Shell thickness (*nm*)	Band gap	Shell thickness (*nm*)
Co-Precipitation	3.293	25	3.288	36	3.283	60
Hydrothermal	3.286	15	3.382	35	3.280	70

4.4.4. Photoluminescence studies

The photoluminescence (PL) spectroscopy technique can reveal several important information about the surface defects, surfaces states and, oxygen vacancies [182]. The incident photon induces charge carries separation and recombination processes in semiconductor materials [183]. The room temperature PL emission spectra (excitation wavelength 330 *nm*) of ZnO@CeO_2 core shell are shown in Figs. 4-41 and 4-42. The PL spectra of all the samples exhibited a strong

emission band in the UV region related to the band edge emission and a weak broad emission in the visible region due to various structural defects presents in the ZnO and CeO_2 nanostructures. However, there were differences in PL intensities which were observed due to the interfacial effect between the core and shell materials [13]. To decompose the broad spectra into discrete peaks, those spectra were fitted using Gaussian function; the fitted bands are presented in part of Figs. 4-41 and 4-42 and the obtained parameters are tabulated (Table 4-16). The spectra mainly consist of five emission bands; a strong intense ultraviolet emission and relatively weak violet band, blue band, blue-green emission and green band which are located at 394 (~3.14), 416(2.98~), 448(~2.76), 488(~2.54) and 531(~2.33) *nm* (eV), respectively. The observed sharp peak at 394 nm was considered as a signature of the wurtzite ZnO crystalline structure [184].

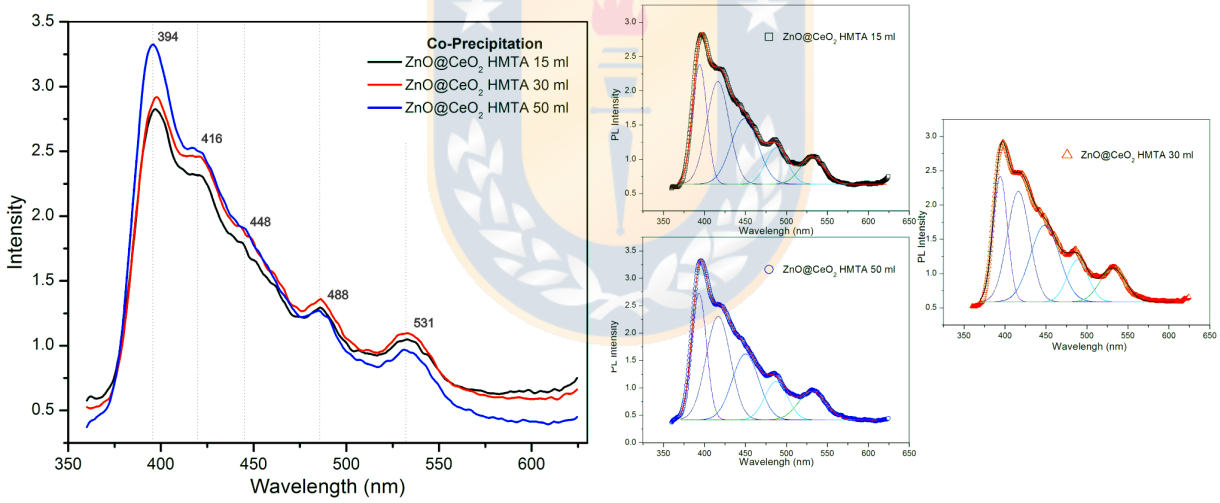

Fig. 4-41 Photoluminescence spectra of ZnO@CeO_2 Core shell nanostructures via coprecipitation method.

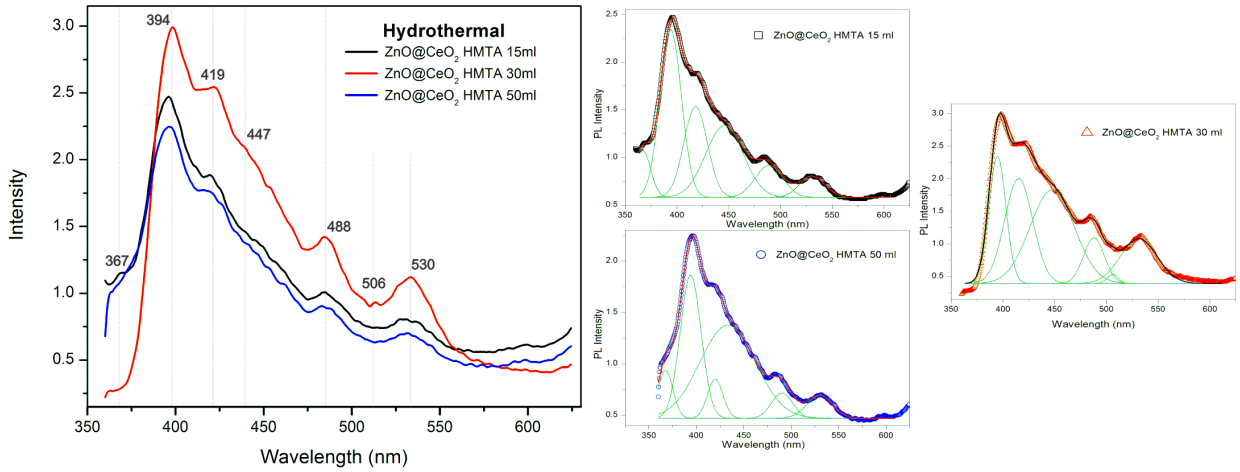

Fig. 4-42 Photoluminescence spectra of ZnO@CeO_2 core shell nanostructures *via* coprecipitation method.

Table 4-16 Parameters obtained from the PL data.

Co-Precipitation/ HMAT (ml)					
15		**30**		**50**	
Peak Center	Intensity	Peak Center	Intensity	Peak Center	Intensity
394	2.390	394	2.438	393	2.739
416	2.14	416	2.200	416	2.302
448	1.619	448	1.704	450	1.628
488	1.187	488	1.205	487	1.113
531	1.031	531	1.091	531	0.953
Hydrothermal					
15		**30**		**50**	
Peak Center	Intensity	Peak Center	Intensity	Peak Center	Intensity
366	1.073	--	--	367	0.942
393	2.320	394	2.339	394	1.868
418	1.539	415	2.019	419	0.859
446	1.338	447	1.837	433	1.377
489	0.919	488	1.110	490	0.715
--	--	506	0.543	--	--
530	0.794	531	1.882	530	0.686

The less intense violet band emission was attributed to zinc interstitial defects [185]. In general zinc interstitial defects are mobile in ZnO. Furthermore, the former report by Pokha et al. [186] and Kumar et al. [187], showed violet emission band (~416), green-blue band located at 488

nm; also, green emission located at 530 *nm* belonged to nonradiative transitions of CeO_2 nanoparticles. Therefore, the emission bands ranging 415 to 530 *nm* as observed by the charge transitions energy levels between Ce 4*f* and O 2*p* levels. They arise the transitions of Ce 4*f* band to the valence bands in CeO_2. With oxygen deficiency Ce^{+4} could switch to Ce^{+3} in CeO_2, results in the formation of oxygen vacancies in shell with electronic energy level below the 4*f* band. Hence, wide emission bands were observed in the UV and visible region [188]. Consequently, the peak at 530 *nm* in PL spectrum was associated with the surface defects and oxygen vacancy. It is interesting that PL intensity, as well as photocatalytic activity of catalysis, can be modified [189].

4.4.5. Raman spectra analysis

Those ZnO@CeO_2 CSNs were containing both ZnO with wurtzite structure and ceria with cubic fluorite structure. According to ZnO structure and its space group (C_{6v}^4), the group theory predicts the optical phonons as $A_1+E_1+2E_2+2B_1$. The A_1, E_1 and E_2 branches which are intercommunicated in Raman while the B branches are inactive, and A_1 and E_1 can split into longitudinal optical (LO) and transversal optical (TO) [190]. The modes E_1(TO) and A_1(LO) resulting from polarization in the infrared propagate parallel to z-axis [191]. The mode E_2 corresponding to the non-polarization phonon activity; has been associated with two wavenumbers E_2(high) and E_2(low) that are associated to O and Zn sublattice. Vlaic et al. and Santos et al. reported that pure CeO_2 with cubic fluorite structure (Fm3m space group) only have a single peak on Raman spectroscopy which corresponds to F_{2g} vibration mode of cubic structure [192]. This active mode is susceptible to any disorder in oxygen sublattice, grain size and doping [189].

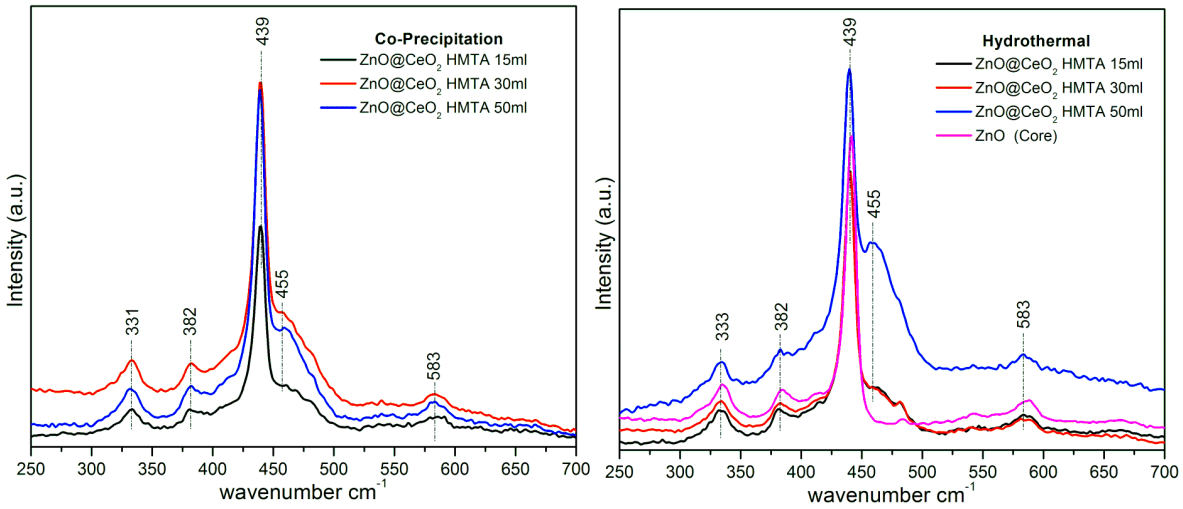

Fig. 4-43 Room temperature Raman spectra of ZnO@CeO_2 core shell particles prepared via Co-Precipitation and hydrothermal methods.

Fig. 4-43 shows a typical Raman scattering spectrum of the ZnO@CeO_2 core shell nanostructures with different thickness of shell obtained through two different methods. All the samples have five peaks and located at 331, 382, 439(sharp band), 455, 583 cm^{-1}. Perhaps the peak at 455cm^{-1} was absent in the pure ZnO. The peak appeared at 331cm^{-1} originates from the zone boundary phonons $E_2^{high} - E_2^{low}$, and the band located at 381cm^{-1} corresponds to the A_1(TO) mode. Furthermore, the peak appeared at 439 cm^{-1} corresponds to E_2^{high} mode of Raman active assigned characteristic of ZnO with wurtzite hexagonal structure [193]. Cuscó et al. [141] reported this Raman band appears at 436 cm^{-1}; therefore, a slight red shift in our results which was likely due to optical phonon confinement [171]. The broad peak at 583 cm^{-1} corresponds to the E_1(LO). The peak intensity at 439 and 583 cm^{-1} are related to characterization in a concentration of oxygen vacancy in ZnO. Besides, all of core shell samples shown a sharp Raman band appeared at 455 cm^{-1} is an original band for the fluorite cubic structures of CeO_2 [194] could be ascribed to the F_{2g}

vibration mode. Raman spectral results along with the structural and morphological studies supported the successful formation of ZnO@CeO_2.

4.4.6. Sunscreen application

Sunscreen compositions, in particular, contain additives that offer protection from ultraviolet (UV) radiation, which can damage the skin. To assess the absorption of our CSNs, known wt. % ZnO@CeO_2 CSNs was mixed with simple moisturizer with ultrasonic for 5 sec. The resultant paste was then applied on glass plate as thin layer. The absorption results displayed in Fig. 4-44. From the absorption studies, it is clearly evident that the prepared nanostructures exhibited strong absorption in the UVA and UVB regions, which signified the potential of these materials as UV blockers in the sunscreen lotions.

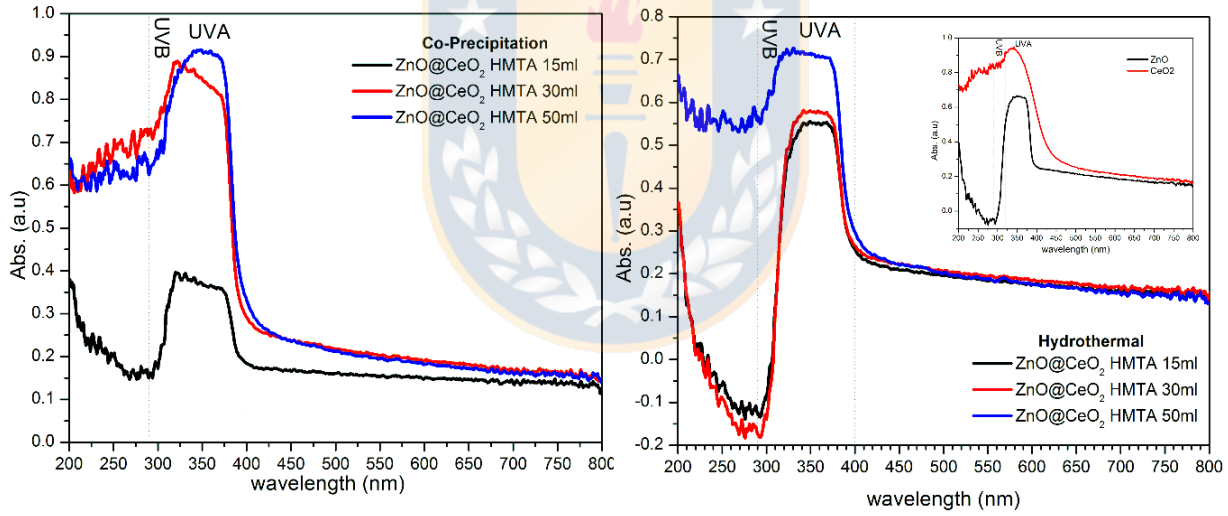

Fig. 4-44 The absorption of UV-vis spectrometer measurements of sunscreen which contains 8% of ZnO@CeO_2 core shell nanostructures.

4.5. ZnO@CeO_2 spherical core shell nanostructures

The size and morphology of prepared nanostructures were investigated by using TEM analysis and as shown in Fig. 4-45 (a-d). The TEM image exhibited (Fig. 4-45(b)) spherical ZnO

nanoparticles with average diameter 100 nm and few particles with more than 100 nm of size. The lattice fringes of 3.18 and 2.62 $\mathring{A}$ corresponding to the core and shell of ZnO@CeO_2 were depicted in Fig. 4-45(c), respectively. Moreover, as it can be seen in Fig. 4-25 (b) the shell thickness was 28 to 35nm.

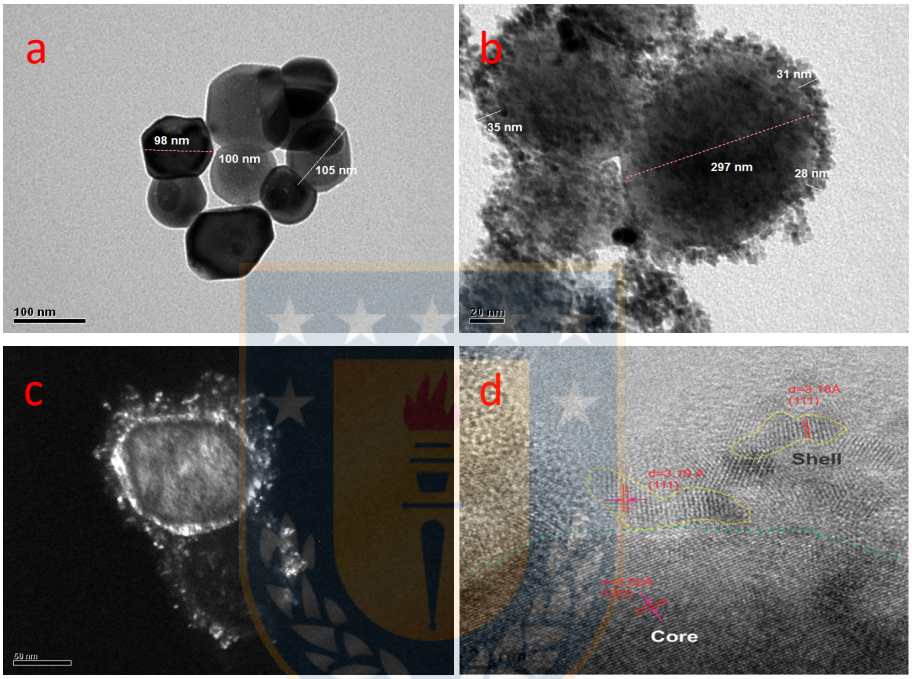

Fig. 4-45 TEM images of **(a)** spherical ZnO nanoparticles, **(b & c)** ZnO@CeO_2 spherical core shell nanostructure and HRTEM of **(d)** ZnO@CeO_2 nanostructures.

The optical absorption spectrum of the sample is shown in Fig. 4-46. As an ultraviolet blocking material, the ZnO@CeO_2 core shell nanostructures have strong absorption properties in ultraviolet range. The characteristic absorption bands at 375nm (3.31eV) and 375 nm (3.31eV) were attributed to the intrinsic band-gap absorption of ZnO and to CeO_2, respectively.

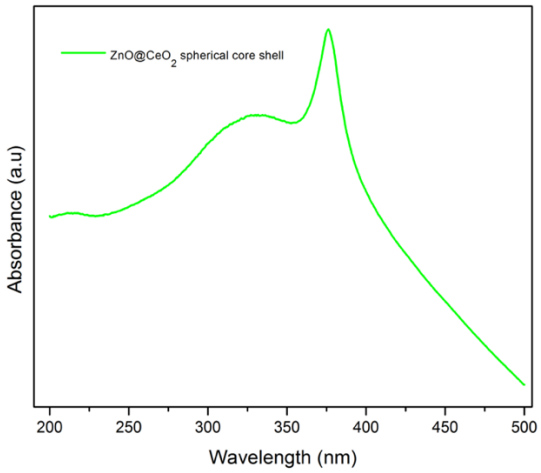

Fig. 4-46 Optical absorption spectrum of ZnO@CeO_2 spherical core shell.

The diffraction patterns of ZnO, CeO_2 and ZnO@CeO_2 spherical core shell nanostructures are shown in Fig. 4-47. The gold of refinement use for this structure is to shoe all analysis methods in order to calculate the lactic and crystallinity are similar. So, first step, in the structural analysis, trough the Rietveld-refinement procedure was applied to the raw patterns. This widely applied method is useful to refine crystal structure parameters and to determine the phase fractions in multiphase samples. The ***Rietveld*** method fits the whole pattern simultaneously by calculation of the expected intensity at a given 2θ and least squares minimization of the difference between calculated and observed intensities through variation of the atomic structures parameters. This method is very powerful and preferred to single peak and pattern decomposition methods in particular if the pattern is affected by peak overlapping. The best fits of the three samples are graphically represented in Fig. 4-47 and the refined structural details were tabulated on Table 4-17. The crystal size of ZnO and CeO_2 nanoparticles were 74.8 and 5.8nm, respectively. While in ZnO@CeO_2 spherical core shell nanostructures the crystal size of core (ZnO) was increased to 104 nm and shell was almost the same with CeO_2 particles.

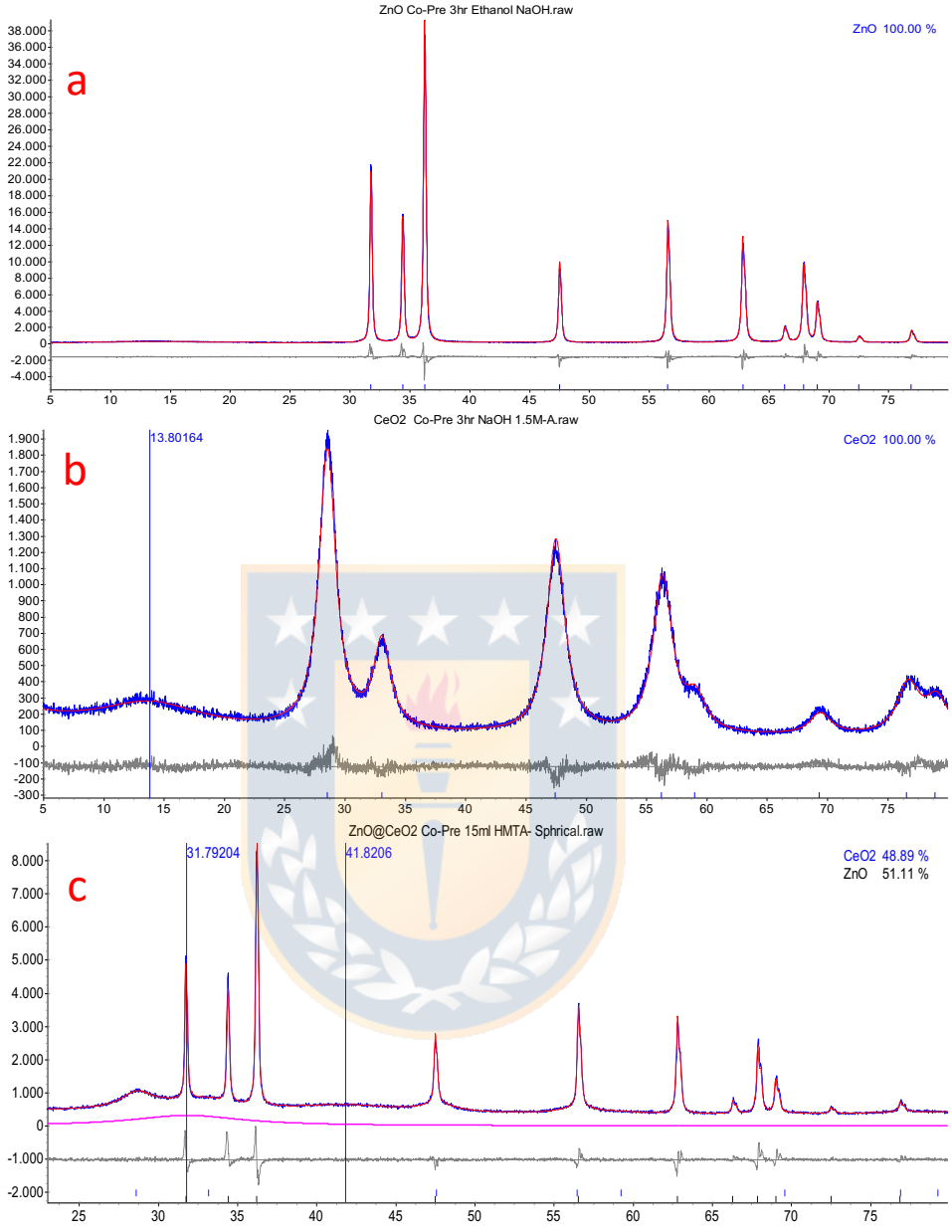

Fig. 4-47 Rietveld analysis of the (a) ZnO, (b) CeO_2 and (c)ZnO@CeO_2 spherical core shell nanostructures. The black line represents the experimental data, the red line indicates the calculated pattern and the blue line denotes the difference curve.

Table 4-17 The lattice parameters, crystallite size of ZnO, CeO_2 and their spherical core shell.

		Lattice parameter		Cell volume	Crystal size
		a (Å)	b (Å)	($Å^3$)	(nm)
ZnO		3.252	5.210	47.733	74.8
CeO_2		5.434	5.434	160.533	5.8
ZnO@CeO_2	ZnO (core)	3.253	5.211	47.770	104.1
	CeO_2 (Shell)	5.40	5.40	157.543	4.4

4.6. CeO_2@ZnO core shell nanostructures

The TEM micrographs of the prepared pure CeO_2, CeO_2@ZnO core shell nanostructures and their energy dispersive X-ray spectroscopy (EDS) are depicted in Fig. 4-48. The Fig. 4-48(a) shows core particles with~10 *nm* size. The observation of uniform shell layer consisting of the aggregation of fine ZnO covering the surface of spherical CeO_2 (core) confirmed the successful formation of CeO_2@ZnO core shell nanostructures. The thickness of ZnO shell was estimated from the TEM images. The HMTA used in the synthesis played a significant role in the realization of thin layer of ZnO on CeO_2. The elemental analysis of CeO_2@ZnO core shell nanostructures was examined through EDS analysis. The Fig. 4-49 provided with the XRD pattern of CeO_2@ZnO core shell nanostructures. The observed diffraction peaks for pristine ceria can be well indexed to the cubic fluorite structure. The XRD pattern of the sample exhibited various peaks centered at around 28.04, 32.0, 46.11, 54.75, 58.4, and 72.61° are indexed of CeO_2 crystal structure. Some other peaks were observed which can be attributed to the hexagonal phase of ZnO (shell) crystal structure. The average crystallite size of the core (CeO_2) was found to be 8 nm from the high

intensity diffraction peak of cubic cerium oxide at 28.04 which is related to plane (111) using the Debye-Scherrer equation.

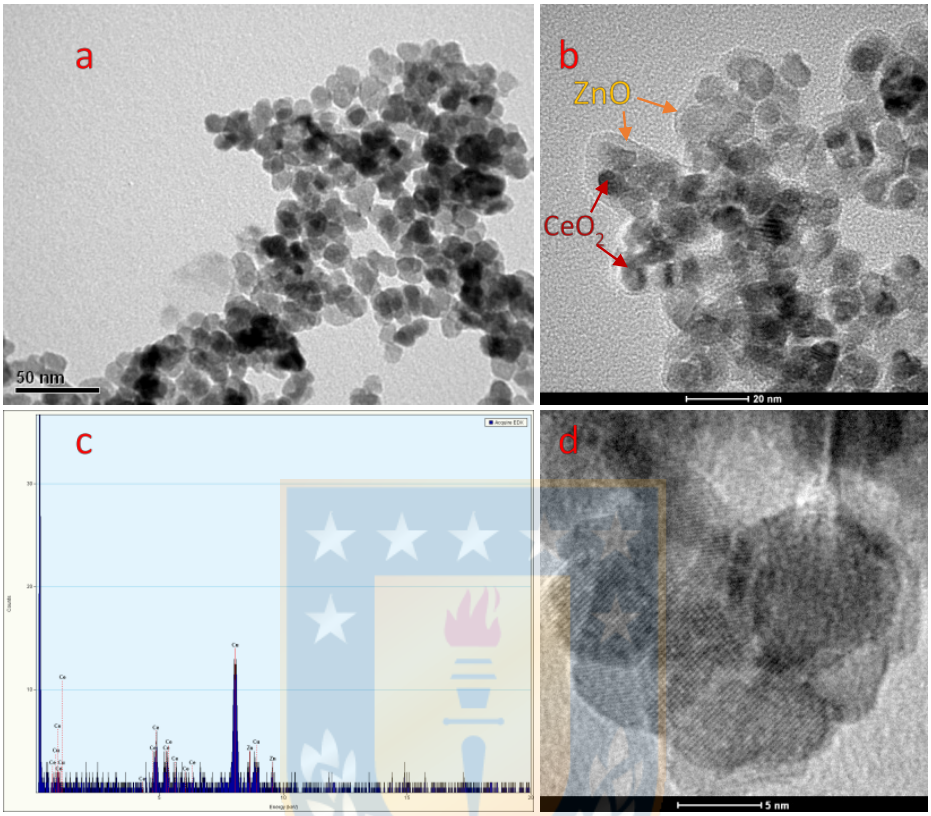

Fig. 4-48 TEM, images of **(a)** CeO_2, **(b & d)** CeO_2@ZnO core shell nanostructures and **(c)** Energy dispersive X-ray spectroscopy (EDS) of CeO_2@ZnO core shell nanostructure.

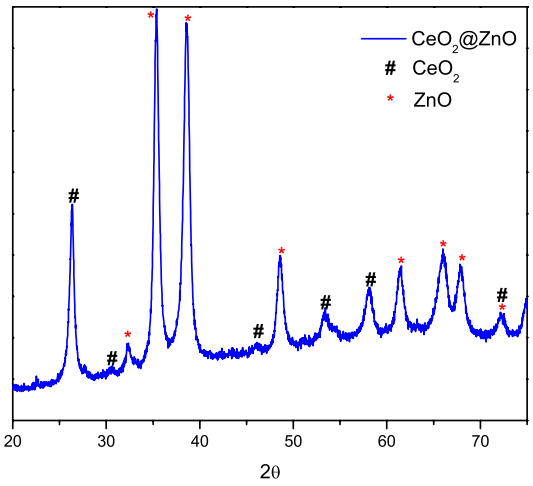

Fig. 4-49 XRD pattern of CeO_2@ZnO core shell nanostructures.

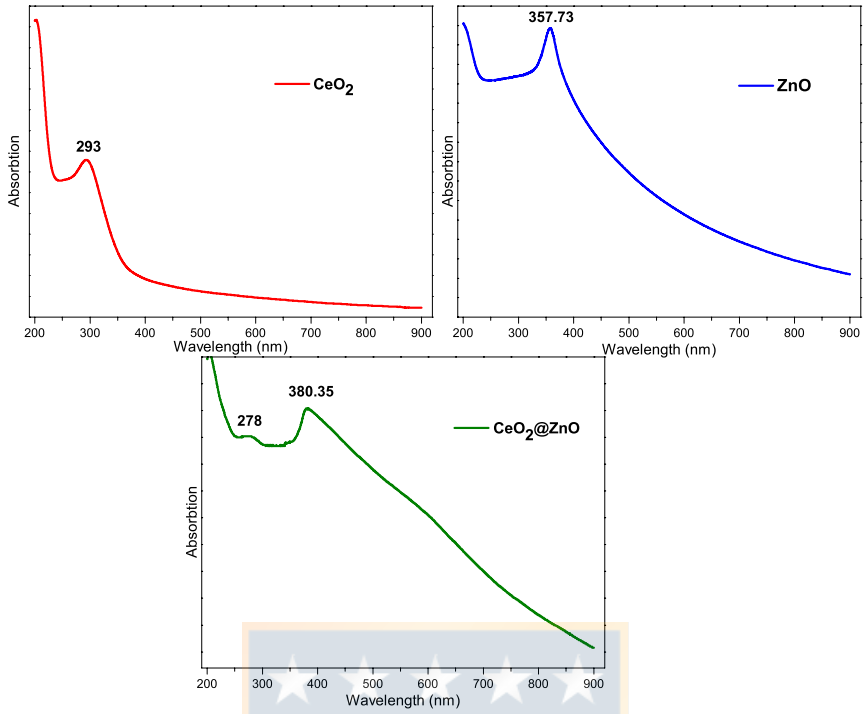

Fig. 4-50 UV-visible spectra of pure CeO_2, ZnO and CeO_2@ZnO core shell nanostructure.

The UV-visible absorption spectra of the pristine CeO_2, ZnO and CeO_2@ZnO core shell nanostructure are shown in Fig. 4-50. The core shell nanostructures consist of two peaks located at 380 and 278 nm. Furthermore, this core shell structure has strong absorption in the visible and UV regions. Due to the interfacial effect between the core and shell materials, certain change in the absorption edges were observed for CeO_2 as well ZnO nanoparticles [105]. For pure cerium oxide, the absorption edge was observed at 293 nm. However, in the case of core shell nanostructures this absorption edge was shifted to 278 nm which may be due to strong surface coupling between ZnO and CeO_2 at the interface.

Chapter 5

CONCLUSIONS

In this work, it has been adopted different synthesis routes such as hydrothermal and co-precipitation (solvothermal) based on wet chemical technique to obtain the nanoparticles of semiconductors, namely ZnO, CeO_2 and their novel core-shell nanostructures. Uniform shell layer was successfully achieved by hydrothermal and co-precipitation methods. The thickness of the shell layer was tuned by varying the HMTA concentration in the reaction process. The band gap values shown an inverse relation with the shell thickness. The lotions prepared from the nanostructures clearly exhibited strong absorption in the UV region, which paved the way for their usage in the sunscreen lotions.

In summary, in case of ZnO nanostructures, it is noted that the variation in the concentration of HMTA and variation in the reaction time led to morphological evolution of the ZnO nanostructures. It was observed that for fixed reaction time, the increase of HMTA (to an optimal level of 0.05 M of HMTA) led to the improvement of the crystallinity and favoured the formation of rod like nanostructures. It was also observed that the increase in the refluxing time of reaction led to the deterioration of the rod like morphology. It was succeeded in the preparation of hexagonal rods morphology with high crystallite size, low microstrain and high band gap values. These ideal parameters led to the observation of high NBE emission and less intense defects related emission which subsequently favoured the enhanced photocatalytic activity when compared with the other prepared samples.

In case of ceria nanostructures, the crystallization of ceria nanostructures was ultrafast, which was achieved within a few minutes (≤ 2 min) and signified the imminent success of synthesis technique for large scale. The observed variation (increase) in the band gap of the hierarchical

ceria nanostructures was attributed to the variation (increase) in the crystallite size. Apart from the bandgap related emission, all the samples exhibited emission band associated with Ce^{3+} fluorescent centers present over the surface of the nanostructures. The observed luminescence in the visible range was attributed to the various F-centers originated from oxygen vacancies. This emission was enhanced in the samples with low microstrain by favoring the formation of more defects in the nanostructures. In comparison, nearly spherical morphology exhibited high degradation efficiency of 97.72 %. The variation in the first order rate constants was attributed to the variation in the crystallite size and microstrain. The results suggested that the relaxation of microstrain (low strain) improved the charge separation and favored the enhancement in photocatalytic activity.

In the case of core shell nanostructures, at the early stages we encountered the problem in the formation of smooth shell layer on the ZnO core but we succeeded in the decoration of CeO_2 nanocubes on the surface of ZnO. The deposition of CeO_2, the size and shape of the ZnO@CeO_2 nanostructures were identified through morphological analysis. The photocatalytic studies indicated that the composite nanostructures exhibited enhanced photocatalytic activity when compared to the pure ZnO and CeO_2 nanostructures, which suggested that composite materials could offer promising applications in wastewater treatment.

As described in this dissertation, the present report discloses the production process of ZnO@CeO_2 core shell, which there can provide nanostructures with uniform aspect ratio and particle diameter. The synthesis of ZnO@CeO_2 core shell structures consists of: (i) ZnO as a core portion thereof particle formed by heating followed by refluxing, hydrothermal and high pressure wherein a mixture comprising a zinc nitrate salt and hexamethylenetetramine for rod structure; (ii) tunable aspect ratio and the particle diameter; (iii) a CeO_2 layer that forms a shell portion on the surface of ZnO core wherein core composed structure; (iv) separating the core and core shell

particles from the resulting mixtures and (v) drying and calcination of the powders of core shell nanostructures. The present report also able to provide a strategy for deposition of CeO_2 shell with varying thickness. Moreover, this research work is useful in providing simple ways of production process of ZnO@CeO_2 core shell nanostructures with tunable CeO_2 shell thickness which may be employed in UV blocker for cosmetic application and also photocatalysis application. A process for producing core shell, wherein the deposition of cerium oxide on the surface of core with different thickness, the amount of hexamethylenetetramine has been varied from 15, 30 and 50 mL with the concentration of 0.02 g/L was elaborated.

An ultraviolet shield material consists of cerium oxide coated ZnO particles of rod shape with different shell thickness was successfully evaluated. As a final sentence, this research work provides a method for preparing ZnO@CeO_2 core shell nanostructures, with tunable thickness of core and shell, for the usage as ultraviolet shielding agent and in the cosmetic applications.

References

1. J. F. Li, Y. J. Zhang, S. Y. Ding, R. Panneerselvam, and Z. Q. Tian, Chem. Rev. **117**, 5002 (2017).

2. C. Chen, C. Li, and Z. Shi, Adv. Sci. **3**, (2016).

3. T. G. Smijs and S. Pavel, Nanotechnol. Sci. Appl. **4**, 95 (2011).

4. N. M. Zholobak, V. K. Ivanov, A. B. Shcherbakov, A. S. Shaporev, O. S. Polezhaeva, A. Y. Baranchikov, N. Y. Spivak, and Y. D. Tretyakov, J. Photochem. Photobiol. B Biol. **102**, 32 (2011).

5. P. Filipe, J. N. Silva, R. Silva, J. L. Cirne de Castro, M. Marques Gomes, L. C. Alves, R. Santus, and T. Pinheiro, Skin Pharmacol. Physiol. **22**, 266 (2009).

6. T. C. Long, N. Saleh, R. D. Tilton, G. V. Lowry, and B. Veronesi, Environ. Sci. Technol. **40**, 4346 (2006).

7. S. Charles, S. Jomini, V. Fessard, E. Bigorgne-Vizade, C. Rousselle, and C. Michel, Nanotoxicology **12**, 1 (2018).

8. G. Chen, Y. Wang, Y. Wei, W. Zhao, D. Gao, H. Yang, and C. Li, ACS Appl. Mater. Interfaces **10**, 11595 (2018).

9. V. E. Kaydashev, E. M. Kaidashev, M. Peres, T. Monteiro, M. R. Correia, N. A. Sobolev, L. C. Alves, N. Franco, and E. Alves, J. Appl. Phys. **106**, 91 (2009).

10. G. Magesh, B. Viswanathan, R. P. Viswanath, and T. K. Varadarajan, Indian J. Chem. Sect. A Inorganic, Bio-Inorganic, Phys. Theor. Anal. Chem. **48**, 480 (2009).

11. D. Yin, F. Zhao, L. Zhang, X. Zhang, Y. Liu, T. Zhang, C. Wu, D. Chen, and Z. Chen, RSC Adv. **6**, 103795 (2016).

12. H. Mirzaei and M. Darroudi, Ceram. Int. **43**, 907 (2017).

13. N. Selvi, N. Padmanathan, K. Dinakaran, and S. Sankar, RSC Adv. **4**, 55745 (2014).

14. F. Carraro, A. Fapohunda, M. C. Paganini, and S. Agnoli, ACS Appl. Nano Mater. **1**, 1492 (2018).

15. K. Eguchi, T. Setoguchi, T. Inoue, and H. Arai, Solid State Ionics **52**, 165 (1992).

16. B. Nelson, M. Johnson, M. Walker, K. Riley, and C. Sims, Antioxidants **5**, 15 (2016).

17. G. Pulido-Reyes, I. Rodea-Palomares, S. Das, T. S. Sakthivel, F. Leganes, R. Rosal, S. Seal, and F. Fernández-Pinãs, Sci. Rep. **5**, 1 (2015).

18. F. Caputo, M. De Nicola, A. Sienkiewicz, A. Giovanetti, I. Bejarano, S. Licoccia, E. Traversa, and L. Ghibelli, Nanoscale **7**, 15643 (2015).

19. S. & S. Das, Dowding, Klump, McGinnis, Nanomedicine **8**, 1483 (2013).

20. M. Sack, L. Alili, E. Karaman, S. Das, A. Gupta, S. Seal, and P. Brenneisen, Mol. Cancer Ther. **13**, 1740 (2014).

21. V. V Srdić, B. Mojić, M. Nikolić, and S. Ognjanović, Process. Appl. Ceram. **7**, 45 (2013).

22. C. S. Bonifacio, S. Carenco, C. H. Wu, S. D. House, H. Bluhm, and J. C. Yang, Chem. Mater. **27**, 6960 (2015).

23. Y.-F. Zhu, N. Zhao, B. Jin, M. Zhao, and Q. Jiang, Phys. Chem. Chem. Phys. **19**, 9253 (2017).

24. R. A. Ramli, W. A. Laftah, and S. Hashim, RSC Adv. **3**, 15543 (2013).

25. M. B. Gawande, A. Goswami, T. Asefa, H. Guo, A. V Biradar, D. Peng, R. Zboril, and R. S. Varma, Chem. Soc. Rev. **44**, 7540 (2015).

26. M. M. Ismail, W. Q. Cao, and M. D. Humadi, Optik (Stuttg). **127**, 4307 (2016).

27. R. Ghosh Chaudhuri and S. Paria, Chem. Rev. **112**, 2373 (2012).

28. H. Naiki, T. Uedao, L. Wang, N. Tamai, and S. Masuo, ACS Omega **2**, 728 (2017).

29. C. Q, S. T, and J. VanEngelen, *Guidance on the Safety Assessment of Nanomaterials in Cosmetics* (European Union, 2012).

30. A. Bhattacharyya, A. Bhaumik, P. U. Rani, S. Mandal, and T. T. Epidi, African J. Biotechnol. **9**, 3489 (2010).

31. J. Jeevanandam, A. Barhoum, Y. S. Chan, A. Dufresne, and M. K. Danquah, Beilstein J. Nanotechnol. **9**, 1050 (2018).

32. C. Tian, Q. Zhang, A. Wu, M. Jiang, Z. Liang, B. Jiang, and H. Fu, Chem. Commun. **48**, 2858 (2012).

33. G. He, H. Fan, and Z. Wang, Opt. Mater. (Amst). **38**, 145 (2014).

34. A. Yumoto, F. Hiroki, I. Shiota, and N. Niwa, Surf. Coatings Technol. **169–170**, 499 (2003).

35. M. F. Al-Kuhaili, S. M. A. Durrani, and I. A. Bakhtiari, Appl. Surf. Sci. **255**, 3033 (2008).

36. T. Trindade, P. O'Brien, and N. L. Pickett, Chem. Mater. **13**, 3843 (2001).

37. X. Huang and J. Li, J. Am. Chem. Soc. **129**, 3157 (2007).

38. S. Y. Ting, H. S. Chen, W. M. Chang, J. J. Huang, C. H. Liao, C. Y. Chen, C. Hsieh, Y. F. Yao, H. T. Chen, Y. W. Kiang, and C. C. Yang, IEEE Photonics Technol. Lett. **24**, 909 (2012).

39. A. Spoiala, M. G. Albu, A. Ficai, E. Andronescu, G. Voicu, and C. Ungureanu, Dig. J. Nanomater. Biostructures **9**, 1729 (2014).

40. P. Reiss, M. Protière, and L. Li, Small **5**, 154 (2009).

41. S. Son, S. H. Hwang, C. Kim, J. Y. Yun, and J. Jang, Appl. Mater. Interfaces **5**, 4815 (2013).

42. B. Y. Guan, L. Yu, J. Li, and X. W. Lou, Sci. Adv. **2**, 2 (2016).

43. J.-Y. Le Traon, Ann. Des Télécommunications **43**, 378 (1988).

44. K. Ellmer, A. Klein, and B. Rech, editors , *Transparent Conductive Zinc Oxide* (Springer Series in Materials Science, 2008).

45. A. B. Djurišić, X. Chen, Y. H. Leung, and A. Man Ching Ng, J. Mater. Chem. **22**, 6526 (2012).

46. A. Saranya, T. Devasena, H. Sivaram, and R. Jayavel, Mater. Sci. Semicond. Process. 0 (2018).

47. R. Krahne, L. Manna, G. Morello, A. Figuerola, C. George, and S. Deka, *Physical Properties of Nanorods* (Springer, 2013).

48. A. Rahmati and M. Yousefi, Zeitschrift Fur Anorg. Und Allg. Chemie **643**, 870 (2017).

49. S. B. Jagadale, V. L. Patil, S. A. Vanalakar, P. S. Patil, and H. P. Deshmukh, Ceram. Int. **44**, 3333 (2018).

50. T. L. Lamson, S. Khan, Z. Wang, Y. K. Zhang, Y. Yu, Z. S. Chen, and H. Xu, Opt. Commun. **411**, 53 (2018).

51. R. Pietruszka, B. S. Witkowski, S. Gieraltowska, P. Caban, L. Wachnicki, E. Zielony, K. Gwozdz, P. Bieganski, E. Placzek-Popko, and M. Godlewski, Sol. Energy Mater. Sol. Cells **143**, 99 (2015).

52. J. Zhang, P. Gu, J. Xu, H. Xue, and H. Pang, Nanoscale **8**, 18578 (2016).

53. M. Poornajar, P. Marashi, D. Haghshenas Fatmehsari, and M. Kolahdouz Esfahani, Ceram. Int. **42**, 173 (2016).

54. S. Nozaki, S. N. Sarangi, S. N. Sahu, and K. Uchida, Adv. Nat. Sci. Nanosci. Nanotechnol. **4**, (2013).

55. A. Pimentel, D. Nunes, P. Duarte, J. Rodrigues, F. M. Costa, T. Monteiro, R. Martins, and E. Fortunato, J. Phys. Chem. C **118**, 14629 (2014).

56. S.-H. Jung, E. Oh, K.-H. Lee, W. Park, and S.-H. Jeong, Adv. Mater. **19**, 749 (2007).

57. W. Feng, B. Wang, P. Huang, X. Wang, J. Yu, and C. Wang, Mater. Sci. Semicond. Process.

41, 462 (2016).

58. D. Jesuvathy Sornalatha and P. Murugakoothan, Mater. Lett. **124**, 219 (2014).

59. I. Musa, N. Qamhieh, and S. T. Mahmoud, Results Phys. **7**, 3552 (2017).

60. H. Avireddy, H. Kannan, P. Shankar, G. K. Mani, A. J. Kulandaisamy, and J. B. B. Rayappan, Mater. Chem. Phys. **212**, 394 (2018).

61. V. Strano, R. G. Urso, M. Scuderi, K. O. Iwu, F. Simone, E. Ciliberto, C. Spinella, and S. Mirabella, J. Phys. Chem. C **118**, 28189 (2014).

62. M. A. Vergés, A. Mifsud, and C. J. Serna, J. Chem. Soc. Faraday Trans. **86**, 959 (1990).

63. A. Barhoum and A. S. H. Makhluuf, *Emerging Applications of Nanoparticles and Architectural Nanostructures : Current Prospects and Future Trends.* (Elsevier, 2018).

64. M. Melchionna and P. Fornasiero, Mater. Today **17**, 349 (2014).

65. J. Li, H. Li, Y. Li, W. Shen, M. Zhang, and Tana, Catal. Today **148**, 179 (2009).

66. X. H. Guo, C. C. Mao, J. Zhang, J. Huang, W. N. Wang, Y. H. Deng, Y. Y. Wang, Y. Cao, W. X. Huang, and S. H. Yu, Small **8**, 1515 (2012).

67. L. Fan, C. Wang, M. Chen, and B. Zhu, J. Power Sources **234**, 154 (2013).

68. E. Tondello, C. Maccato, C. Maragno, A. Gasparotto, G. Sberveglieri, D. Barreca, and E. Comini, Nanotechnology **18**, 125502 (2007).

69. R. W. Tarnuzzer, J. Colon, S. Patil, and S. Seal, Nano Lett. **5**, 2573 (2005).

70. L. S. Zhong, J. S. Hu, A. M. Cao, Q. Liu, W. G. Song, and L. J. Wan, Chem. Mater. **19**, 1648 (2007).

71. R. Aadhavan, S. Bhanuchandar, and K. S. Babu, Mater. Res. Express **5**, (2018).

72. X. Gao, A. Vidal, A. Bayon, R. Bader, J. Hinkley, W. Lipiński, and A. Tricoli, J. Mater. Chem. A **4**, 9614 (2016).

73. A. S. Karakoti, R. Aggarwal, J. P. Davis, R. J. Narayan, W. T. Self, J. Mcginnis, S. Seal, Y. Dqg, R. J. H. Q. Ghihfw, and U. R. J. H. Q. Vshflhv, Jom **60**, 33 (2008).

74. M. Y. Chen, X. T. Zu, X. Xiang, and H. L. Zhang, Phys. B Condens. Matter **389**, 263 (2007).

75. W. Gao, Z. Zhang, J. Li, Y. Ma, and Y. Qu, Nanoscale **7**, 11686 (2015).

76. D. Zhang, F. Niu, T. Yan, L. Shi, X. Du, and J. Fang, Appl. Surf. Sci. **257**, 10161 (2011).

77. F. Gu, Z. Wang, D. Han, C. Shi, and G. Guo, Mater. Sci. Eng. B Solid-State Mater. Adv. Technol. **139**, 62 (2007).

78. O. S. Hammond, K. J. Edler, D. T. Bowron, and L. Torrente-Murciano, Nat. Commun. **8**, 1 (2017).

79. M. Jamshidijam, P. Thangaraj, A. Akbari-Fakhrabadi, M. A. Niño Galeano, J. Usuba, and M. R. Viswanathan, Ceram. Int. **43**, 5216 (2017).

80. E. S. Bârcă, G. Stanciu, L. C. Nistor, C. Luculescu, M. Abrudeanu, C. Munteanu, V. Ion, R. Birjega, M. Dinescu, M. Filipescu, and M. Dumitru, Appl. Surf. Sci. **363**, 245 (2015).

81. L. Yin, Y. Wang, G. Pang, Y. Koltypin, and A. Gedanken, J. Colloid Interface Sci. **246**, 78 (2002).

82. P. Sathishkumar, R. V. Mangalaraja, T. Pandiyarajan, M. A. Gracia-Pinilla, N. Escalona, C. Herrera, and R. Garcia, RSC Adv. **5**, 22578 (2015).

83. F. Gao, L. Dong, L. Liu, W. Sun, Z. Yao, B. Liu, and Y. Cao, Catal. Today **175**, 48 (2011).

84. T. Sakthivel, D. C. Sayle, A. Gupta, S. Das, D. L. Reid, S. Seal, and A. Kumar, Chempluschem **78**, 1446 (2013).

85. L. Torrente-Murciano, A. Gilbank, B. Puertolas, T. Garcia, B. Solsona, and D. Chadwick, Appl. Catal. B Environ. **132**–**133**, 116 (2013).

86. M. D. Hernández-Alonso, A. Belén Hungría, A. Martínez-Arias, J. M. Coronado, J. Carlos

Conesa, J. Soria, and M. Fernández-García, Phys. Chem. Chem. Phys. **6**, 3524 (2004).

87. L. Chen, P. Fleming, V. Morris, J. D. Holmes, and M. A. Morris, J. Phys. Chem. C **114**, 12909 (2010).

88. T. X. T. Sayle, M. Cantoni, U. M. Bhatta, S. C. Parker, S. R. Hall, G. Möbus, M. Molinari, D. Reid, S. Seal, and D. C. Sayle, Chem. Mater. **24**, 1811 (2012).

89. R. Udayabhaskar and B. Karthikeyan, J. Appl. Phys. **116**, (2014).

90. S. K. Pardeshi and A. B. Patil, J. Mol. Catal. A Chem. **308**, 32 (2009).

91. H. Feng, Z. Xu, L. Wang, Y. Yu, D. Mitchell, D. Cui, X. Xu, J. Shi, T. Sannomiya, Y. Du, W. Hao, and S. X. Dou, ACS Appl. Mater. Interfaces **7**, 27592 (2015).

92. A. Cantarero, G. Ionita, Z. D. Dohčević-Mitrović, V. D. Araújo, S. Aškrabić, and M. M. de Lima, J. Phys. D. Appl. Phys. **46**, 495306 (2013).

93. T. Gao, Q. Li, and T. Wang, Chem. Mater. **17**, 887 (2005).

94. G. Raju Kumar and M. Mrinmoy, *Metal Semiconductor Core-Shell Nanostructures for Energy and Environmental Applications* (Elsevier, Amsterdam, 2017).

95. A. I. Y. Tok, F. Y. C. Boey, Z. Dong, and X. L. Sun, J. Mater. Process. Technol. **190**, 217 (2007).

96. N. Li, Y. Li, W. Li, S. Ji, and P. Jin, J. Phys. Chem. C **120**, 3341 (2016).

97. N. T. K. Thanh, N. Maclean, and S. Mahiddine, **3**, (2014).

98. S. S., Mod. Asp. Bulk Cryst. Thin Film Prep. (2012).

99. M. Iwamatsu, Phys. Rev. E **95**, 1 (2017).

100. H. Reiss, J. Chem. Phys. **19**, 482 (1951).

101. Y. Lu, Y. Yin, Z. Li, and Y. Xia, 2 (2002).

102. Peter Reiss, Joël Bleuse, and and Adam Pron, Nano Lett. **2**, 781 (2002).

103. D. Pan, Q. Wang, J. Pang, S. Jiang, X. Ji, and L. An, Chem. Mater. **18**, 4253 (2006).

104. C. Li, X. Zhang, W. Dong, and Y. Liu, Mater. Lett. **80**, 145 (2012).

105. N. Selvi, N. Padmanathan, K. Dinakaran, and S. Sankar, RSC Adv. **4**, 55745 (2014).

106. X. S. Wang, Z. C. Wu, J. F. Webb, and Z. G. Liu, Appl. Phys. A Mater. Sci. Process. **77**, 561 (2003).

107. M. S. Ghamsari, S. Alamdari, D. Razzaghi, and M. Arshadi Pirlar, J. Lumin. **205**, 508 (2019).

108. Ü. Özgür, Y. I. Alivov, C. Liu, A. Teke, M. A. Reshchikov, S. Doğan, V. Avrutin, S. J. Cho, and H. Morkç, J. Appl. Phys. **98**, 1 (2005).

109. A. Manohar and C. Krishnamoorthi, Mater. Chem. Phys. **192**, 235 (2017).

110. C. Belkhaoui, N. Mzabi, and H. Smaoui, Mater. Res. Bull. **111**, 70 (2019).

111. A. Manohar and C. Krishnamoorthi, J. Mater. Sci. Mater. Electron. **29**, 737 (2018).

112. A. Manohar and C. Krishnamoorthi, J. Cryst. Growth **473**, 66 (2017).

113. A. Manohar and C. Krishnamoorthi, J. Magn. Magn. Mater. **443**, 267 (2017).

114. M. Yilmaz, B. Bozkurt Cirak, C. Cirak, and S. Aydogan, Philos. Mag. Lett. **96**, 45 (2016).

115. R. Parize, J. Garnier, O. Chaix-Pluchery, C. Verrier, E. Appert, and V. Consonni, J. Phys. Chem. C **120**, 5242 (2016).

116. T. Pandiyarajan, R. V. Mangalaraja, B. Karthikeyan, S. Sepulveda-Guzman, H. D. Mansilla, D. Contreras, N. Escalona, and M. A. Gracia-Pinilla, RSC Adv. **6**, 20437 (2016).

117. A. Manohar and C. Krishnamoorthi, J. Alloys Compd. **722**, 818 (2017).

118. H. Zhang, G. Liu, Y. Cao, J. Chen, K. Shen, A. Kumar, M. Xu, Q. Li, and Q. Xu, Phys. Chem. Chem. Phys. **19**, 26918 (2017).

119. J. Fang, H. Fan, Y. Ma, Z. Wang, and Q. Chang, Appl. Surf. Sci. **332**, 47 (2015).

120. M. Yin, C.-K. Wu, Y. Lou, C. Burda, J. T. Koberstein, Y. Zhu, and S. O'Brien, J. Am. Chem. Soc. **127**, 9506 (2005).

121. O. K. Echendu, S. Z. Werta, F. B. Dejene, and V. Craciun, J. Alloys Compd. **769**, 201 (2018).

122. S. M. H. AL-Jawad, S. H. Sabeeh, A. A. Taha, and H. A. Jassim, J. Sol-Gel Sci. Technol. (2018).

123. J. Singh, P. Kumar, K. S. Hui, K. N. Hui, K. Ramam, R. S. Tiwari, and O. N. Srivastava, CrystEngComm **14**, 5898 (2012).

124. O. Oprea, E. Andronescu, B. S. Vasile, G. Voicu, and C. Covaliu, Dig. J. Nanomater. Biostructures **6**, 1393 (2011).

125. D. Chen, Z. Wang, T. Ren, H. Ding, W. Yao, R. Zong, and Y. Zhu, J. Phys. Chem. C **118**, 15300 (2014).

126. T. Pandiyarajan, M. L. Baesso, and B. Karthikeyan, Eur. Phys. J. D **68**, (2014).

127. Q. Li, S. Fu, C. Song, G. Wang, F. Zeng, and F. Pan, J. Mater. Sci. Mater. Electron. **28**, 17881 (2017).

128. F. Kayaci, S. Vempati, I. Donmez, N. Biyikli, and T. Uyar, Nanoscale **6**, 10224 (2014).

129. D. Das and P. Mondal, RSC Adv. **4**, 35735 (2014).

130. H. Chen, J. Ding, W. Guo, G. Chen, and S. Ma, RSC Adv. **3**, 12327 (2013).

131. Y. Yang, B. K. Tay, X. W. Sun, J. Y. Sze, Z. J. Han, J. X. Wang, X. H. Zhang, Y. B. Li, and S. Zhang, Appl. Phys. Lett. **91**, 1 (2007).

132. L. Wischmeier, T. Voss, I. Rückmann, J. Gutowski, A. C. Mofor, A. Bakin, and A. Waag, Phys. Rev. B - Condens. Matter Mater. Phys. **74**, 1 (2006).

133. M. J. Chithra, M. Sathya, and K. Pushpanathan, Acta Metall. Sin. (English Lett. **28**, 394

(2015).

134. R. Kumar, N. Khare, V. Kumar, and G. L. Bhalla, Appl. Surf. Sci. **254**, 6509 (2008).

135. T. Pandiyarajan, R. Udayabhaskar, and B. Karthikeyan, Appl. Phys. A Mater. Sci. Process. **107**, 411 (2012).

136. R. Udayabhaskar and B. Karthikeyan, J. Appl. Phys. **115**, 1 (2014).

137. R. Aepuru and H. S. Panda, J. Phys. Chem. C **120**, 4813 (2016).

138. T. C. Damen, S. P. S. Porto, and B. Tell, J. Phys. Chem. Solids Mitra J. I. Bryant, Bull. Am. Phys. Soc **142**, 1085 (1966).

139. R. Udayabhaskar, R. V. Mangalaraja, and B. Karthikeyan, Plasmonics **10**, 893 (2015).

140. M. Šćpanović, M. Grujić-Brojčin, K. Vojisavljevič, S. Bernik, and T. Srećković, J. Raman Spectrosc. **41**, 914 (2010).

141. R. Cuscó, E. Alarcón-Lladó, J. Ibáñez, L. Artús, J. Jiménez, B. Wang, and M. J. Callahan, Phys. Rev. B **75**, 165202 (2007).

142. R. Udayabhaskar and B. Karthikeyan, J. Am. Ceram. Soc. **98**, (2015).

143. B. Cheng, W. Sun, J. Jiao, B. Tian, Y. Xiao, and S. Lei, J. Raman Spectrosc. **41**, 1221 (2010).

144. M. Yoshikawa, K. Inoue, T. Nakagawa, H. Ishida, N. Hasuike, and H. Harima, Appl. Phys. Lett. **92**, 1 (2008).

145. Z. Song, T. A. Kelf, W. H. Sanchez, M. S. Roberts, J. Rička, M. Frenz, and A. V. Zvyagin, Biomed. Opt. Express **2**, 3321 (2011).

146. C. Balkas, H. Shin, R. Davis, and R. Nemanich, Phys. Rev. B - Condens. Matter Mater. Phys. **59**, 12977 (1999).

147. A. Li Bassi, D. Cattaneo, V. Russo, C. E. Bottani, E. Barborini, T. Mazza, P. Piseri, P.

Milani, F. O. Ernst, K. Wegner, and S. E. Pratsinis, J. Appl. Phys. **98**, (2005).

148. A. Manohar and C. Krishnamoorthi, J. Photochem. Photobiol. B Biol. **177**, 95 (2017).

149. A. Manohar and C. Krishnamoorthi, J. Photochem. Photobiol. B Biol. **173**, 456 (2017).

150. L. Yan, R. Yu, J. Chen, and X. Xing, Cryst. Growth Des. **8**, 1474 (2008).

151. Z. Wang, Z. Quan, and J. Lin, Inorg. Chem. **46**, 5237 (2007).

152. C. Ho, J. C. Yu, T. Kwong, A. C. Mak, and S. Lai, Chem. Mater. **17**, 4514 (2005).

153. S. Tsunekawa, J.-T. Wang, Y. Kawazoe, and A. Kasuya, J. Appl. Phys. **94**, 3654 (2003).

154. Y. W. Zhang, R. Si, C. S. Liao, C. H. Yan, C. X. Xiao, and Y. Kou, J. Phys. Chem. B **107**, 10159 (2003).

155. T. Taniguchi, Y. Sonoda, M. Echikawa, Y. Watanabe, K. Hatakeyama, S. Ida, M. Koinuma, and Y. Matsumoto, ACS Appl. Mater. Interfaces **4**, 1010 (2012).

156. E. Álvarez, M. E. Zayas, D. Rodríguez-Carvajal, F. Félix-Domínguez, R. P. Duarte-Zamorano, C. Falcony, and U. Caldiño, Opt. Mater. (Amst). **37**, 451 (2014).

157. K. M. Parida and S. Parija, Sol. Energy **80**, 1048 (2006).

158. J. Yu and X. Yu, Environ. Sci. Technol. **42**, 4902 (2008).

159. H. Sudrajat and P. Sujaridworakun, J. Mol. Liq. **242**, 433 (2017).

160. S. W. Lee, S. Obregón, and V. Rodríguez-González, RSC Adv. **5**, 44470 (2015).

161. N. Sutradhar, A. Sinhamahapatra, S. Pahari, M. Jayachandran, B. Subramanian, H. C. Bajaj, and A. B. Panda, J. Phys. Chem. C **115**, 7628 (2011).

162. C. Anandan and P. Bera, Appl. Surf. Sci. **283**, 297 (2013).

163. A. Younis, D. Chu, Y. V. Kaneti, and S. Li, Nanoscale **8**, 378 (2016).

164. M. Yu, Y. Tong, S. Xie, X. Lu, C. Zeng, and Y. Yang, J. Power Sources **247**, 545 (2013).

165. R. Sankar ganesh, M. Navaneethan, G. K. Mani, S. Ponnusamy, K. Tsuchiya, C.

Muthamizhchelvan, S. Kawasaki, and Y. Hayakawa, J. Alloys Compd. **698**, 555 (2017).

166. J. Calvache-Muñoz, F. A. Prado, and J. E. Rodríguez-Páez, Colloids Surfaces A Physicochem. Eng. Asp. **529**, 146 (2017).

167. T. E. P. Alves, C. Kolodziej, C. Burda, and A. Franco, Mater. Des. **146**, 125 (2018).

168. E. K. Goharshadi, S. Samiee, and P. Nancarrow, J. Colloid Interface Sci. **356**, 473 (2011).

169. C. Sun, H. Li, H. Zhang, Z. Wang, and L. Chen, Nanotechnology **16**, 1454 (2005).

170. N. Ahmad, A. Umar, R. Kumar, and M. Alam, Ceram. Int. **42**, 11562 (2016).

171. R. Lamba, A. Umar, S. K. Mehta, and S. K. Kansal, J. Alloys Compd. **620**, 67 (2015).

172. N. Assi, P. A. Azar, M. S. Tehrani, and S. W. Husain, J. Iran. Chem. Soc. **13**, 1593 (2016).

173. H. Zhou, Y. Qu, T. Zeid, and X. Duan, Energy Environ. Sci. **5**, 6732 (2012).

174. B. G. Mishra and G. R. Rao, J. Mol. Catal. A Chem. **243**, 204 (2006).

175. I. S. Ahuja, C. L. Yadava, and R. Singh, J. Mol. Struct. **81**, 229 (1982).

176. N. Bhargava, V. Shanmugaiah, M. Saxena, M. Sharma, N. K. Sethy, S. K. Singh, K. Balakrishnan, K. Bhargava, and M. Das, Biointerphases **11**, 031016 (2016).

177. W. Tian, M. A. Pouchon, H. Guo, D. Chen, X. Yin, and Z. Qin, Ceram. Int. **44**, 6739 (2018).

178. O. S. Polezhaeva, N. V. Yaroshinskaya, and V. K. Ivanov, Russ. J. Inorg. Chem. **52**, 1184 (2007).

179. R. Udayabhaskar, R. V. Mangalaraja, S. F. Sahlevani, V. T. Perarasu, B. Karthikeyan, D. Contreras, and M. A. Gracia-Pinilla, J. Alloys Compd. **770**, (2019).

180. F. K. Shan and Y. S. Yu, J. Eur. Ceram. Soc. **24**, 1869 (2004).

181. S. S. Kumar, P. Venkateswarlu, V. R. Rao, and G. N. Rao, Int. Nano Lett. **3**, 30 (2013).

182. E. D. Sherly, J. J. Vijaya, and L. J. Kennedy, J. Mol. Struct. **1099**, 114 (2015).

183. J. Liqiang, Q. Yichun, W. Baiqi, L. Shudan, J. Baojiang, Y. Libin, F. Wei, F. Honggang, and S. Jiazhong, Sol. Energy Mater. Sol. Cells **90**, 1773 (2006).

184. A. Simimol, P. Chowdhury, S. K. Ghosh, and H. C. Barshilia, Electrochim. Acta **90**, 514 (2013).

185. S. Chattopadhyay, S. Dutta, P. Pandit, D. Jana, S. Chattopadhyay, A. Sarkar, P. Kumar, D. Kanjilal, D. K. Mishra, and S. K. Ray, Phys. Status Solidi Curr. Top. Solid State Phys. **8**, 512 (2011).

186. S. Phokha, S. Pinitsoontorn, P. Chirawatkul, Y. Poo-arporn, and S. Maensiri, Nanoscale Res. Lett. **7**, 1 (2012).

187. S. Kumar, A. K. Ojha, D. Patrice, B. S. Yadav, and A. Materny, Phys. Chem. Chem. Phys. **18**, 11157 (2016).

188. S. K. Sahoo, M. Mohapatra, A. K. Singh, and A. Shashi, Mater. Manuf. Process. **25**, 982 (2010).

189. B. Sabu and T. Varghese, **53**, 596 (2015).

190. C. A. Arguello, D. L. Rousseau, and S. P. S. Porto, Phys. Rev. **181**, 1351 (1969).

191. A. F. Jaramillo, R. Baez-Cruz, L. F. Montoya, C. Medinam, E. Pérez-Tijerina, F. Salazar, D. Rojas, and M. F. Melendrez, Ceram. Int. **43**, 11838 (2017).

192. M. L. Dos Santos, R. C. Lima, C. S. Riccardi, R. L. Tranquilin, P. R. Bueno, J. A. Varela, and E. Longo, Mater. Lett. **62**, 4509 (2008).

193. M. E. Koleva, N. N. Nedyalkov, P. A. Atanasov, N. Fukata, and M. Dutta, **9447**, 94470E (2015).

194. S. Y. Wang, N. Li, L. F. Luo, W. X. Huang, Z. Y. Pu, Y. J. Wang, G. S. Hu, M. F. Luo, and J. Q. Lu, Appl. Catal. B Environ. **144**, 325 (2014).

Publication

Journal articles

1. **Saeed Farhang-Sahlevani**, Thangaraj Pandiyarajan, Felipe Sanhueza, Ali Akbari-Fakhrabadi, Héctor D. Mansilla, David Contreras, Ramalinga Viswanathan Mangalaraja, M. A. Gracia-Pinilla "*A facile hydrothermal synthesis of CeO_2 nanocubes decorated ZnO nanostructures: optical and enhanced photocatalytic properties*" Journal of Materials Science: Materials in Electronics 2019 in press. DOI: 10.1007/s10854-019-01521-8.
2. R. Udayabhaskar, R.V. Mangalaraja, **Saeed Farhang Sahlevani**, V.T. Perarasu, B. Karthikeyan, David Contreras, M.A. Gracia-Pinilla "*Graphene induced band gap widening and luminescence quenching in ceria:graphene nanocomposites*" Journal of alloys and compounds 2019 Vol. 770 1221-1228. DIO: 10.1016/j.jallcom.2018.08.226.
3. R. Udayabhaskar, **Saeed Farhang Sahlevani**, T Prabhakaran, T Pandiyarajan, B Karthikeyan, David Contreras, RV Mangalaraja *"Modulation of optical and photocatalytic properties by morphology and microstrain in hierarchical ceria nanostructures"* Solar Energy Materials and Solar Cells 2019 Vol. 195 106-113. DOI: 10.1016/j.solmat.2019.02.033.

Patent

1. Pandiyarajan Thangaraj, **Saeed Farhang Sahlevani**, Felipe Sanhueza, Marta López, Carlos Von Plessing, Mangalaraja Ramalinga Viswanathan *"Proceso de síntesis para la obtención de materiales núcleo-coraza ZnO-CeO_2 de espesor regulable, para aplicación de protección ultravioleta"* Instituto Nacional de Propiedad Industrial (INAPI) Chile 2017 N° Solicitud 2995-17.

Conference presentation

1. **Saeed Farhang Sahlevani**, Felipe Sanhueza, Pandiyarajan Thangaraj, Mangalaraja Ramalinga Viswanathan, *"Optical and Photocatalysis Activity of CeO2@ ZnO Core@Shell Nanostructures Synthesized by Solvothermal route"*
   Conference name: **TMS 2017**
   Place: San Diego, California – USA
   Date: 26th Feb. - 2nd Mar. 2017

2. ***Saeed Farhang Sahlevani**, Ramalinga Viswanathan Mangalaraja, Pandiyarajan Thangaraj, Felipe Sanhueza, "Optical and Photocatalytic Activity of CeO_2@ZnO Core-Shell Nanostructures Synthesized by Hydrothermal route"*
   Conference name: **XXVI International Materials Research Congress**
   Place: Cancún – México.
   Date: 20th– 25thAug. 2017.

3. *Saeed Farhang Sahlevani, Ramalinga Viswanathan Mangalaraja, Pandiyarajan Thangaraj, Felipe Sanhueza*, "Facile synthesis of ZnO@CeO_2 core-shell nanorods by hydrothermal route"
   Conference name: **XVII CONGRESO CONAMET/SAM 2017**
   Place: Copiapó – Chile
   Date: 18th -20th Oct. 2017

4. *Saeed Farhang Sahlevani, Ramalinga Viswanathan Mangalaraja, Pandiyarajan Thangaraj, Felipe Sanhueza, "*Facile synthesis of CeO_2@ZnO core-shell nanostructures by solvothermal route"
   Conference name: **Functional Integrated nanosystems- nanoFIS 2017**
   Place: Graz – Austria.
   Date: 22nd to 24th November 2017.